CARNEGIE MELLON UNIVERSITY

Computational Study of Structure and Dynamics of Ionic Liquids

by
Jiannan Liu

A thesis submitted in partial fulfillment for the
degree of Doctor of Philosophy

in the
Hyung J. Kim
Department of Chemistry, Mellon College of Science

May 2019

The chapters below are reprinted or adapted from published articles with permission.

Chapter 2: Reprinted with permission from J. Phys. Chem. B, **2018**, *122* (42), 9747–9756. Copyright 2018 American Chemical Society.

Chapter 4: Reprinted from J. Chem. Phys., **2018**, *148*, 193830, with the permission of AIP Publishing.

Abstract

Sulfonic acid based and imidazolium-based ionic liquids were studied in this thesis. A classical force field for sulfonic acid was developed in OPLS-AA and CHARMM format. The structure and dynamics of alyl sulfonic acid was examined to validated the force field, including density, heat of vaporization and transport properties. The radial distribution function produced from the force field was also compared with the results of ab inito molecular dynamics. Next, the dissolution of ZnO $(10\bar{1}0)$ surface in a sulfonic acid based ionic liquid was studied using ab initio approaches. Possible pathways of the initial dissolution process are explored. Energies of proton transfer from ionic liquids to ZnO $(10\bar{1}0)$ surfaces are calucated. The solvation of zinc ion is also discussed. For imidazolium-based ionic liquids, its heterogeneous dynamics was invastigated with the help of four point correlation function. In addition, we also proposed a new "mobile" self four point correlation function to better describe the collective motions. A comparison between imidazolium-based ionic liquids, choline acetate and acetonitrile was presented. The effects of the side chain length of imidazolium-based ionic liquids were also discussed in detail. In the end, the interactions between the anions and the hydrogens on the imidazolium ring were examined with the calculation of their vibrational spectroscopy. The results of classical force field and DFT calculations were compared.

Acknowledgments

I would like to thank my advisor, Prof. Hyung Kim, for his support for my Ph.D research. His guidance is great fortune for my career and my life.

I appreciate Profs. David Yaron, Kevin Noonan and Sean Garrett-Roe to serve on my committee.

I would also like to thank Nilesh Dhumal, Hyunjin Kim, Fangyong Yan, Andrew DeYoung, Hadi Abroshan, Jon Willcox and Yao Li. Their advice and discussions were always benefical.

Contents

List of Tables

List of Figures

Introduction

1.1 Ionic liquid

An ionic liquid (IL) refers to a molten salt whose melting point (m.p.) is typically below 100 ℃.[1,2] Common ILs consist of imidazolium-, pyridinium-, pyrrolidinium- or ammonium-based cation paired with anions such as halides, tetrafluoroborate (BF_4), hexafluorophosphate (PF_6), bis(trifluoromethylsulfonyl)imide (Tf_2N) or bis-(fluorosulfonyl)imide (FSI). Low temperature IL (m.p. below 130K) has been proposed to build lunar liquid mirror telescope.[3]

Common characteristics of ionic liquids, e.g. high viscosity, thermal stability and low vapor pressure, are governed by the strong electrostatic interactions between ions. Specific conductivities of ionic liquids limited by their viscosities usually fall in the region of aqueous solutions. Solubility in ionic liquids depends mainly on polarity and hydrogen bonding ability. The miscibility with water and organic solvents can be tuned by varying the anionic species and/or the length of side chains of the cations.

Applications of ILs have been actively developing over the past decade.[2] ILs are considered "green" solvents for synthesis and extraction because of their recyclability and stability. ILs are also used as an electrolyte in rechargeable lithium ion batteries and as a dielectric medium in capacitors. ILs are employed in solar thermal systems as a heat transfer and storage medium. IL-based methods are developed for gas storage and handling.

Imidazolium-based ILs are among the most investigated ILs.[4] Their positive charge is highly delocalized across the imidazolium ring. The hydrogen of C-2 carbon of the imidazolium ring is acidic and can have hydrogen bonding capability. Their solubility and miscibility can be tuned by changing the alkyl groups. Imidazolium-based ILs can form a partially ordered ion network through cation-anion interaction, which can be used to synthesize nanoparticles.[5,6]

Cyclic alkyl quaternary ammonium cations, such as pyrrolidinium- and piperidinium-

based ILs have gained considerable interests during the last several years owing to their wide electrochemical windows and water immiscibility.[7] They can be applied as electrolytes in electrochemical reduction and polymer electrolyte composition in lithium ion batteries and chemical capacitors. Due to the localized charge on nitrogen, cyclic alkyl quaternary ammonium cations have stronger electrostatic interactions than imidazolium-based cations, resulting in higher melting points. To decrease their melting points, cyclic alkyl quaternary ammonium cations are often paired with Tf_2N.

Anions also play an important role in ILs. Their size and symmetry can significantly influence the melting points, viscosities and conductivities of ILs. ILs containing Tf_2Noften have low melting points and low viscosities due to its delocalized charge and low symmetry. Halides and symmetric anions such as $BF_4$and PF_6lead to higher melting points. Hydrogen bonding ability of anions is also important especially when paired with imidazolium-based cations.

Functionalized ILs which are designed for a specific purpose, e.g. as the solvent or catalyst for specific reaction, separation and extraction, are called task specific ionic liquids (TSILs). The alkyl chain of imidazolium-based IL can be customized as the reaction medium for catalytic reation.[8] TSIL with an acidic counteranion has been applied in esterification reactions as a dual solvent–catalyst system.[9] Many TSILs can be used in mineral processing to selectively dissolve metal oxides.[10–12] TSILs are also being developed to capture CO_2.[13]

Dissolution of metal oxides using ionic liquids was first reported by Dai et al.[14] and Bell et al.[15] Imidazolium chloroaluminate melt was found to be able to dissolve UO_3 and V_2O_5. Betaine bis(trifluoromethylsulfonyl)imide was used for the dissolution of rare earth oxides.[11,16] Other IL cations, such as imidazolium- and cyclic alkyl quaternary ammonium-based cations, can be functionalized with a carboxyl group to achieve selective dissolution.[17] Eutectic mixture of choline chloride and hydrogen bond

donors, such as carboxylic acids, amines, alcohols and urea is also a novel solvent for mineral leaching.[18,19] Dissolution of gold, silver, copper and base metal from sulphidic ores using 1-butyl-3-methylimidazolium hydrogen sulphate is also reported.[20,21]

1.2 Computer modeling

Computer simulation of liquid systems is common nowadays. It can be applied to study the structure and properties of water, proteins and organic liquids. Computer simulation can be categorized into classical and ab initio method based on their underlying computational models determining the interaction between atoms.

Classical methods, such classical molecular dynamics (MD) and classical Monte Carlo (MC) simulation, are widely used because they are fast and can provide reasonable accuracy. These methods employ an empirical force field to calculate the force and energy of the simulation system. An empirical force field usually contains bonded and nonbonded terms. Typically, bonded terms include bond stretching, angle bending and torsional rotation. Improper angles may be used to enforce geometric constraints. Cross terms can also be added to ensure proper conformation. Nonbonded interactions are electrostatic interactions and van der Waals interactions. Various force fields have been developed for different purposes, including MM3[22], CHARMM[23,24], AMBER[25–28] and OPLS[29].

Since electrostatic interactions play an important role in determining the properties of ILs, partial charge assignment is crucial for IL systems. Different force fields employ different methedologies to model the electrostatic interaction. Gasteiger-Marsili model[30,31] considers partial equalization of electronegativity between bonded atoms. In the early version of AMBER,[25,26] Mulliken charges were used to represent the electrostatic interaction between atoms, but this model does not reproduce electrostatic potential of a molecule very well. Later, AMBER94[27,28] switched to RESP

charges, for Restrained ElectroStatic Potential fit. CHARMM[23,24] uses charges from electrostatic potential fit (ESP) of the molecule pairing with hydrogen bond donors and acceptors, such as water, as the initial guess, and this initial guess is further modified to reproduce the distances and interaction energies. The original OPLS force field[29,32,33] fits charges to reproduce liquid properties. In the OPLS force field, molecules are divided into neutral subunits, which makes charges transferable, especially for macromolecules. Other OPLS-based force field[34–36] also uses ESP charges, such as charges based on CHELPG method (CHarges from Electrostatic Potentials using a Grid based method)[37], but ESP charges cannot be applied to large molecules, such as spherands[38], because of conformational variability and accuracy of charges for innermost atoms. For large systems, RESP charges are good alternatives.

Another term in nonbonded interactions, van der Waals interaction, is usually adjusted to reproduce thermodynamic properties, such as density, heat of vaporization and solvation enthapy.[29] Alkanes are often chosen as the starting point because their electrostatic interactions are negligible. Van der Waals parameters are often transferable between different molecules when their coordination numbers are the same.

Most of bonded parameters are fitted to ab initio calculations. Bond and angle force constants were usually taken from Hessian matrix.[23] But it was found that these parameters did not reproduce experimental vibrational spectra of molecules.[39] Later, bond and angle force constants are fitted to potential energy surface (PES) obtained from ab initio method, or these force constants are modified to reproduce experimental vibrational spectra. Fitting dihedral parameters to PES scan is considered the most accurate and reliable method.

Ab initio methods evaluate the forces and energies of the system based on quantum chemistry. Several approximations have to be adopted, such as Born Oppenheimer (BO) method and Car-Parrinello (CP) method.[40] To accelerate the simulation, in-

teractions between atoms are often modeled by pseudopotentials instead of the exact atomic potentials. Forces and energies are evaluated through density functional theory (DFT). Ab initio methods have their native advantages in simulating chemical reactions and electronic properties. Since ab initio methods are much more time consuming than classical methods, it is sometimes beneficial to combine quantum mechanics and molecular mechanics (QM/MM) methods in order to simulate large systems accurately and efficiently.

[1] Marsh, K.; Boxall, J.; Lichtenthaler, R. Room temperature ionic liquids and their mixtures—a review. *Fluid Phase Equilibria* **2004**, *219*, 93 – 98.

[2] Plechkova, N. V.; Seddon, K. R. Applications of ionic liquids in the chemical industry. *Chem. Soc. Rev.* **2008**, *37*, 123–150.

[3] Borra, E. F.; Seddiki, O.; Angel, R.; Eisenstein, D.; Hickson, P.; Seddon4, K. R.; Worden, S. P. Deposition of metal films on an ionic liquid as a basis for a lunar telescope. *Nature* **2007**, *447*, 979 – 981.

[4] Shukla, M.; Saha, S. In *Ionic Liquids - New Aspects for the Future*; Kadokawa, J., Ed.; 2013; Chapter 3.

[5] Chiappe, C.; Sanzone, A.; Mendola, D.; Castiglione, F.; Famulari, A.; Raos, G.; Mele, A. Pyrazolium- versus Imidazolium-Based Ionic Liquids: Structure, Dynamics and Physicochemical Properties. *The Journal of Physical Chemistry B* **2013**, *117*, 668–676.

[6] Gutel, T.; Santini, C. C.; Philippot, K.; Padua, A.; Pelzer, K.; Chaudret, B.; Chauvin, Y.; Basset, J.-M. Organized 3D-alkyl imidazolium ionic liquids could be used to control the size of in situ generated ruthenium nanoparticles? *J. Mater. Chem.* **2009**, *19*, 3624–3631.

[7] Domańska, U. Physico-Chemical Properties and Phase Behaviour of Pyrrolidinium-Based Ionic Liquids. *International Journal of Molecular Sciences* **2010**, *11*, 1825–1841.

[8] Scholten, J. D.; Prechtl, M. H. G.; Dupont, J. Decomposition of Formic Acid Catalyzed by a Phosphine-Free Ruthenium Complex in a Task-Specific Ionic Liquid. *ChemCatChem* **2010**, *2*, 1265–1270.

[9] Arfan, A.; Bazureau, J. P. Efficient Combination of Recyclable Task Specific Ionic Liquid and Microwave Dielectric Heating for the Synthesis of Lipophilic Esters. *Organic Process Research & Development* **2005**, *9*, 743–748.

[10] Visser, A. E.; Swatloski, R. P.; Reichert, W. M.; Mayton, R.; Sheff, S.; Wierzbicki, A.; Davis, Jr., J. H.; Rogers, R. D. Task-specific ionic liquids for the extraction of metal ions from aqueous solutions. *Chem. Commun.* **2001**, 135–136.

[11] Abbott, A. P.; Frisch, G.; Hartley, J.; Ryder, K. S. Processing of metals and metal oxides using ionic liquids. *Green Chem.* **2011**, *13*, 471–481.

[12] Davris, P.; Balomenos, E.; Panias, D.; Paspaliaris, I. *1st European Rare Earth Resources Conference*; 2014 Sept 04-07.

[13] Yang, Z.-Z.; Zhao, Y.-N.; He, L.-N. CO2 chemistry: task-specific ionic liquids for CO2 capture/activation and subsequent conversion. *RSC Adv.* **2011**, *1*, 545–567.

[14] Dai, S.; Shin, Y. S.; Toth, L. M.; Barnes, C. E. Comparative UV−Vis Studies of Uranyl Chloride Complex in Two Basic Ambient-Temperature Melt Systems: The Observation of Spectral and Thermodynamic Variations Induced via Hydrogen Bonding. *Inorganic Chemistry* **1997**, *36*, 4900–4902.

[15] Bell, R. C.; Castleman, A. W.; Thorn, D. L. Vanadium Oxide Complexes in Room-Temperature Chloroaluminate Molten Salts. *Inorganic Chemistry* **1999**, *38*, 5709–5715.

[16] Nockemann, P.; Thijs, B.; Pittois, S.; Thoen, J.; Glorieux, C.; Van Hecke, K.; Van Meervelt, L.; Kirchner, B.; Binnemans, K. Task-Specific Ionic Liquid for Solubilizing Metal Oxides. *The Journal of Physical Chemistry B* **2006**, *110*, 20978–20992.

[17] Nockemann, P.; Thijs, B.; Parac-Vogt, T. N.; Van Hecke, K.; Van Meervelt, L.; Tinant, B.; Hartenbach, I.; Schleid, T.; Ngan, V. T.; Nguyen, M. T.; Binnemans, K. Carboxyl-Functionalized Task-Specific Ionic Liquids for Solubilizing Metal Oxides. *Inorganic Chemistry* **2008**, *47*, 9987–9999.

[18] Abbott, A. P.; Capper, G.; Davies, D. L.; Rasheed, R. K.; Tambyrajah, V. Novel solvent properties of choline chloride/urea mixtures. *Chem. Commun.* **2003**, 70–71.

[19] Abbott, A. P.; Capper, G.; Davies, D. L.; Shikotra, P. Processing metal oxides using ionic liquids. *Mineral Processing and Extractive Metallurgy* **2006**, *115*, 15–18.

[20] Whitehead, J. A.; Lawrance, G. A.; McCluskey, A. 'Green' leaching: recyclable and selective leaching of gold-bearing ore in an ionic liquid. *Green Chem.* **2004**, *6*, 313–315.

[21] Whitehead, J.; Zhang, J.; Pereira, N.; McCluskey, A.; Lawrance, G. Application of 1-alkyl-3-methyl-imidazolium ionic liquids in the oxidative leaching of sulphidic copper, gold and silver ores. *Hydrometallurgy* **2007**, *88*, 109 – 120.

[22] Allinger, N. L.; Yuh, Y. H.; Lii, J. H. Molecular mechanics. The MM3 force field for hydrocarbons. 1. *Journal of the American Chemical Society* **1989**, *111*, 8551–8566.

[23] MacKerell, A. D. et al. All-Atom Empirical Potential for Molecular Modeling and Dynamics Studies of Proteins. *The Journal of Physical Chemistry B* **1998**, *102*, 3586–3616.

[24] MacKerell, A. D.; Banavali, N.; Foloppe, N. Development and current status of the CHARMM force field for nucleic acids. *Biopolymers* **2000**, *56*, 257–265.

[25] Weiner, S. J.; Kollman, P. A.; Case, D. A.; Singh, U. C.; Ghio, C.; Alagona, G.; Profeta, S.; Weiner, P. A new force field for molecular mechanical simulation of nucleic acids and proteins. *Journal of the American Chemical Society* **1984**, *106*, 765–784.

[26] Weiner, S. J.; Kollman, P. A.; Nguyen, D. T.; Case, D. A. An all atom force field for simulations of proteins and nucleic acids. *Journal of Computational Chemistry* **1986**, *7*, 230–252.

[27] Cornell, W. D.; Cieplak, P.; Bayly, C. I.; Gould, I. R.; Merz, K. M.; Ferguson, D. M.; Spellmeyer, D. C.; Fox, T.; Caldwell, J. W.; Kollman, P. A. A Second Generation Force Field for the Simulation of Proteins, Nucleic Acids, and Organic Molecules. *Journal of the American Chemical Society* **1995**, *117*, 5179–5197.

[28] Kollman, P.; Dixon, R.; Cornell, W.; Fox, T.; Chipot, C.; Pohorille, A. In *Computer Simulation of Biomolecular Systems*; van Gunsteren, W., Weiner, P., Wilkinson, A., Eds.; Springer Netherlands, 1997; Vol. 3; pp 83–96.

[29] Jorgensen, W. L.; Maxwell, D. S.; Tirado-Rives, J. Development and Testing of the OPLS All-Atom Force Field on Conformational Energetics and Properties of Organic Liquids. *Journal of the American Chemical Society* **1996**, *118*, 11225–11236.

[30] Gasteiger, J.; Marsili, M. Iterative partial equalization of orbital electronegativity—a rapid access to atomic charges. *Tetrahedron* **1980**, *36*, 3219 – 3228.

[31] Gasteiger, J.; Marsili, M. A new model for calculating atomic charges in molecules. *Tetrahedron Letters* **1978**, *19*, 3181 – 3184.

[32] Jorgensen, W. L.; Tirado-Rives, J. The OPLS [optimized potentials for liquid simulations] potential functions for proteins, energy minimizations for crystals

of cyclic peptides and crambin. *Journal of the American Chemical Society* **1988**, *110*, 1657–1666.

[33] A. Kaminski, G.; L. Jorgensen, W. Host-guest chemistry of rotaxanes and catenanes: application of a polarizable all-atom force field to cyclobis(paraquat-p-phenylene) complexes with disubstituted benzenes and biphenyls [dagger]. *J. Chem. Soc., Perkin Trans. 2* **1999**, 2365–2375.

[34] Canongia Lopes, J. N.; Deschamps, J.; Pádua, A. A. H. Modeling Ionic Liquids Using a Systematic All-Atom Force Field. *The Journal of Physical Chemistry B* **2004**, *108*, 2038–2047.

[35] Shimizu, K.; Almantariotis, D.; Gomes, M. F. C.; Pádua, A. A. H.; Canongia Lopes, J. N. Molecular Force Field for Ionic Liquids V: Hydroxyethylimidazolium, Dimethoxy-2- Methylimidazolium, and Fluoroalkylimidazolium Cations and Bis(Fluorosulfonyl)Amide, Perfluoroalkanesulfonylamide, and Fluoroalkylfluorophosphate Anions. *The Journal of Physical Chemistry B* **2010**, *114*, 3592–3600.

[36] Canongia Lopes, J. N.; Pádua, A. A. H. Molecular Force Field for Ionic Liquids Composed of Triflate or Bistriflylimide Anions. *The Journal of Physical Chemistry B* **2004**, *108*, 16893–16898.

[37] Breneman, C. M.; Wiberg, K. B. Determining atom-centered monopoles from molecular electrostatic potentials. The need for high sampling density in formamide conformational analysis. *Journal of Computational Chemistry* **1990**, *11*, 361–373.

[38] Kollman, P. A. Advances and Continuing Challenges in Achieving Realistic and Predictive Simulations of the Properties of Organic and Biological Molecules. *Accounts of Chemical Research* **1996**, *29*, 461–469.

[39] Mayne, C. G.; Saam, J.; Schulten, K.; Tajkhorshid, E.; Gumbart, J. C. Rapid parameterization of small molecules using the force field toolkit. *Journal of Computational Chemistry* **2013**, *34*, 2757–2770.

[40] Car, R.; Parrinello, M. Unified Approach for Molecular Dynamics and Density-Functional Theory. *Phys. Rev. Lett.* **1985**, *55*, 2471–2474.

Theoretical Study of Alkylsulfonic Acids: Force Field Development and Molecular Dynamics Simulations

2.1 Introduction

Short-chain alkylsulfonic acids (Figure 2.1) have a wide range of applications in industry due to their many desirable properties, including high acidity, solubility and conductivity as well as low toxicity and good biodegradability. As such, methanesulfonic acid (MSA), for example, has been used as a catalyst in organic synthesis such as polymerization, alkylation and esterification.[1,2] Furthermore, its good solubility and conductivity make MSA an ideal electrochemical electrolyte for, e.g., electroplating of Sn/Pb and many flow battery systems.[3–5] A selective electrochemical stripping procedure has also been designed based on MSA.[6]

Ab initio methods have been employed to study physicochemical properties of MSA, such as conformations, heat of formation, and energetics of reactions involving MSA, in the gas phase.[7,8] Structure and energetics of MSA-water clusters and other MSA mixtures have also been investigated.[9–13] While ab initio simulation methods offer the most accurate computational approach with direct access to electronic structural properties, their high computational cost places a significant restriction on their applications. Therefore for large systems—especially solution-phase systems—that require extended simulations, classical methods couched in force fields still provide a very useful approach.

To our knowledge (and to our surprise), force field parameters for alkylsulfonic acids have not been studied though those for many of their derivatives, such as alkylsulfonic acid esters and alkylsulfonate anions, have been developed[14,15] in widely-used force fields, e.g., CHARMM[16] and OPLS.[17] The only exception is MSA, for which a GROMOS-based potential model has been constructed to investigate its structural and dynamic properties, and hydrogen bonded interactions.[18,19] Though this model was able to capture several interesting properties of MSA, its extension to other sul-

fonic acids and/or application to liquid systems containing MSA by utilizing OPLS and CHARMM force fields is not easy; the difference in functional forms of the interaction potentials does not allow for direct combination of its parameters with those of CHARMM or OPLS. Thus it would be worthwhile and desirable to construct a potential model for alkylsulfonic acids, which is compatible with these existing force fields. In this article, we develop two sets of force field parameters—one using CHARMM and one using OPLS protocols—for three short-chain alkylsulfonic acids, methanesulfonic acid (MSA), ethanesulfonic acid (ESA) and 1-propanesulfonic acid (PSA). These new parameter sets are validated via comparison with experimental data and ab initio calculation results. The fact that the structural and transport properties are well captured indicates that our model descriptions can be applied to study various processes, such as electrochemical reaction dynamics, in homogeneous and heterogeneous environments involving these and related solvents.

The outline of this paper is as follows: Details of the force field developments are given in sec 2.2 and classical and ab initio simulation methods are summarized in sec 2.3. In sec 2.4, validation of the force field parameters is presented by comparing simulation results with experimental data and ab initio results. Section 2.5 concludes.

2.2 Force field development

We begin by describing our general strategy for developing potential models for alkylsulfonic acids. The force field parameters for MSA were developed first. The parameters directly available from the CHARMM and OPLS force fields were used without any modifications. Missing parameters were determined by using the force fields for related molecules, in particular, alkylsulfonates, as well as with the aid of ab initio calculations and experimental information (see below for details). With the exception of parameters for one dihedral group involving acidic hydrogen in CHARMM-based

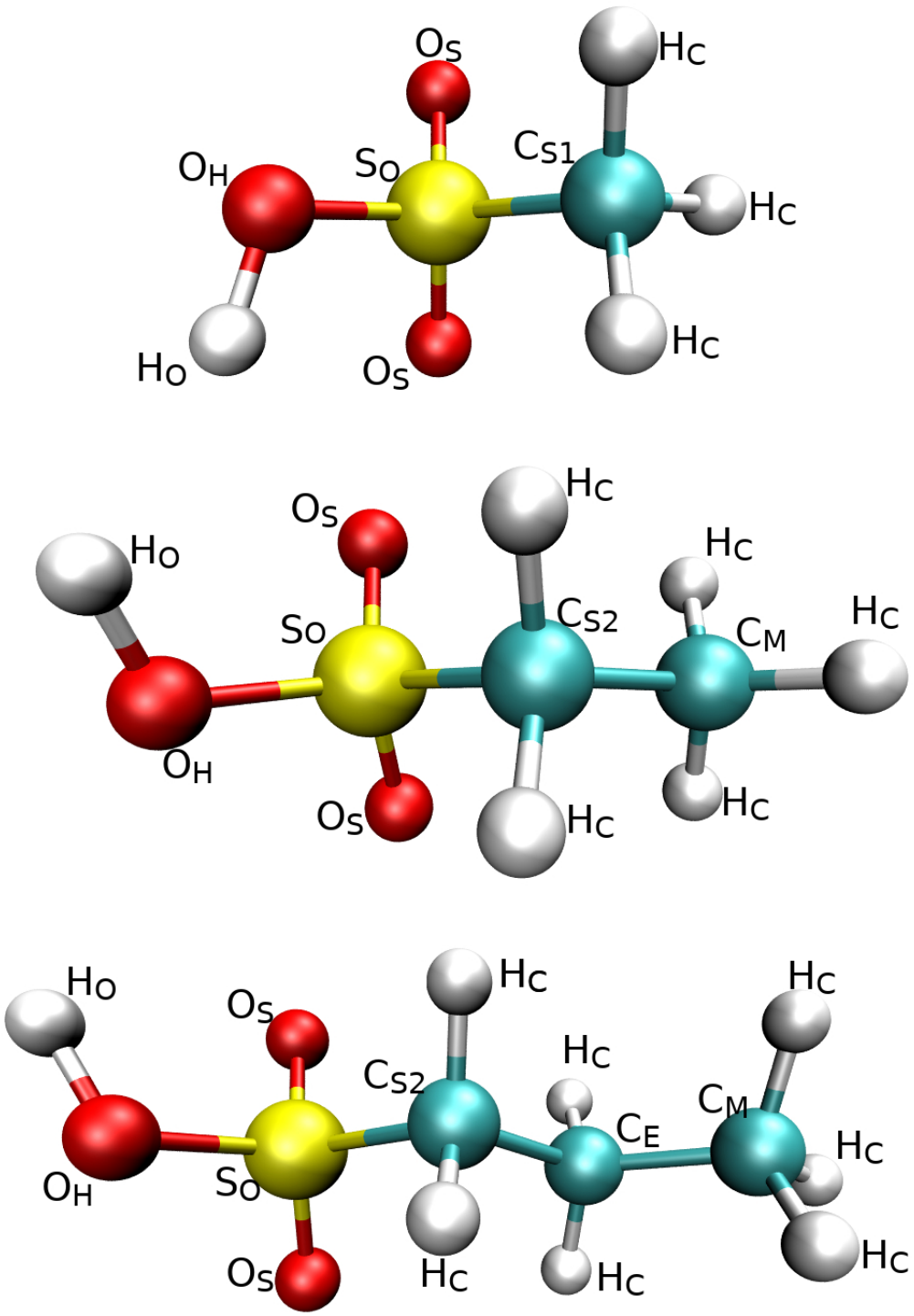

Figure 2.1: Atom types for MSA (top), ESA (middle) and PSA (bottom).

models, optimized parameters of MSA thus constructed were then transferred to ESA and PSA by maintaining charge-neutrality for each of alkyl segments. Complete information on the force field parameters for MSA, ESA and PSA is compiled in Appendix A.3.

We now consider the construction of model potentials based on the CHARMM (eq 2.1) and OPLS (eq 2.2) descriptions in more detail:

$$E = \sum_{i<j,bonds} \frac{1}{2} k^b_{ij} \left(r_{ij} - b_{ij}\right)^2 + \sum_{i<k,angles} \frac{1}{2} k^\theta_{ijk} \left(\theta_{ijk} - \theta^0_{ijk}\right)^2 + \frac{1}{2} k^{UB}_{ijk} \left(r_{ik} - r^0_{ik}\right)^2 + \sum_{i<l,dihedrals} \sum_n k^\phi_{n,ijkl} \left(1 + \cos\left(n\phi - \phi_{n,ijkl}\right)\right) + \sum_{i<j} \left(\frac{q_i q_j}{4\pi\varepsilon_0 r_{ij}} + 4\epsilon_{ij} \left(\left(\frac{\sigma_{ij}}{r_{ij}}\right)^{12} - \left(\frac{\sigma_{ij}}{r_{ij}}\right)^{6} \right) \right) \quad (2.1)$$

$$E = \sum_{i<j,bonds} \frac{1}{2} k^b_{ij} \left(r_{ij} - b_{ij}\right)^2 + \sum_{i<k,angles} \frac{1}{2} k^\theta_{ijk} \left(\theta_{ijk} - \theta^0_{ijk}\right)^2 + \sum_{i<l,dihedrals} \sum_{n=1}^{4} \frac{1}{2} V_{n,ijkl} \left(1 - (-1)^n \cos\left(n\phi_{ijkl}\right)\right) + \sum_{i<j} \left(\frac{q_i q_j}{4\pi\varepsilon_0 r_{ij}} + 4\epsilon_{ij} \left(\left(\frac{\sigma_{ij}}{r_{ij}}\right)^{12} - \left(\frac{\sigma_{ij}}{r_{ij}}\right)^{6} \right) \right) \quad (2.2)$$

The optimized geometries of isolated MSA, ESA and PSA were determined using Gaussian 09 package.[20] Unless otherwise noted, all electronic structure calculations for CHARMM-based parameterization were performed at the MP2/6-31G** level, while those for OPLS were carried out at the B3LYP/6-31G** level.[21–24] We note that these are the methods of choice in the construction of existing CHARMM and OPLS force field parameters. The predictions of our potential models for optimized geometry of MSA are compared with the ab initio results in Table 2.1. Model C and Model O there refer to the force field models we developed based on CHARMM and

OPLS protocols, respectively. Only the results directly related to the parameters of MSA, which are missing in CHARMM and OPLS, are presented. Overall the results of Model C and Model O are in good agreement with ab initio calculations, suggesting that our parameterization is reasonable.

Table 2.1: Optimized geometry of MSA.

Geometry	Model C	Model O	MP2	B3LYP
O_H–H_O	0.97Å	0.97Å	0.97Å	0.97Å
S_O=O_S	1.43Å	1.44Å	1.46Å	1.46Å
S_O–O_H	1.61Å	1.64Å	1.64Å	1.65Å
C_{S1}–S_O	1.76Å	1.79Å	1.77Å	1.79Å
O_S–S_O=O_S	123°	120°	121°	121°
O_S–S_O–O_H	105°	107°	109°	107°
C_{S1}–S_O=O_S	110°	111°	109°	109°
C_{S1}–S_O–O_H	96°	98°	98°	98°
C_{S1}–S_O–O_H–H_O	139°	144°	135°	135°
O_S–S_O–O_H–H_O*	26°/107°	30°/100°	21°/112°	21°/111°

* Torsional angles of two O_S respectively.

The non-bonded parameters for alkylsulfonic acids are listed in Table 2.2. As mentioned above, many of them are already available from CHARMM[14,25–28] or OPLS[15,29,30] force fields and they are used without any modifications to maximize the compatibility of our model descriptions with these force fields. CHARMM requires special non-bonded parameters for 1-4 interactions involving C_{S1}, C_{S2}, C_M and C_E.[25] These 1-4 interaction parameters are given in Appendix A.3. The Lennard-Jones (LJ) interaction parameters, σ and ϵ, follow the combination rules of CHARMM or OPLS, depending on which force-field description our potential model is based on.

To determine the missing parameters for Model C, we proceeded as follows: For the LJ parameters of O_S, O_H and H_O in the sulfonyl group, those of the corresponding atoms of acetic acid were used. The LJ parameters of S_O were taken from neutral sulfur in sulfone, sulfonamide and sulfoxide.[31] Partial charges were assigned following the CHARMM protocol using VMD package and Force Field Toolkit plugin.[32,33]

During the optimization, charges of alkyl hydrogen, methyl carbon and methylene carbon atoms were fixed at 0.09 e, -0.27 e and -0.18 e, where e is the elementary charge. For bonded interactions, the force constants for the S–O_H bond and S–O_H–H bond angle of the sulfonyl group were adjusted with the aid of ab initio calculations to reproduce experimental vibrational spectra.[34,35] Torsional parameters involving H_O, i.e., H–O_H–S–O_S and H–O_H–S–C dihedral parameters, as well as the O_H–H force constant were determined by fitting their potential energy profiles to the ab initio results. Specifically, the H–O_H–S–O_S dihedral parameters and O_H–H force constant were obtained using the ab initio results for MSA and were employed for all three alkylsulfonic acids without any further adjustments. The H–O_H–S–C dihedral parameters, on the other hand, were determined separately for MSA, ESA and PSA. The torsional parameter set for PSA thus determined shows a good transferability to 1-butanesulfonic acid (BSA) though BSA is not investigated in the present study. For all other bonded interactions, CHARMM parameters generated by ParamChem interface[36] with CHARMM General Force Field (CGenFF)[14,26–28] were employed.

For Model O, the LJ parameters of S_O of a sulfonate anion were used without any modification, similar to Model C above. For O_S and O_H, however, the σ and ϵ parameters of acetic acid were further optimized to reproduce experimental results for density and heat of vaporization. This is different from Model C, for which no additional adjustments were made. We note that the resulting σ values of O_S and O_H are similar to the corresponding CHARMM values but their ε values exhibit a significant difference. Partial charges of the sulfonyl group were assigned using the CHELPG method.[37] For S_O and C_{S1}, their charges were adjusted to reproduce experimental density and heat of vaporization. Interestingly, the partial charges of the sulfonyl group thus determined are very close to those of Model C though their optimization protocols differ markedly. Each alkyl hydrogen atom was assigned a partial charge 0.06 e following the OPLS protocol. For bonded interactions, the force

constants for the S–O_H bond and the S–O_H–H and O_H–S–C bond angles were assigned to reproduce experimental vibrational spectra.[34,35] The H–O_H–S–O_S and H–O_H–S–C dihedral parameters were determined by fitting their potential energy profiles to the ab initio results for MSA. We found that the dihedral parameters thus determined capture the ab initio results for torsional potential energy profiles for ESA, PSA and BSA quite well. We therefore used them for ESA and PSA without any additional adjustments in our study. For other bonded interactions, OPLS parameters were used without any modifications.

Table 2.2: Non-bonded parameters of Model C and Model O.

Atom types	q (e)		σ (nm)		ε (kJ/mol)	
	Model C	Model O	Model C	Model O	Model C	Model O
C_{S1}	-0.270[c]	-0.160[*]	0.3653[c]	0.3500[c]	0.3264[c]	0.2761[c]
C_{S2}	-0.180[c]	-0.100[*]	0.3581[c]	0.3500[c]	0.2343[c]	0.2761[c]
C_M	-0.270[c]	-0.180[c]	0.3653[c]	0.3500[c]	0.3264[c]	0.2761[c]
C_E	-0.180[c]	-0.120[c]	0.3581[c]	0.3500[c]	0.2343[c]	0.2761[c]
H_C (C_{S1}, C_M)	0.090[c]	0.060[c]	0.2388[c]	0.2500[c]	0.1004[c]	0.1255[c]
H_C (C_{S2}, C_E)	0.090[c]	0.060[c]	0.2388[c]	0.2500[c]	0.1464[c]	0.1255[c]
S_O	1.034[*]	1.090[*]	0.3564[d]	0.3550[s]	1.4644[d]	1.0460[s]
O_S	-0.484[*]	-0.500[*]	0.3029[a]	0.2990[†]	0.5021[a]	0.8370[†]
O_H	-0.547[*]	-0.580[*]	0.3145[a]	0.3120[‡]	0.8038[a]	0.5860[‡]
H_O	0.481[*]	0.470[*]	0.0400[h]	0.0000[h]	0.1925[h]	0.0000[h]

[*] This work.
[†] This work. Modified from carboxylic acid.
[‡] This work. Modified from alcohol.
[a] Acetic acid.
[c] Alkyl chain.
[d] DMSO[31].
[h] Polar hydrogen.
[s] Alkylsulfonates.[15]

2.3 Simulation Methods

2.3.1 Classical MD

Three different systems comprising, respectively, 512 MSA, 342 ESA and 215 PSA molecules were studied. MD simulations were carried out using GROMACS 5.1 program[38] with cubic boundary conditions applied. The trajectories were integrated with the leap frog algorithm and a time step of 1 fs. The cutoff value used for van der Waals interactions was 14 Å. The particle mesh Ewald method[39] was employed to account for the electrostatic interactions in periodic systems. Each system was first equilibrated at 400K and 1 bar for 5 ns and annealed to 298.15K in 5 ns, followed by a 5 ns simulation to determine the system density (Table 2.3) in the isobaric-isothermal ensemble using the Nosé-Hoover thermostat[40,41] and Parrinello-Rahman barostat.[42] Using the resulting density, the system was then equilibrated for 10 ns in the micro-canonical (NVE) ensemble, followed by a 10 ns production run with configurations saved at every 1 ps. The temperatures in NVE simulations were within a 1% error of the target temperature 298 K.

2.3.2 Ab initio MD

Ab initio MD was performed using CP2K 3.0 package.[43] The system contains 16 MSA molecules in a periodic cubic box with the side length 11.9902 Å to reproduce the experimental density. To ensure good total energy convergence, a timestep of 0.5 fs was employed. DFT with BLYP exchange correlation[22,44] and Goedecker-Teter-Hutter (GTH) pseudopotential[45] with DZVP-MOLOPT basis set[46] was employed to describe interatomic interactions. A cutoff of 400 Ry was used for Gaussian plane wave (GPW) method[47] with NN50 smoothing method. Long range dispersion correlations were incorporated using the DFT-D2 scheme.[48] Wavefunctions were optimized using

the orbital transformation method with IRAC and DIIS minimizer with FULL_ALL preconditioner.[49] Convergence criteria were set to 10^{-6}. Nosé-Hoover thermostat was employed to maintain the system temperature at 298.15 K.

The initial configuration needed for ab initio simulation was prepared via classical MD using the Model O developed here. By employing the ab initio method described above, the system was equilibrated for 5 ps in the canonical ensemble, followed by a 30 ps production run from which averages were computed.

2.4 Results and discussion

2.4.1 Density

The densities ρ calculated from Model C and Model O are compared with experimental results[50] in Table 2.3. In all cases we studied, both model descriptions yield a very good agreement with experiments with errors less than 2 %. Model O shows a particularly good agreement because some of its van der Waals parameters were adjusted from the OPLS values to reproduce the MSA density as explained above. The van der Waals parameters of Model C, on the other hand, are taken directly from the CHARMM force fields without any adjustments and thus it tends to overestimate ρ slightly.

Table 2.3: MD results for density ρ of MSA, ESA and PSA (units: g/cm^3).

System	Model C	Model O	Experiment[†]
MSA	1.5019 ± 0.0005	1.4775 ± 0.0003	1.4812
ESA	1.3491 ± 0.0004	1.3413 ± 0.0006	1.3341
PSA	1.2680 ± 0.0011	1.2489 ± 0.0017	1.2516

[†] Reference 50.

2.4.2 Heat of Vaporization

Heat of vaporization ΔH_{vap} is calculated via[51]

$$\Delta H_{\text{vap}} = [E(g) + k_{\text{B}}T] - E(l) \tag{2.3}$$

where $E(g)$ and $E(l)$ are the potential energies of the system in the gas and liquid phases, respectively, k_{B} is Boltzmann's constant, and T is the system temperature. $E(g)$ was computed by simulating a single molecule in vacuum for 10 ns after 10 ns equilibration.

The MD results for ΔH_{vap} are presented in Table 2.4. The results for MSA are in good accord with the measurement. As in the case of density discussed above, Model C slightly overestimates ΔH_{vap} since no adjustments of the CHARMM parameters were made in its construction in contrast to Model O. Both Model C and Model O predict that ΔH_{vap} increases with the alkyl chain length. This trend is attributed mainly to increasing intermolecular interactions and thus better stabilization as the molecular size grows in the liquid phase. This also leads to higher boiling temperature for larger compounds. A similar trend generally obtains for other organic systems, such as alkanes and carboxylic acids.

Table 2.4: MD results for ΔH_{vap} (units: kJ/mol) for MSA, ESA and PSA at 25 °C

System	Model C	Model O	Experiment
MSA	76.5	74.9	75.2[†]
ESA	79.3	78.5	–
PSA	82.7	81.6	–

[†] Reference 52.

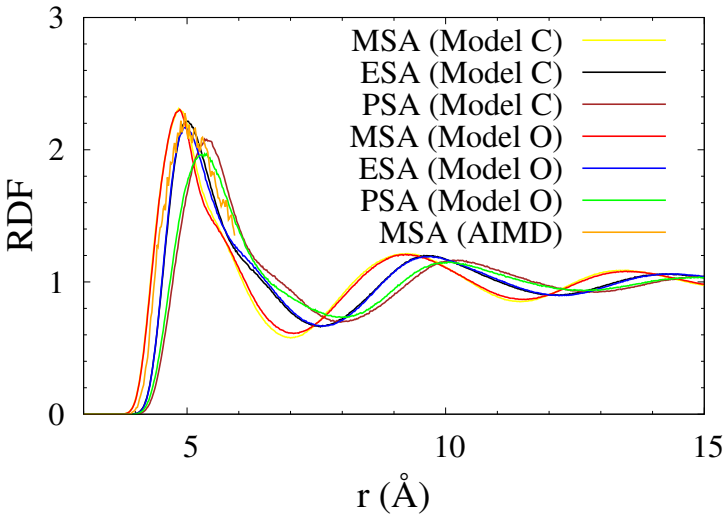

Figure 2.2: COM-to-COM radial distribution functions. Due to its small system size, the range of RDF is very short for ab initio MD simulation.

2.4.3 Structure

We turn to intermolecular structure of alkylsulfonic acids. The results for the radial distribution function (RDF) of the center of mass (COM) of individual molecules are displayed in Figure 2.2. Models C and O yield similar RDFs for all three systems we studied. Specifically, their first peaks are similar in height (~ 2) and position ($\sim 5\,$Å); the first peak position of PSA is shifted to larger distances by only $\sim 0.5\,$Å, compared to MSA. The sulfonic acids studied here can be considered as rod-like (i.e., cylindrical) molecules of a similar radius and thus their COMs can approach each other to a similar proximity. The differences in position of the first minimum as well as the second peak of the RDFs nonetheless reflect the increasing chain length, i.e., height of the cylinder.

RDFs between the sulfonyl oxygen and acidic hydrogen atoms are presented in Figure 2.3. To help the reader, a snapshot of two MSA molecules hydrogen-bonded to each other is shown in Figure 2.4. The O_S–H_O distributions exhibit a prominent peak at 1.7 Å, indicating that O_S and H_O form a strong intermolecular hydrogen bond. The corresponding peak around 1.8 Å in the O_H–H_O distribution is much

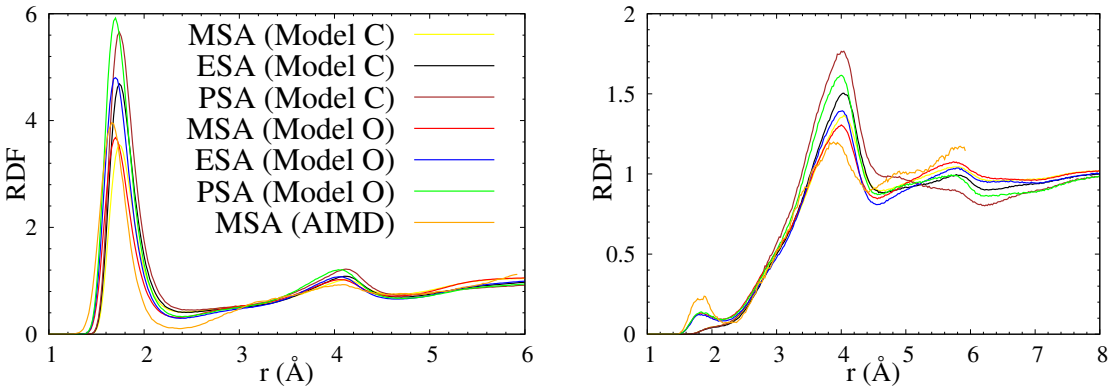

(a) RDF between O_S–H_O (b) RDF between O_H–H_O

Figure 2.3: Radial distribution functions between O and H

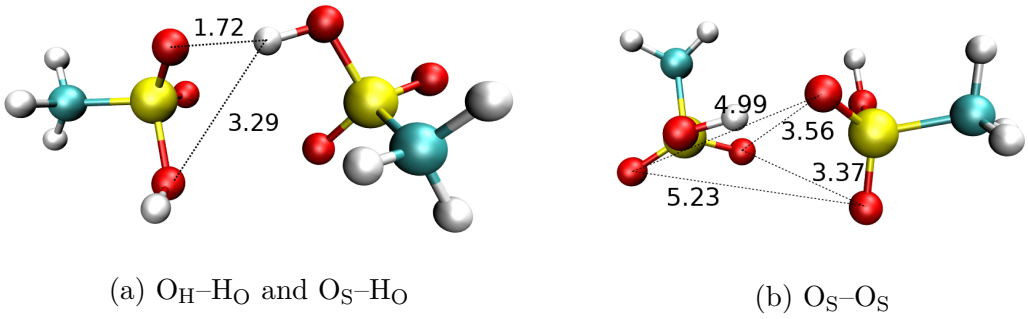

(a) O_H–H_O and O_S–H_O (b) O_S–O_S

Figure 2.4: Snapshot of a hydrogen-bonded pair taken from the AIMD trajectory. Color code: S (yellow), O (red), H (white) and C (green). Units for distance: Å.

lower, revealing that its hydrogen bonding strength is considerably weaker than that of O_S–H_O. The main peak around 4 Å primarily accounts for the distribution of H_O, which is hydrogen-bonded to O_S, around O_H of the molecule that this hydrogen-bonded O_S belongs to, as shown in Figure 2.4a. We notice that for a given sulfonic acid, hydrogen bond peaks are higher in Model O than in Model C. This suggests that the former model yields stronger intermolecular hydrogen bonds than the latter.

For detailed insight, we quantify hydrogen bonds by employing a geometric definition based on the bond distance and angle specifications. Specifically, we consider that a hydrogen bond is formed when the intermolecular hydrogen-oxygen distance is smaller than the first minimum of their RDF, i.e., 2.35 Å, and the angle between the OH bond and the intermolecular O-to-O direction is smaller than 30°. A similar

definition has been used for water systems in previous studies.[53–55] The results for % population of specific hydrogen bonds, viz., the ratio of the number of hydrogen bonds and the total number of OH groups, are given in Table 2.5. CHARMM- and OPLS-based force field models yield a nearly identical % population of O_S–H_O hydrogen bonds for all three sulfonic acids. For O_H–H_O hydrogen bonds, on the other hand, the Model C results are only about 1/3 of the Model O results as is expected from their respective RDF peak heights in Figure 2.3. In the case of MSA, both Models C and O tend to underestimate the hydrogen-bonding interaction compared to the ab initio result. One likely reason is the absence of electronic polarizability in the force field models, which can increase intermolecular electrostatic interactions through induced charges.[56] Despite this difference, the overall agreement between the force field models and ab initio results in the hydrogen bond structures is very reasonable.

Table 2.5: Ratio of the number of hydrogen bonds to the total number of hydrogen bond donors.

	Force field	O_H–H_O	O_S–H_O	Total
MSA	Model C	0.9%	92.0%	93.0%
	Model O	2.4%	91.8%	94.2%
	AIMD	3.9%	93.3%	97.2%
ESA	Model C	0.7%	93.1%	93.8%
	Model O	1.8%	93.5%	95.3%
PSA	Model C	0.6%	93.5%	94.1%
	Model O	1.8%	93.6%	95.4%

To obtain a quantitative understanding of hydrogen-bonded clusters and network that can be formed, we examine the distribution of the number of hydrogen bonds per molecule. From molecular structural perspective, one alkylsulfonic acid can form a maximum of four hydrogen bonds—three as a hydrogen bond acceptor and one as a hydrogen bond donor. According to simulation results, however, one acid molecule forms, on average, two hydrogen bonds—one as an acceptor and one as a donor. Indeed, about 50% of the population shows this behavior of two hydrogen bonds

(Table 2.6), whereas less than 1 % forms four hydrogen bonds. A relatively small amount of alkylsulfonic acids (about 17%) exhibits the formation of three hydrogen bonds and almost twice that amount (about 30%) is characterized by fewer than two hydrogen bonds. The latter population with fewer than two hydrogen bonds is mainly responsible for the termination of the hydrogen bond network. As a result, the average size of hydrogen-bonded clusters is 8–10 molecules, where a hydrogen-bonded cluster is defined as a group of molecules connected by hydrogen bonds.

Table 2.6: Distribution of number of hydrogen bonds per molecule.[†]

	Force field	0	1	2	3
MSA	Model C	3.3%	32.0%	48.0%	16.5%
	Model O	2.6%	30.6%	48.9%	17.5%
	AIMD	1.5%	23.8%	57.1%	17.7%
ESA	Model C	2.6%	30.3%	50.4%	16.6%
	Model O	2.0%	28.9%	51.2%	17.6%
PSA	Model C	2.0%	29.3%	51.1%	17.4%
	Model O	2.2%	29.3%	51.2%	17.0%

[†] The probability of forming four hydrogen bonds per molecule is lower than 1%.

Table 2.7: Size and number of hydrogen-bonded clusters in the simulation system.

	Force field	total number of clusters	average size of clusters
MSA	Model C	68.3	7.6
	Model O	57.3	9.1
	AIMD[*]	1.5	12.8
ESA	Model C	41.1	8.5
	Model O	34.1	10.3
PSA	Model C	23.6	9.4
	Model O	23.7	9.4

[*] AIMD cluster size is not reliable due to small system size.

For quantitation of hydrogen-bonded clusters, we introduce two different probability distributions: (1) probability distribution of the cluster size, $P(n)$, defined as the ratio of the number of hydrogen-bonded clusters of size n to the total number of

clusters, and (2) probability distribution of the number of molecules in clusters of size n, viz., $P_{\mathrm{mol}}(n) = nP(n)/\sum_n nP(n)$, where $\sum_n nP(n)$ is the average cluster size. We also consider their cumulative distribution functions, $\Phi(n) \equiv P(x \leq n) = \sum_{x \leq n} P(x)$ and $\Phi_{\mathrm{mol}}(n) \equiv P_{\mathrm{mol}}(x \leq n) = \sum_{x \leq n} P_{\mathrm{mol}}(x)$. The results are shown in Figure 2.5. $P(n)$ in Figure 2.5a indicates that a significant number of molecules do not form intermolecular hydrogen bonds (viz., clusters of size of 1) and the probability of forming large hydrogen-bonded clusters decreases dramatically as their size increases. As is expected, Model C and Model O show some difference in $P(n)$, especially for $n = 1$ and 2, due to the difference in force field parameters. According to $\Phi(n)$ in Figure 2.5c, less than 10% of the clusters consist of more than 20 molecules, while the clusters with fewer than 10 molecules account for around 75% of the total hydrogen-bonded clusters formed. In terms of the number of molecules, however, only about 30% of the molecules in the system belong to the clusters of size less than 10 (Figure 2.5d). To account for about 80% of the molecules in $\Phi_{\mathrm{mol}}(n)$, the cluster size needs to be increased to $n \approx 50$. This means that despite the high abundance of small clusters, clusters of large size do play an important role. Because of the small system size (16 MSA molecules), we did not analyze the AIMD simulation results for hydrogen-bonded clusters.

Returning to RDFs, we consider oxygen-oxygen distributions in Figure 2.6. The main O_H–O_S peak at ~ 2.7 Å arises from the O_H–$H_O \cdots O_S$ hydrogen bond, while various structures of the O_S–O_S distribution are due to differing O_S-to-O_S separations in the hydrogen-bonded pair (Figure 2.4b). We note that the ab initio and force field results show a discrepancy in the peak positions in the O_S–O_S distribution. This arises mainly from the difference in the relative orientation of two MSA molecules that are hydrogen-bonded to each other (Figure 2.4b). They are in a slightly more twisted conformation in the ab initio MD such that O_S-to-O_S separation becomes elongated compared to the classical force field results.

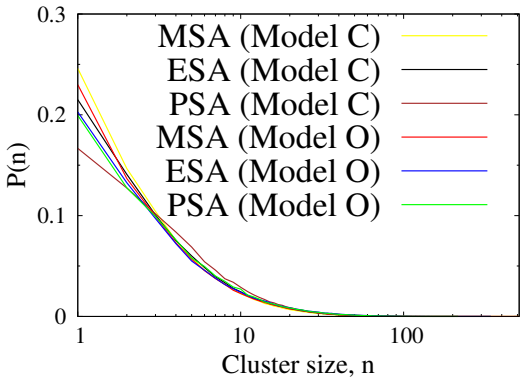

(a) Probability distribution of hydrogen-bonded clusters of size n, $P(n)$

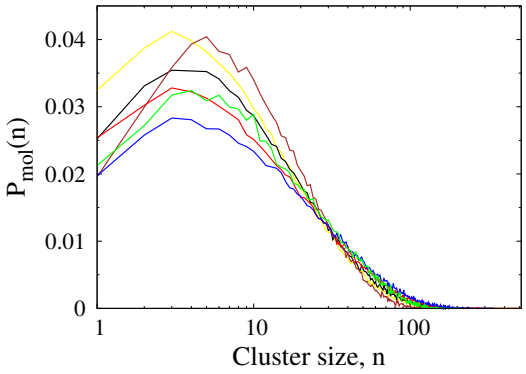

(b) Probability distribution of number of molecules in hydrogen-bonded clusters of size n, $P_{\mathrm{mol}}(n)$

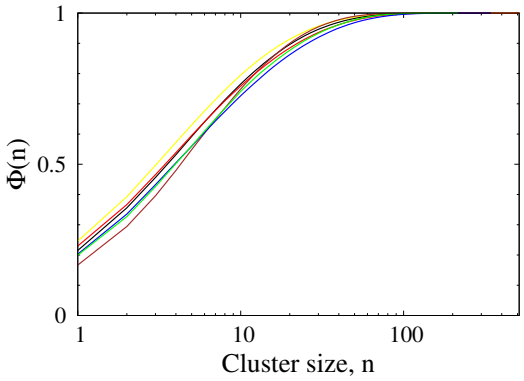

(c) Cumulative distribution function of hydrogen-bonded clusters with size n, $\Phi(n)$

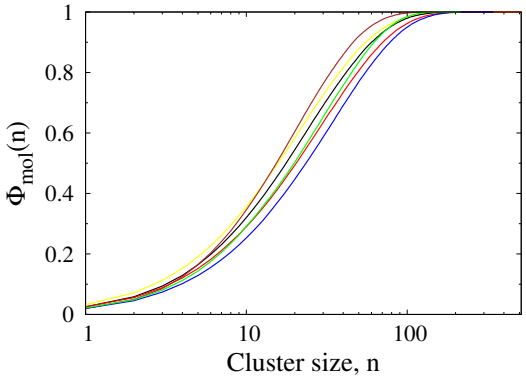

(d) Cumulative distribution function of number of molecules in hydrogen-bonded clusters, $\Phi_{\mathrm{mol}}(n)$

Figure 2.5: Distribution of hydrogen-bonded clusters.

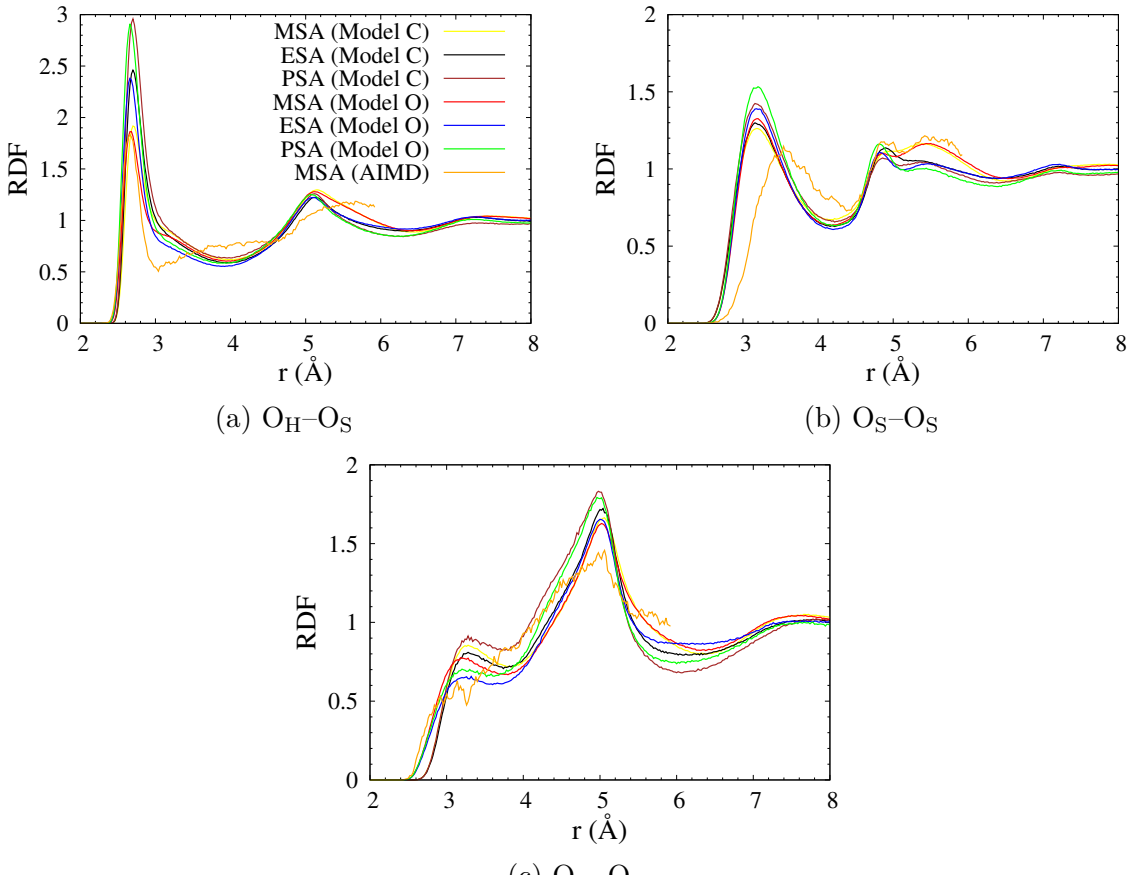

(a) O_H–O_S (b) O_S–O_S

(c) O_H–O_H

Figure 2.6: Radial distribution functions between oxygen atoms.

To further illustrate the structure of alkylsulfonic acids, we have analyzed three-dimensional spatial distribution functions (SDFs). The ab initio and force field results for the acidic hydrogen H_O in MSA are compared in Figure 2.7. Distributions of an open shell shape around two O_S atoms clearly show the formation of strong hydrogen bonds between O_S and H_O. The ring-like distribution around O_H arises from rotations of H_O of the central molecule about its O_H–S_O axis. Though not shown here, there appears a fine structure above this ring-like distribution when the isosurface value for SDF is lowered below 5. The formation of weak intermolecular hydrogen bonds between O_H and H_O discussed above is responsible for this structure (not shown here). Model C on the other hand does not yield any discernible structure even with the isosurface value as low as 1. This is directly related to the aforementioned result that the number of O_H–H_O hydrogen bonds for Model C is much lower than that for Model O (cf. Table 2.5).

SDFs of the terminal carbon atom of the alkyl chain of MSA and PSA in Figure 2.8 show that the distributions of alkyl chains are correlated with intermolecular hydrogen bond distributions. To be specific, alkyl chains tend to be concentrated in the outer regions of the H_O distributions (Figure 2.7), while the aggregation among them is barely noticeable. A near absence of hydrophobic aggregation of alkyl chains is probably due to their relatively short chain lengths. Comparison of the predictions of the two models indicates that the interactions between alkyl groups are stronger in Model C than in Model O, especially for PSA.

2.4.4 Transport properties

Viscosity

Shear viscosity is calculated using non-equilibrium MD (NEMD) with the periodic perturbation method (PPM), which has been employed for a wide range of different

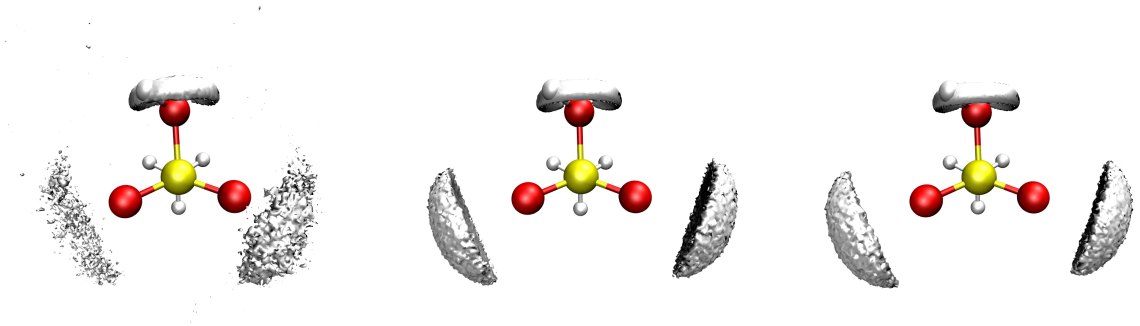

(a) AIMD (b) Model C (c) Model O

Figure 2.7: Spatial distribution of H_O in MSA: (a) AIMD, (b) Model C and (c) Model O. Isodensity surface values are 20 for AIMD and 10 for classical MD.

systems, including Lennard-Jones fluids,[57,58] ionic liquids,[59] and organic liquids.[60,61] PPM creates a velocity field in the system by applying a periodic force in the form of $\lambda \cos(kz)$ along the x-direction of the simulation cell. While ideally λ should be very small so that the system remains close to equilibrium, a sizable amplitude is needed to establish a significant velocity field for efficient and accurate calculations. We employed multiple λ values in the range $\sim$ 0.1–0.3 nm/ps^2 for each of the systems we studied (see Figure 2.9). The shear viscosities at these λ values were determined via[57–61]

$$\eta = \frac{\lambda \rho}{u_0 k^2} \; ; \qquad u_x(z,t) = u_0 \cos(kz) \tag{2.4}$$

with the velocity profile $u_x(z,t)$ obtained from non-equlibrium MD and were extrapolated to $\lambda = 0$ to obtain the equilibrium shear viscosity. The viscosity at each λ value was computed by averaging over 11 different trajectories, each of which was simulated for 1 ns after a 1 ns equilibration. Berendsen thermostat was applied to remove the heat generated by the external force.[62] Due to large errors in η for small λ, especially for ESA and PSA, $\lambda < 0.1$ nm/ps^2 was not considered for these two sulfonic acids (Figure 2.9).

MD and experimental results for shear viscosity are presented in Table 2.8. To the best of our knowledge, the experimental results are available only for MSA. The

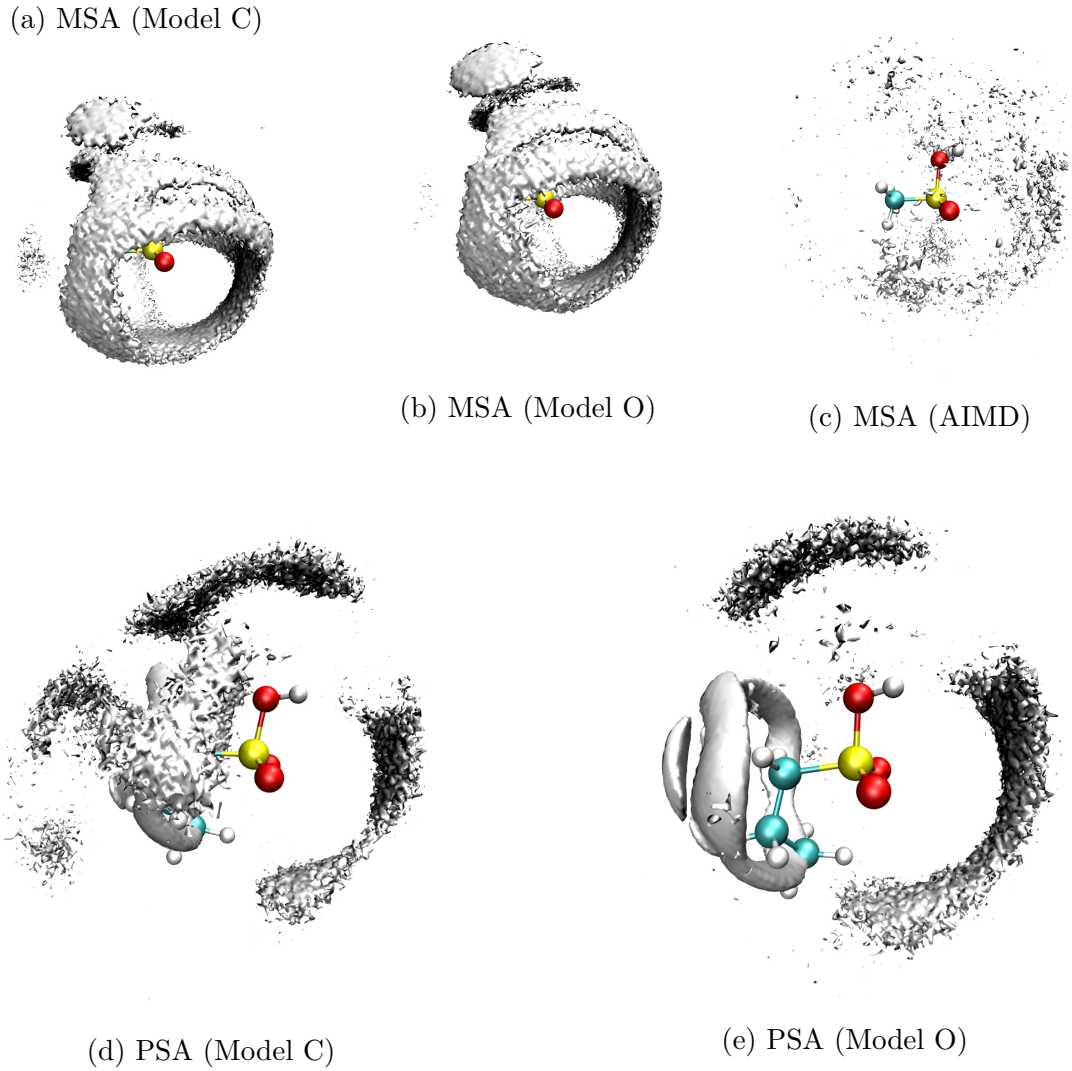

(a) MSA (Model C)

(b) MSA (Model O)

(c) MSA (AIMD)

(d) PSA (Model C)

(e) PSA (Model O)

Figure 2.8: Spatial distribution of the terminal carbon atom of the alkyl chain of MSA and PSA—i.e., C_{S1} of MSA and C_M of PSA (Figure 2.1)—around a central solvent molecule. The ring-like structure around the alkyl chain of the central PSA molecule in (d) and (e) represents the distribution of its own C_M. Color code: S (yellow), O (red), H (white) and C (green). Isodensity surface values are 10 for AIMD and 3 for classical MD.

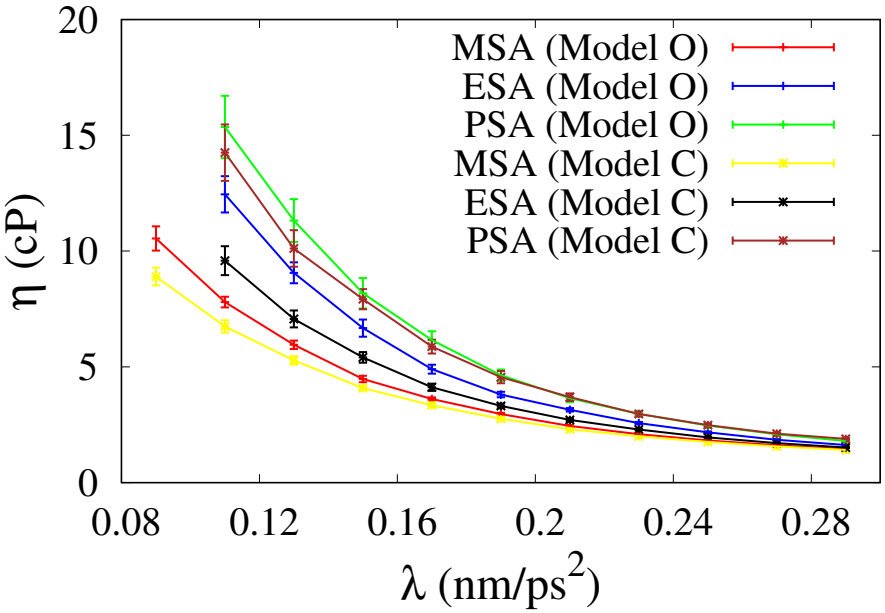

Figure 2.9: Shear viscosities of MSA, ESA and PSA at different acceleration amplitudes.

results of both Models C and O compare reasonably well with the measurements, indicating our potential models provide a reasonable framework to study transport properties of alkylsulfonic acids.

Table 2.8: Shear viscosities of MSA, ESA and PSA (units: cP).

system	Model C	Model O	Experiment
MSA	10.0 ± 1.0	11.7 ± 1.2	11.2[†]
ESA	12.1 ± 1.3	15.6 ± 1.8	–
PSA	18.0 ± 2.0	19.6 ± 2.2	–

[†] Reference 63.

Translational diffusion

Diffusion coefficients are calculated using the Einstein relation

$$D = \lim_{t\to\infty} \frac{\langle R^2(t)\rangle}{6t} \tag{2.5}$$

where $R^2(t)$ is the square displacement of the center of mass of a molecule during time t and $\langle \ldots \rangle$ denotes an equilibrium ensemble average. Results are presented in Table 2.9. Sulfonic acids with longer chains diffuse more slowly. As is expected from the Stokes-Einstein relation, the diffusion coefficients show the trend exactly the opposite of viscosities in Table 2.8.

Table 2.9: Diffusion coefficients of MSA, ESA and PSA.

D (10^{-11} m^2/s)	Model C	Model O
MSA	6.36 ± 0.19	5.04 ± 0.29
ESA	4.48 ± 0.13	2.59 ± 0.20
PSA	2.59 ± 0.21	2.47 ± 0.08

2.5 Concluding Remarks

In this article, we have developed force field descriptions, Model C and Model O, for small alkylsulfonic acids, based on CHARMM and OPLS parameters and protocols, respectively. The MD results for methanesulfonic acid, ethanesulfonic acid and 1-propanesulfonic acid obtained with these potential models show a good agreement with the available experimental information. Compared to the AIMD results for methanesulfonic acid, both Model C and Model O underestimate its hydrogen bond structure slightly. This was attributed to the neglect of electronic polarizability in the force field descriptions. Nonetheless, they yield a good overall agreement with AIMD, indicating that Model C and Model O offer reliable descriptions for alkylsulfonic acids, compatible with OPLS and CHARMM force fields.

[1] Gora, M.; Kozik, B.; Jamrozy, K.; Luczynski, M. K.; Brzuzan, P.; Wozny, M. Solvent-free condensations of ketones with malononitrile catalysed by methanesulfonic acid/morpholine system. *Green Chem.* **2009**, *11*, 863–867.

[2] Subramanian, L. R.; Hanack, M.; García Martínez, A.; Kreilein, M. M. *Encyclopedia of Reagents for Organic Synthesis*; John Wiley & Sons, Ltd, 2001.

[3] D. Gernon, M.; Wu, M.; Buszta, T.; Janney, P. Environmental benefits of methanesulfonic acid. Comparative properties and advantages. *Green Chem.* **1999**, *1*, 127–140.

[4] Hazza, A.; Pletcher, D.; Wills, R. A novel flow battery: A lead acid battery based on an electrolyte with soluble lead(II) Part I. Preliminary studies. *Phys. Chem. Chem. Phys.* **2004**, *6*, 1773–1778.

[5] Na, Z.; Xu, S.; Yin, D.; Wang, L. A cerium-lead redox flow battery system employing supporting electrolyte of methanesulfonic acid. *Journal of Power Sources* **2015**, *295*, 28–32.

[6] Chen, J. Selective electrolytic stripping of metal coatings from base metal substrates. 1987; https://www.google.com/patents/US4678552, US Patent 4,678,552.

[7] Wang, L.; Zhang, J. Ab initio calculation on thermochemistry of CH_3SO_xH (x=1-3) and H_2SO_y (y=2,3). *Journal of Molecular Structure: THEOCHEM* **2002**, *581*, 129–138.

[8] Carvalho, N. A. F.; Silva, S. A. P.; Resende, S. M. Theoretical determination of the properties of methanesulfinic and methanesulfonic acids. *Journal of the Brazilian Chemical Society* **2011**, *22*, 950–954.

[9] Wang, L. Clusters of hydrated methane sulfonic acid $CH_3SO_3H{\cdot}(H_2O)_n$ (n = 1-5): A theoretical study. *The Journal of Physical Chemistry A* **2007**, *111*, 3642–3651.

[10] Krishtal, A.; Senet, P.; Van Alsenoy, C. Influence of structure on the polarizability of hydrated methane sulfonic acid clusters. *Journal of Chemical Theory and Computation* **2008**, *4*, 2122–2129.

[11] Givan, A.; Loewenschuss, A.; Nielsen, C. J. Infrared spectrum and ab initio calculations of matrix isolated methanesulfonic acid species and its 1:1 water complex. *Journal of Molecular Structure* **2005**, *748*, 77–90.

[12] Lehtonen, O.; Hartikainen, J.; Rissanen, K.; Ikkala, O.; Pietilä, L.-O. Hydrogen bonding and protonation in acid-base complexes: Methanesulfonic acid-pyridine. *The Journal of Chemical Physics* **2002**, *116*, 2417–2424.

[13] Xu, J.; Finlayson-Pitts, B. J.; Gerber, R. B. Proton transfer in mixed clusters of methanesulfonic acid, methylamine, and oxalic acid: implications for atmospheric particle formation. *The Journal of Physical Chemistry A* **2017**, *121*, 2377–2385.

[14] Yu, W.; He, X.; Vanommeslaeghe, K.; MacKerell, A. D. Extension of the CHARMM general force field to sulfonyl-containing compounds and its utility in biomolecular simulations. *Journal of Computational Chemistry* **2012**, *33*, 2451–2468.

[15] Canongia Lopes, J. N.; Pádua, A. A. H.; Shimizu, K. Molecular force field for ionic liquids IV: Trialkylimidazolium and alkoxycarbonyl-imidazolium cations; alkylsulfonate and alkylsulfate anions. *The Journal of Physical Chemistry B* **2008**, *112*, 5039–5046.

[16] MacKerell, A. D. et al. All-atom empirical potential for molecular modeling and dynamics studies of proteins. *The Journal of Physical Chemistry B* **1998**, *102*, 3586–3616.

[17] Jorgensen, W. L.; Maxwell, D. S.; Tirado-Rives, J. Development and testing of the OPLS all-atom force field on conformational energetics and properties of organic liquids. *Journal of the American Chemical Society* **1996**, *118*, 11225–11236.

[18] Canales, M.; Alemán, C. Molecular dynamics simulation study of methanesulfonic acid. *The Journal of Physical Chemistry B* **2014**, *118*, 3423–3430.

[19] Canales, M.; Guàrdia, E. A comparative molecular dynamics study of sulfuric and methanesulfonic acids. *Journal of Molecular Liquids* **2016**, *224*, 1064–1073.

[20] Frisch, M. J. et al. Gaussian 09 Revision A.02. Gaussian Inc. Wallingford CT 2009.

[21] Becke, A. D. A new mixing of Hartree-Fock and local density-functional theories. *The Journal of Chemical Physics* **1993**, *98*, 1372–1377.

[22] Lee, C.; Yang, W.; Parr, R. G. Development of the Colle-Salvetti correlation-energy formula into a functional of the electron density. *Phys. Rev. B* **1988**, *37*, 785–789.

[23] Hehre, W. J.; Ditchfield, R.; Pople, J. A. Self-consistent molecular orbital methods. XII. Further extensions of Gaussian-type basis sets for use in molecular orbital studies of organic molecules. *The Journal of Chemical Physics* **1972**, *56*, 2257–2261.

[24] Hariharan, P.; Pople, J. The influence of polarization functions on molecular orbital hydrogenation energies. *Theoretica Chimica Acta* **1973**, *28*, 213–222.

[25] MacKerell, A. D.; Banavali, N.; Foloppe, N. Development and current status of the CHARMM force field for nucleic acids. *Biopolymers* **2000**, *56*, 257–265.

[26] Vanommeslaeghe, K.; MacKerell, A. D. Automation of the CHARMM general force field (CGenFF) I: Bond perception and atom typing. *Journal of Chemical Information and Modeling* **2012**, *52*, 3144–3154.

[27] Vanommeslaeghe, K.; Raman, E. P.; MacKerell, A. D. Automation of the CHARMM general force field (CGenFF) II: Assignment of bonded parameters and partial atomic charges. *Journal of Chemical Information and Modeling* **2012**, *52*, 3155–3168.

[28] Vanommeslaeghe, K.; Hatcher, E.; Acharya, C.; Kundu, S.; Zhong, S.; Shim, J.; Darian, E.; Guvench, O.; Lopes, P.; Vorobyov, I.; Mackerell, A. D. CHARMM general force field: A force field for drug-like molecules compatible with the CHARMM all-atom additive biological force fields. *Journal of Computational Chemistry* **2010**, *31*, 671–690.

[29] Shimizu, K.; Almantariotis, D.; Gomes, M. F. C.; Pádua, A. A. H.; Canongia Lopes, J. N. Molecular force field for ionic liquids V: Hydroxyethylimidazolium, dimethoxy-2-methylimidazolium, and fluoroalkylimidazolium cations and bis(fluorosulfonyl)amide, perfluoroalkanesulfonylamide, and fluoroalkylfluorophosphate anions. *The Journal of Physical Chemistry B* **2010**, *114*, 3592–3600.

[30] Canongia Lopes, J. N.; Pádua, A. A. H. Molecular force field for ionic liquids composed of triflate or bistriflylimide anions. *The Journal of Physical Chemistry B* **2004**, *108*, 16893–16898.

[31] Strader, M. L.; Feller, S. E. A flexible all-atom model of dimethyl sulfoxide for molecular dynamics simulations. *The Journal of Physical Chemistry A* **2002**, *106*, 1074–1080.

[32] Humphrey, W.; Dalke, A.; Schulten, K. VMD – Visual molecular dynamics. *Journal of Molecular Graphics* **1996**, *14*, 33–38.

[33] Mayne, C. G.; Saam, J.; Schulten, K.; Tajkhorshid, E.; Gumbart, J. C. Rapid parameterization of small molecules using the force field toolkit. *Journal of Computational Chemistry* **2013**, *34*, 2757–2770.

[34] Chackalackal, S. M.; Stafford, F. E. Infrared spectra of methane-, fluoro-, and chlorosulfonic acids. *Journal of the American Chemical Society* **1966**, *88*, 4815–4819.

[35] Luo, J.; Hu, J.; Saak, W.; Beckhaus, R.; Wittstock, G.; Vankelecom, I. F. J.; Agert, C.; Conrad, O. Protic ionic liquid and ionic melts prepared from methanesulfonic acid and 1H-1,2,4-triazole as high temperature PEMFC electrolytes. *J. Mater. Chem.* **2011**, *21*, 10426–10436.

[36] ParamChem. https://www.paramchem.org/.

[37] Breneman, C. M.; Wiberg, K. B. Determining atom-centered monopoles from molecular electrostatic potentials. The need for high sampling density in formamide conformational analysis. *Journal of Computational Chemistry* **1990**, *11*, 361–373.

[38] van der Spoel, D.; Lindahl, E.; Hess, B.; Groenhof, G.; Mark, A. E.; Berendsen, H. J. C. GROMACS: Fast, flexible, and free. *Journal of Computational Chemistry* **2005**, *26*, 1701–1718.

[39] Darden, T.; York, D.; Pedersen, L. Particle mesh Ewald: An N·log(N) method for Ewald sums in large systems. *The Journal of Chemical Physics* **1993**, *98*, 10089–10092.

[40] Nosé, S. A unified formulation of the constant temperature molecular dynamics methods. *The Journal of Chemical Physics* **1984**, *81*, 511–519.

[41] Nosé, S. A molecular dynamics method for simulations in the canonical ensemble. *Molecular Physics* **1984**, *52*, 255–268.

[42] Parrinello, M.; Rahman, A. Polymorphic transitions in single crystals: A new molecular dynamics method. *Journal of Applied Physics* **1981**, *52*, 7182–7190.

[43] Hutter, J.; Iannuzzi, M.; Schiffmann, F.; VandeVondele, J. cp2k: atomistic simulations of condensed matter systems. *Wiley Interdisciplinary Reviews: Computational Molecular Science* **2014**, *4*, 15–25.

[44] Becke, A. D. Density-functional exchange-energy approximation with correct asymptotic behavior. *Phys. Rev. A* **1988**, *38*, 3098–3100.

[45] Goedecker, S.; Teter, M.; Hutter, J. Separable dual-space Gaussian pseudopotentials. *Phys. Rev. B* **1996**, *54*, 1703–1710.

[46] VandeVondele, J.; Hutter, J. Gaussian basis sets for accurate calculations on molecular systems in gas and condensed phases. *The Journal of Chemical Physics* **2007**, *127*, 114105.

[47] Lippert, B. G.; Hutter, J.; Parrinello, M. A hybrid Gaussian and plane wave density functional scheme. *Molecular Physics* **1997**, *92*, 477–488.

[48] Grimme, S. Semiempirical GGA-type density functional constructed with a long-range dispersion correction. *Journal of Computational Chemistry* **2006**, *27*, 1787–1799.

[49] VandeVondele, J.; Hutter, J. An efficient orbital transformation method for electronic structure calculations. *The Journal of Chemical Physics* **2003**, *118*, 4365–4369.

[50] Haynes, W. M., Ed. *CRC Handbook of Chemistry and Physics*, 95th ed.; CRC Press, 2014.

[51] Caleman, C.; van Maaren, P. J.; Hong, M.; Hub, J. S.; Costa, L. T.; van der Spoel, D. Force field benchmark of organic liquids: density, enthalpy of vaporization, heat capacities, surface tension, isothermal compressibility, volumetric expansion coefficient, and dielectric constant. *Journal of Chemical Theory and Computation* **2012**, *8*, 61–74.

[52] Guthrie, J. P.; Stein, A. R.; Huntington, A. P. Thermodynamics of methanesulfonic acid, methanesulfonyl chloride, and methyl methanesulfonate. *Canadian Journal of Chemistry* **1998**, *76*, 929–936.

[53] Bursulaya, B. D.; Kim, H. J. Molecular dynamics simulation study of water near critical conditions. I. Structure and solvation free energetics. *The Journal of Chemical Physics* **1999**, *110*, 9646–9655.

[54] Mountain, R. D. Molecular dynamics investigation of expanded water at elevated temperatures. *The Journal of Chemical Physics* **1989**, *90*, 1866–1870.

[55] Mountain, R. D. Comparison of a fixed-charge and a polarizable water model. *The Journal of Chemical Physics* **1995**, *103*, 3084–3090.

[56] Bursulaya, B. D.; Zichi, D. A.; Kim, H. J. Molecular dynamics simulation study of polarizable solute solvation in water. 1. Equilibrium solvent structure and solute rotational dynamics. *The Journal of Physical Chemistry* **1996**, *100*, 1392–1405.

[57] Hess, B. Determining the shear viscosity of model liquids from molecular dynamics simulations. *The Journal of Chemical Physics* **2002**, *116*, 209–217.

[58] Vasquez, V. R.; Macedo, E. A.; Zabaloy, M. S. Lennard-Jones viscosities in wide ranges of temperature and density: Fast calculations using a steady-state periodic perturbation method. *International Journal of Thermophysics* **2004**, *25*, 1799–1818.

[59] Hu, Z.; Margulis, C. J. On the response of an ionic liquid to external perturbations and the calculation of shear viscosity. *The Journal of Physical Chemistry B* **2007**, *111*, 4705–4714.

[60] Zhao, L.; Wang, X.; Wang, L.; Sun, H. Prediction of shear viscosities using periodic perturbation method and OPLS force field. *Fluid Phase Equilibria* **2007**, *260*, 212–217, 3rd Fluid Properties Challenge.

[61] Zhao, L.; Cheng, T.; Sun, H. On the accuracy of predicting shear viscosity of molecular liquids using the periodic perturbation method. *The Journal of Chemical Physics* **2008**, *129*, 144501.

[62] Berendsen, H. J. C.; Postma, J. P. M.; van Gunsteren, W. F.; DiNola, A.; Haak, J. R. Molecular dynamics with coupling to an external bath. *The Journal of Chemical Physics* **1984**, *81*, 3684–3690.

[63] Roitman, D. B.; McAlister, J.; Oaks, F. L. Composition characterization of methanesulfonic acid. *Journal of Chemical & Engineering Data* **1994**, *39*, 56–60.

Theoretical Study of Possible Pathways of ZnO Dissolution in Ionic Liquid, 1-methyl-1-(4'-sulfonylbutyl)-pyrrolidinium chloride

3.1 Introduction

In 2017, transportation accounts for 29% of total energy consumed in US. Fossil fuel responsible for 92% energy needed in transportation. Combustion emission of carbon oxide in addition to nitrogen oxide and sulfur oxide has huge negative impacts on the environment.[1] Zinc-air fuel cell (ZAFC) is one of alternative energy sources to fossil fuel. It converts zinc to zinc oxide in basic condition while producing electricity.[2–4] The potential application of ZAFC to power eletricial vehecles can mitigate the environmental impacts.

Regeneration of zinc in ZAFC is both environmentally crucial and cost beneficial. Traditionally, electrolysis and carbothermal method are the main approaches to reduce zinc from zinc oxide. The former method often first disolves zinc oxide in acidic or basic solutions, and after purification, zinc is produced through electrolysis.[3,4] The latter one involves reducing zinc in zinc oxide with carbon under high temperature.[3]

Use of ILs, including imidazolium-based and betaine-based ILs, as a leaching agent for metal oxides has been reported previously.[5–10] Other IL cations, such as imidazolium- and cyclic alkyl quaternary ammonium-based cations, can be functionalized with a carboxyl group to achieve the selective dissolution.[11] Eutectic mixture of choline chloride and hydrogen bond donors, such as carboxylic acids, amines and alcohols and urea is also a novel efficient solvent for mineral leaching.[12,13] Sulfonic acid based ionic liquids were used mainly as catalysts at low concentration due to their high melting points and viscosities.[14,15] Recently a new sulfonic acid functionalized ionic liquid was synthesized with relatively low viscosity and could be used undiluted.[15]

In this chapter, we propose using 1-methyl-1-(4'-sulfonylbutyl)pyrrolidinium chloride (MSP-Cl) as a leaching agent for disolving zinc oxide for electrolysis. Reaction barrier of proton transfer from MSP cation to bare zinc oxide surfaces are examined

using nudged elastic band method (NEB). Reaction energies of zinc ion dissociation after protonation is also studied.

3.2 Simulation Methods

All ab initio calculations in this paper were performed using CP2K package.[16] Our systems contained 48 ZnO units. ZnO surfaces, $(10\bar{1}0)$ and $(11\bar{2}0)$, are shown in Figure 3.2, respectively. DFT with BLYP exchange correlation[17,18] and Goedecker-Teter-Hutter (GTH) pseudopotential[19] with DZVP-MOLOPT basis set[20] was employed to describe interatomic interactions. A cutoff of 700 Ry was used for Gaussian plane wave (GPW) method[21]. Long range dispersion correlations were incorporated using the DFT-D2 scheme.[22] Wavefunctions were optimized using the orbital transformation method with IRAC and DIIS minimizer with FULL_ALL preconditioner.[23] Two-dimensional periodic boundary condition was implemented using wavelet method.[24] At least 10 Å empty space was left at both ends of the non-periodic direction. Convergence criteria were set to 10^{-6}.

Geometry minimization using BFGS method was employed to obtain the optimized geometry and energy. Convergence criteria were set such that the maximum force on each atom was smaller than 10^{-4} Bohr/Hartree.

D-NEB[25], a variant of nudged elastic band method, was employed to determine the energy profile of proton transfer from MSP to bare ZnO surfaces. The method was chosen primarily due to its convergence speed. 24 images including reactant and product state were used.

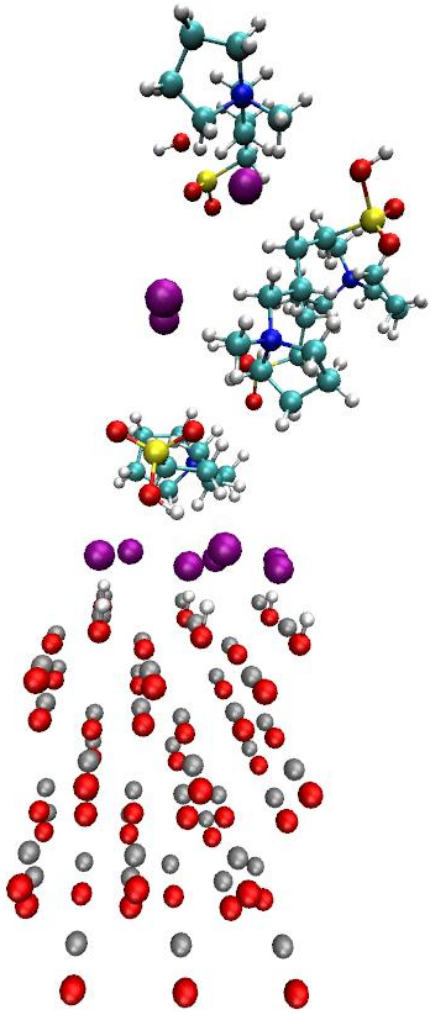

Figure 3.1: System configuration. Purple is chloride, oxygen is red, grey is zinc, white is hydrogen, cyan is carbon and blue is nitrogen.

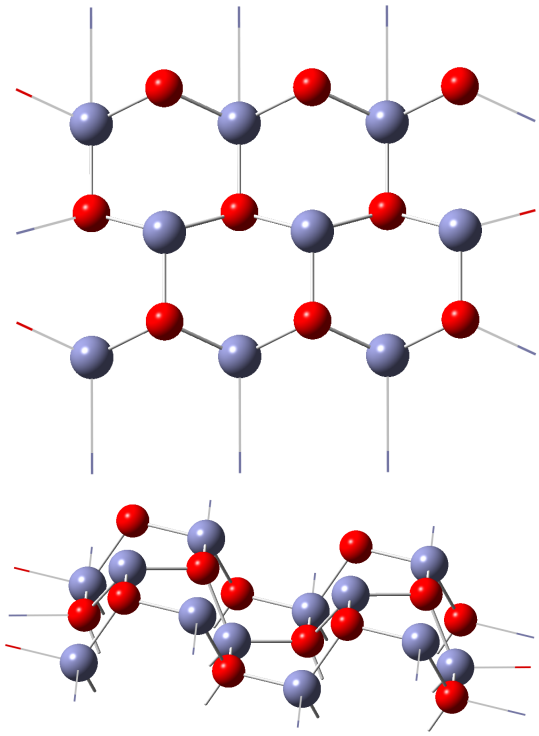

Figure 3.2: ZnO surfaces, $(10\bar{1}0)$ (top) and $(11\bar{2}0)$ (bottom).

3.3 Results and discussion

3.3.1 Protonation on ZnO Surface

Protonation on ZnO surfaces in water environment has been previoussly studied[26–31]. In more acidic environment, e.g. the presence of alkyl sulfonic acids, proton transfer from the acidic sulfonic acid group to ZnO surface should be much easier. Hence, in this section, we examine the reaction energies of the protonation on ZnO $(10\bar{1}0)$ surfaces.

All the possible combinations of the protontated ZnO surfaces are listed in Figure 3.3. The reaction energies of proton transfer from MSP to ZnO surfaces are listed in Table 3.1. We note that, due to the small system size, the configurations of systems are likely limited by the periodic boundary condition. Larger systems with more combinations could yield reaction energies closer to the real scenario. However, the

increasing number of combinations and system size make DFT calculations infeasible.

The overall trend suggests that the reaction energies of proton transfer increase with respect to the number of protons on the surfaces. The decrease in the magnitude of reaction energy could be caused by the accumulated positive charges on the ZnO surface. The reaction energies of transfering the first two protons to bare ZnO surfaces are significantly larger than those of subsequent proton transfer. The transfer of the sixth proton is not energetically favorable. Thus, the likely equilibrium structure could be protonation of five of the six oxygen sites. Some reactions involving unfavorable products, e.g. 2-1 to 3-1, are not included in the table.

For surfaces with the same number of protons, generally protons tend to maximize their distances to reduce electrostatic repulsion. Chloride anions bind to the zinc atoms closest to the protons.

3.3.2 Energy barrier using NEB

The reaction energy of proton transfer to a bare ZnO surface found to be -118.0 kJ/mol for ZnO $(10\bar{1}0)$ surface (0-1 in Figure 3.3) and -161.0 kJ/mol for ZnO $(11\bar{2}0)$ surface. Surprisingly, NEB did not yield a barrier for the proton transfer to ZnO $(10\bar{1}0)$ surface, while for ZnO $(11\bar{2}0)$ surface, the barrier height is 26.3 kcal/mol.

3.3.3 The dissolution of zinc ion

After the protonation of the ZnO surface, there are two main possiblities for the zinc dissolution step: (1) dissolve zinc ion first, then form water; (2) form water first, then dissolve zinc ion. In this section, we explore these two possiblities. Our calculations support that pathway (1) is the likely mechanism.

Table 3.1: Reaction energies (kJ/mol) of proton transfer from MSP to ZnO·nHCl $(10\bar{1}0)$ surfaces forming ZnO·nHCl-H^+ and Zn^{2+} leaving ZnO·nHCl-H^+ surfaces. The first column are the number of protons on the initial ZnO surfaces, ZnO·$(HCl)_n$ as shown in Figure 3.3. The energy of proton transfer to the initial ZnO surface forming ZnO·$(HCl)_n$-H^+ is shown in the third column with pattern code in parentheses. The energy of pulling a Zn^{2+} ion from the ZnO·$(HCl)_n$-H^+ surface formed before is shown in the fourth column with pattern code in parentheses.

Number of protons (n) on the initial surface	Initial pattern of protons (see Figure 3.3)	Proton transfer energy from MSP to ZnO·$(HCl)_n$ surfaces (pattern of products)	Zn^{2+} leaving ZnO·$(HCl)_n$-H^+ surfaces (pattern of products)
n=0	0-1	-118.00 (1-1)	47.08 (1-1a)
n=1	1-1	-73.76 (2-2)	-4.52 (2-2a)*
		-97.67 (2-3)	50.84 (2-3a)
		-46.43 (2-1)	–
n=2	2-1	-34.6 (3-2)	42.03 (3-2a)
	2-2	-55.75 (3-3)	57.58 (3-3a)
		-30.59 (3-2)	17.18 (3-2b)*
	2-3	-40.99 (3-3)	54.99 (3-3b)*
n=3	3-1	-55.17 (4-1)	31.07 (4-1a)
	3-2	-47.83 (4-3)	45.19 (4-3a)
			18.00 (4-3b)
		-27.02 (4-1)	31.07 (4-1a)
	3-3	-25.98 (4-1)	–
		-34.90 (4-3)	–
		7.78 (4-2)	28.09
n=4	4-1	-37.35 (5-1)	51.66 (5-1a)
	4-2	-23.62 (5-1)	72.36 (5-1b)
	4-3	-8.1 (5-1)	48.11 (5-1c)
n=5	5-1	18.39 (6-1)	-29.1 (6-1a)

* Znic ion is on the ZnO surface, not fully solvated.

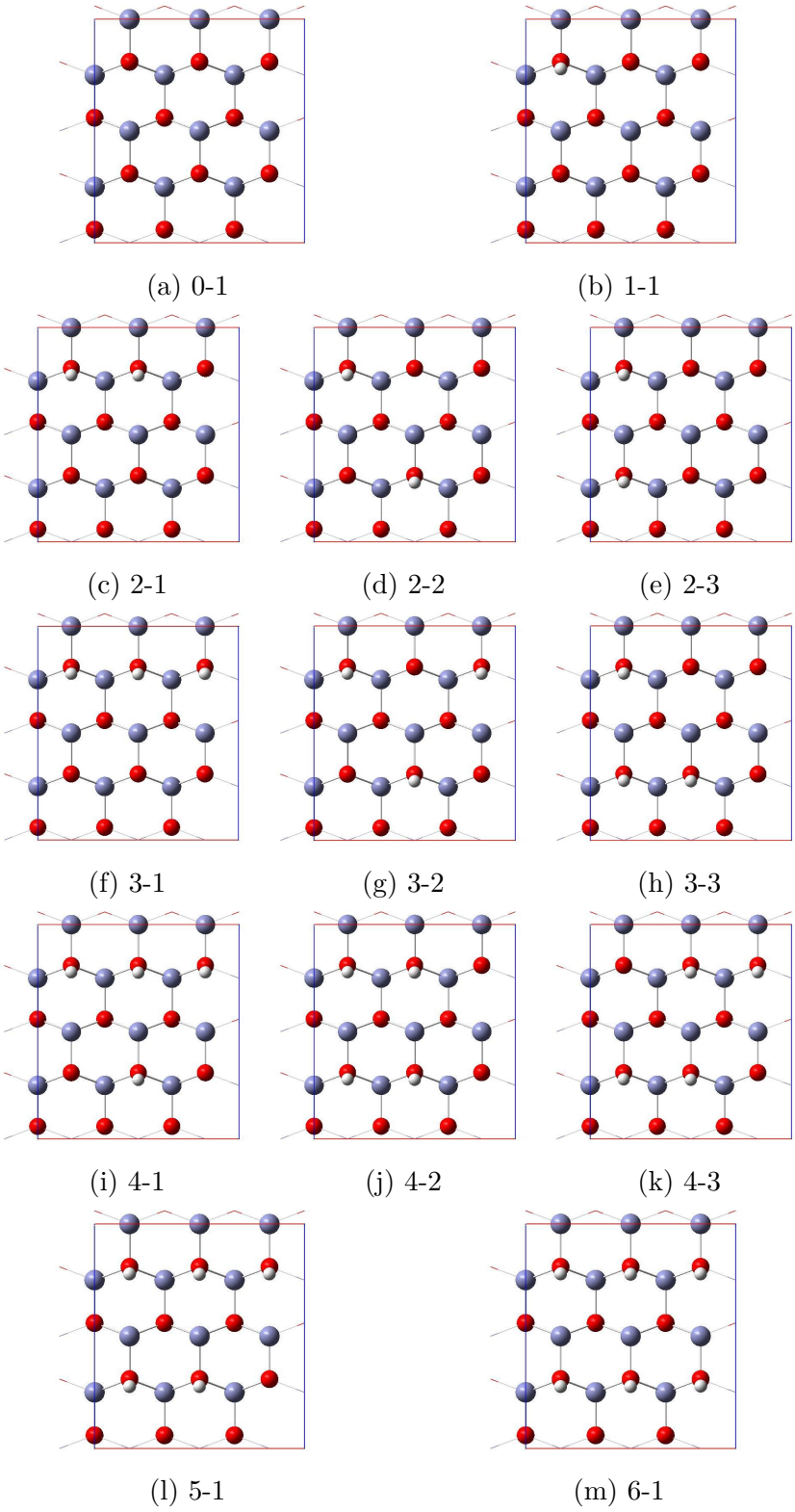

(a) 0-1 (b) 1-1

(c) 2-1 (d) 2-2 (e) 2-3

(f) 3-1 (g) 3-2 (h) 3-3

(i) 4-1 (j) 4-2 (k) 4-3

(l) 5-1 (m) 6-1

Figure 3.3: Labels of ZnO surfaces. The first number is the number of proton on a ZnO surface.

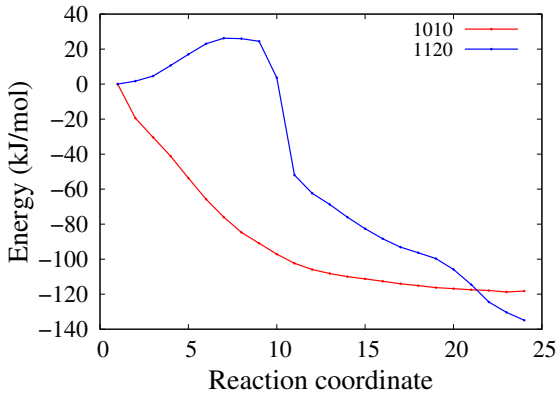

Figure 3.4: Reaction energy profile of proton transfer from MSP to bare ZnO surface.

Zinc dissolution first

In the 4th column of Table 3.1, we present some of the reaction energies of dissolving one zinc ion into the first solvation shell. From one to five protons on the surfaces, the dissolution energies of one zinc ion are positive. The magnitude of the dissolution energies is typicially 30-50 kJ/mol with a few exceptions. Some of these exceptions are surface reconstruction, which will be discussed in section 3.3.3 below. When all the oxygen sites are protonated, the reaction energy of dissolving one zinc ion becomes -29.1 kJ/mol. It is worth noting that the sixth proton transfer is not energetically favorable (18.39 kJ/mol), which can be considered as an energy barrier for the dissolution process.

Water formation first

We examine the possiblity of forming water after all the oxygen sites on ZnO surface are protonated, e.g. 6-1 in Figure 3.3, in this section. There are two reasons that we did not calculate the energies of water formation before all the oxygen sites on ZnO surface are protonated. First, the proton transfer energies to oxygen sites are very negative. Second, there have been several reports[26–31] that ZnO surface can dissociate water. Thus, we focus on forming water with surface 6-1.

The reaction energy of forming water on surface 6-1 is around 70 kJ/mol, and the reaction energy of subsequent protonation of this water molecule forming hydronium ion is about -20 kJ/mol. It is clear that forming water before zinc dissolution is highly unfavorable. It is likely due to the accumulated positive charges on ZnO surface.

Surface reconstruction

While studing how zinc ions enter the solution phase, we also notice that in certain cases, zinc ions do not fully leave the surfaces. Instead zinc ions move to other positions and leave a vacancy at their original places, e.g. 2-2a (Figure 3.5).The energy of 2-2a is near zero, which suggests that reconstruction of the surfaces is possible during dissolution process. However, due to a large number of possible structures in surface reconstruction, we did not explore this pathway.

3.4 Concluding Remarks

In this chapter, we examined the possible dissolution pathways of ZnO in an acidic sulfonic acid based ionic liquid. The reaction energies of proton transfer from the acidic ionic liquids to ZnO surfaces were calcuated. We also showed that zinc ions are likely dissolved after all oxygen sites on ZnO surfaces are protonated. Our results also suggests that zinc ions are dissolved first, and then water is formed. We also noticed the ions on the surfaces may reoragnize during the dissolution process.

This study is limited to the initial steps of ZnO dissolution because of the large number of potential configurations of ZnO surfaces. When more computational resource is available, it would gain more details if the system size and number of dissolved zinc ions could be increased.

However, due to the high cost of ab initio simulations and a large number of ZnO surface configurations, our analysis is limited to a small number of likely reaction pathways. Thus, it would be worthwhile in the future to extend the present study to

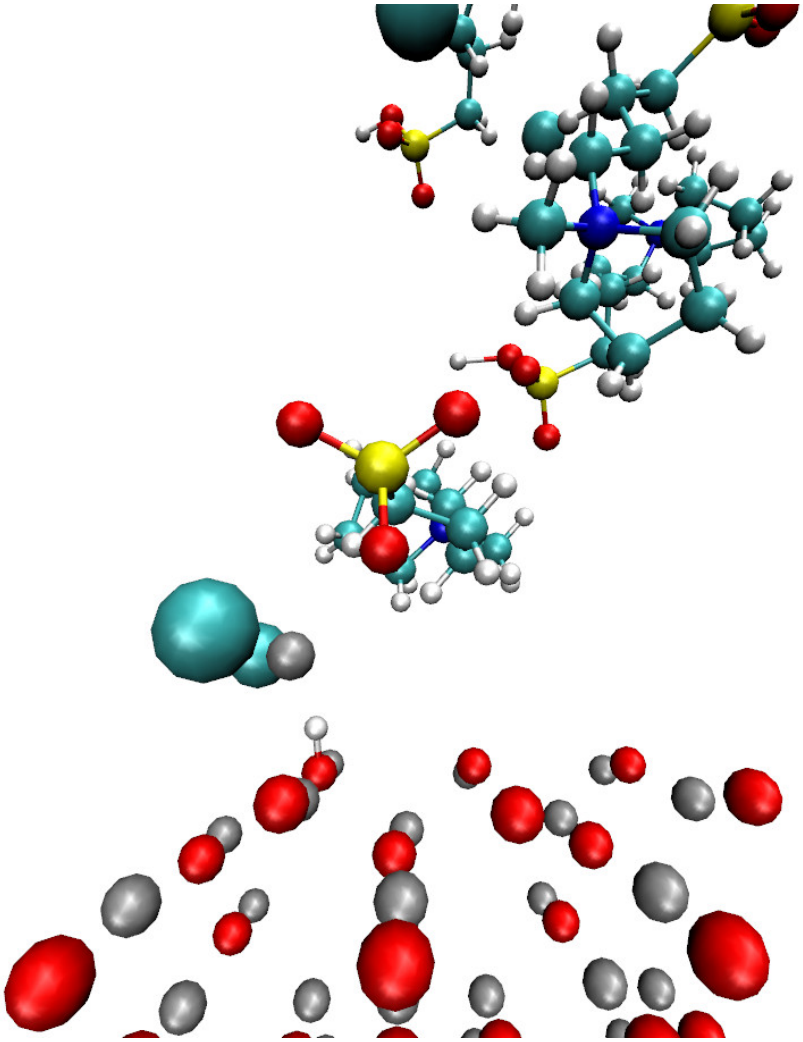

Figure 3.5: Structure of 2-2a. Grey: Zn; red: O; Yellow: S; Blue: N; Turquoise: Cl; Cyan: C.

other configureations to gain more complete insight into ZnO dissolution.

[1] https://www.eia.gov/energyexplained/?page=us_energy_transportation.

[2] Sapkota, P.; Kim, H. Zinc–air fuel cell, a potential candidate for alternative energy. *Journal of Industrial and Engineering Chemistry* **2009**, *15*, 445 – 450.

[3] Li, Y.; Dai, H. Recent advances in zinc–air batteries. *Chem. Soc. Rev.* **2014**, *43*, 5257–5275.

[4] Zhu, A. L.; Wilkinson, D. P.; Zhang, X.; Xing, Y.; Rozhin, A. G.; Kulinich, S. A. Zinc regeneration in rechargeable zinc-air fuel cells–A review. *Journal of Energy Storage* **2016**, *8*, 35 – 50.

[5] Dai, S.; Shin, Y. S.; Toth, L. M.; Barnes, C. E. Comparative UV—Vis Studies of Uranyl Chloride Complex in Two Basic Ambient-Temperature Melt Systems: The Observation of Spectral and Thermodynamic Variations Induced via Hydrogen Bonding. *Inorganic Chemistry* **1997**, *36*, 4900–4902.

[6] Bell, R. C.; Castleman, A. W.; Thorn, D. L. Vanadium Oxide Complexes in Room-Temperature Chloroaluminate Molten Salts. *Inorganic Chemistry* **1999**, *38*, 5709–5715.

[7] Nockemann, P.; Thijs, B.; Pittois, S.; Thoen, J.; Glorieux, C.; Van Hecke, K.; Van Meervelt, L.; Kirchner, B.; Binnemans, K. Task-Specific Ionic Liquid for Solubilizing Metal Oxides. *The Journal of Physical Chemistry B* **2006**, *110*, 20978–20992.

[8] Abbott, A. P.; Frisch, G.; Hartley, J.; Ryder, K. S. Processing of metals and metal oxides using ionic liquids. *Green Chem.* **2011**, *13*, 471–481.

[9] Whitehead, J. A.; Lawrance, G. A.; McCluskey, A. 'Green' leaching: recyclable and selective leaching of gold-bearing ore in an ionic liquid. *Green Chem.* **2004**, *6*, 313–315.

[10] Whitehead, J.; Zhang, J.; Pereira, N.; McCluskey, A.; Lawrance, G. Application of 1-alkyl-3-methyl-imidazolium ionic liquids in the oxidative leaching of sulphidic copper, gold and silver ores. *Hydrometallurgy* **2007**, *88*, 109–120.

[11] Nockemann, P.; Thijs, B.; Parac-Vogt, T. N.; Van Hecke, K.; Van Meervelt, L.; Tinant, B.; Hartenbach, I.; Schleid, T.; Ngan, V. T.; Nguyen, M. T.; Binnemans, K. Carboxyl-Functionalized Task-Specific Ionic Liquids for Solubilizing Metal Oxides. *Inorganic Chemistry* **2008**, *47*, 9987–9999.

[12] Abbott, A. P.; Capper, G.; Davies, D. L.; Rasheed, R. K.; Tambyrajah, V. Novel solvent properties of choline chloride/urea mixtures. *Chem. Commun.* **2003**, 70–71.

[13] Abbott, A. P.; Capper, G.; Davies, D. L.; Shikotra, P. Processing metal oxides using ionic liquids. *Mineral Processing and Extractive Metallurgy* **2006**, *115*, 15–18.

[14] Zare, A.; Abi, F.; Moosavi-Zare, A. R.; Beyzavi, M. H.; Zolfigol, M. A. Synthesis, characterization and application of ionic liquid 1,3-disulfonic acid imidazolium hydrogen sulfate as an efficient catalyst for the preparation of hexahydroquinolines. *Journal of Molecular Liquids* **2013**, *178*, 113 – 121.

[15] Dupont, D.; Raiguel, S.; Binnemans, K. Sulfonic acid functionalized ionic liquids for dissolution of metal oxides and solvent extraction of metal ions. *Chem. Commun.* **2015**, *51*, 9006–9009.

[16] Hutter, J.; Iannuzzi, M.; Schiffmann, F.; VandeVondele, J. cp2k: atomistic simulations of condensed matter systems. *Wiley Interdisciplinary Reviews: Computational Molecular Science* **2014**, *4*, 15–25.

[17] Becke, A. D. Density-functional exchange-energy approximation with correct asymptotic behavior. *Phys. Rev. A* **1988**, *38*, 3098–3100.

[18] Lee, C.; Yang, W.; Parr, R. G. Development of the Colle-Salvetti correlation-energy formula into a functional of the electron density. *Phys. Rev. B* **1988**, *37*, 785–789.

[19] Goedecker, S.; Teter, M.; Hutter, J. Separable dual-space Gaussian pseudopotentials. *Phys. Rev. B* **1996**, *54*, 1703–1710.

[20] VandeVondele, J.; Hutter, J. Gaussian basis sets for accurate calculations on molecular systems in gas and condensed phases. *The Journal of Chemical Physics* **2007**, *127*, 114105.

[21] Lippert, B. G.; Hutter, J.; Parrinello, M. A hybrid Gaussian and plane wave density functional scheme. *Molecular Physics* **1997**, *92*, 477–488.

[22] Grimme, S. Semiempirical GGA-type density functional constructed with a long-range dispersion correction. *Journal of Computational Chemistry* **2006**, *27*, 1787–1799.

[23] VandeVondele, J.; Hutter, J. An efficient orbital transformation method for electronic structure calculations. *The Journal of Chemical Physics* **2003**, *118*, 4365–4369.

[24] Genovese, L.; Deutsch, T.; Goedecker, S. Efficient and accurate three-dimensional Poisson solver for surface problems. *The Journal of Chemical Physics* **2007**, *127*, 054704.

[25] Trygubenko, S. A.; Wales, D. J. A doubly nudged elastic band method for finding transition states. *The Journal of Chemical Physics* **2004**, *120*, 2082–2094.

[26] Meyer, B.; Marx, D.; Dulub, O.; Diebold, U.; Kunat, M.; Langenberg, D.; Wöll, C. Partial Dissociation of Water Leads to Stable Superstructures on the Surface of Zinc Oxide. *Angewandte Chemie International Edition* **2004**, *43*, 6641–6645.

[27] Cooke, D. J.; Marmier, A.; Parker, S. C. Surface Structure of (10$\bar{1}$0) and (11$\bar{2}$0) Surfaces of ZnO with Density Functional Theory and Atomistic Simulation. *The Journal of Physical Chemistry B* **2006**, *110*, 7985–7991, PMID: 16610898.

[28] Dulub, O.; Meyer, B.; Diebold, U. Observation of the Dynamical Change in a Water Monolayer Adsorbed on a ZnO Surface. *Phys. Rev. Lett.* **2005**, *95*, 136101.

[29] Newberg, J. T.; Goodwin, C.; Arble, C.; Khalifa, Y.; Boscoboinik, J. A.; Rani, S. ZnO(10$\bar{1}$0) Surface Hydroxylation under Ambient Water Vapor. *The Journal of Physical Chemistry B* **2018**, *122*, 472–478, PMID: 28800394.

[30] Kenmoe, S.; Biedermann, P. U. Water aggregation and dissociation on the ZnO(10$\bar{0}$) surface. *Phys. Chem. Chem. Phys.* **2017**, *19*, 1466–1486.

[31] Quaranta, V.; Hellström, M.; Behler, J. Proton-Transfer Mechanisms at the Water–ZnO Interface: The Role of Presolvation. *The Journal of Physical Chemistry Letters* **2017**, *8*, 1476–1483, PMID: 28296415.

Heterogeneous Dynamics of Ionic Liquids: A Four-Point Time Correlation Function Approach

4.1 Introduction

It is no surprise that the use of ionic liquids (ILs) – salts that exist in a molten state below 100°C – has been tested and shows promise in a broad range of applications.[1–5] Unusual and often desirable properties such as chemical and thermal stability, high effective polarity, nonvolatility, wide electrochemical window, *etc.*, make them ideal for a variety of specialized tasks. Furthermore, by judiciously engineering functional groups or exchanging ions entirely, the possibility arises for generating customizable ILs.

Parallel to a material's applicability comes interest in the underlying molecular behavior. Many experimental[6–23] and computational[23–40] studies have reported dynamic behavior of different ILs, revealing an array of interesting features, indicating their dynamics are heterogeneous. The examples include spatially-correlated dynamics, sub-diffusive translational motions, non-diffusive reorientational dynamics, non-exponential solvent relaxation, *etc.* These dynamic behaviors, except for spatially-correlated dynamics, have been analyzed using theoretical approaches based on two-point time correlation functions, such as van Hove functions.

In this paper, we extend previous computational efforts to gain further insight into heterogeneity of IL dynamics by using a time-dependent four-point density correlation function.[41] This approach enables, for example, the investigation of the cooperative IL dynamics and the related dynamic length scale for spatial correlation, not accessible via two-point time correlation functions. While four-point time correlation functions have been used to characterize the dynamic behavior of structurally correlated species in glass-like systems,[41–50] their application to ILs has been extremely limited.[51]

Here, we study time evolution of correlated motions in choline acetate ([Cho][Ac]) and 1-butyl-3-methylimidazolium acetate ([BMI][Ac]) (Figure 4.1) as a protype of

Reprinted from J. Chem. Phys., **2018**, *148*, 193830, with the permission of AIP Publishing.

hydroxylic and non-hydroxylic ILs, respectively. For comparison, acetonitrile is considered as a standard nonglassy solvent.

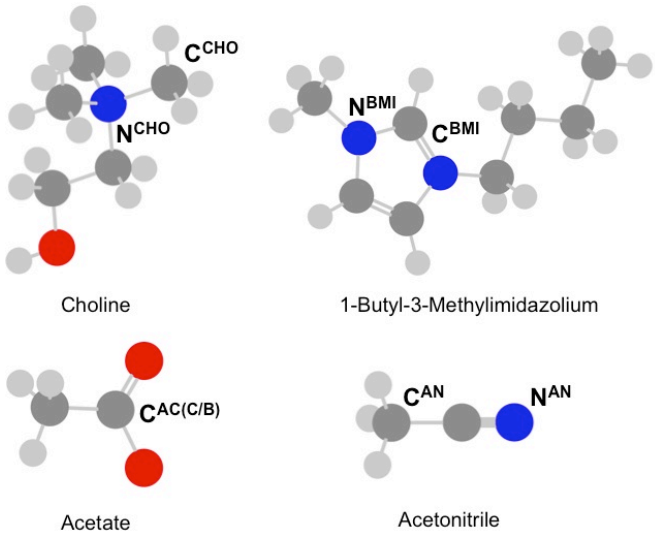

Figure 4.1: Notation used throughout this work. The parenthetical letter in $C^{AC(C/B)}$ indicates if the acetate ion is paired with choline ($C^{AC(C)}$) or BMI ($C^{AC(B)}$).

4.2 Simulation Models and Methods

Details of the simulation systems are compiled in Table 4.1. Three trajectories of each IL system listed there and one trajectory of acetonitrile were simulated with the GROMACS simulation package.[52–55] As in Ref. 38, we used CHARMM force field parameters for ILs, generated via ParamChem v.0.9.7 interface[58] that automatically assigns atom types, force field parameters and charges on molecules based on the 2b8 release of the CHARMM General Force Field.[59–61] We note that the density of [BMI][Ac] determined with these parameters shows a very good agreement with the available experimental data (Table 4.1). For acetonitrile, the potential model developed in Ref 62 was employed. Electrostatic interactions were computed using the particle mesh Ewald (PME) method with a 1.4 nm cut-off. Nosé-Hoover temperature coupling and Parrinello-Rahman pressure coupling were used to maintain

Table 4.1: Simulation Systems: N refers to the number of ion pairs for ILs, while it refers to the number of molecules for acetonitrile; n is the average number density; ρ and ρ_{exp} are simulated and experimental densities; D is the diffusion coefficient of acetate anion and acetonitrile calculated using Einstein equation and Time indicates the length of each production trajectory.

Solvent	T (K)	N	n (nm^{-3})	ρ (g/cm^3)	ρ_{exp} (g/cm^3)	D ($10^{-12}\text{m}^2/\text{s}$)	Time (ns)
[Cho][Ac]	350	256	4.149	1.124	-	0.13	200
[BMI][Ac]	350	512	3.099	1.020	1.0192*	0.27	150
[Cho][Ac]	400	256	4.079	1.106	-	3.0	30
[BMI][Ac]	400	512	3.026	0.993	-	7.1	20
[Cho][Ac]	600	256	3.737	1.013	-	4.4×10^2	10
CH_3CN	300	512	11.387	0.776	0.7857**	3.5×10^3	0.5

* 353 K, Ref 56.
** 298 K, Ref 57.

constant temperature and pressure of the system, respectively. For [Cho][Ac], initial configurations for each simulation were generated by annealing the system in the isothermal-isobaric (NPT) ensemble from 700 K, and then equilibrating at production temperature for 6 ns for 400 K and 350 K simulations and 2 ns for 600 K in the canonical (NVT) ensemble. The initial structures of [BMI][Ac] were prepared by annealing the system from 800 K in the NPT ensemble, followed by equilibration at production temperatures for 10 ns. The acetonitrile simulation was preceded by 0.2 ns of equilibration in the NVT ensemble at production temperature. All production runs were performed in the NVT ensemble.

4.3 Results and Discussion

4.3.1 Radial Distribution Function

We start by considering the static structure of the system in the form of the radial distribution function (RDF), $g_{AB}(r)$, *i.e.*,

$$g_{AB}(\vec{r}) = \frac{V}{N_A N_B} \sum_{i \in A} \sum_{j \in B} \delta\left(\vec{r} - \vec{r}_{ij}\right), \tag{4.1}$$

where i and j represent individual particles and A and B denote species. MD results for RDFs are displayed at 400 K for [Cho][Ac] and [BMI][Ac] and at 300 K for acetonitrile in Figure 4.2. Higher temperature RDFs resemble those displayed in Figure 4.2, but may show minor variations in peak positions and dimensions. For reference, the position (r') and the height ($g(r')$) of the first peak in each RDF are displayed in Table 4.2.

The ILs show prominent oscillatory behavior beyond 1 nm. This is generally attributed to an alternating-charge shell structure, *i.e.*, cations tend to be surrounded by anions which, in turn, tend to be surrounded by cations.[63] This oscillatory behavior can be found in acetonitrile to a slightly reduced degree – the amplitude of oscillations is smaller and they extend to shorter distances.

4.3.2 Spatial Distribution Function

To obtain insight into the anisotropic character of relative distributions of ions, we considered three-dimensional spatial distribution functions (SDFs). The results for cation distributions around the acetate anion are presented as isodensity surfaces in Figure 4.3 as an example. The isodensity values are chosen to highlight the first solvation shells.

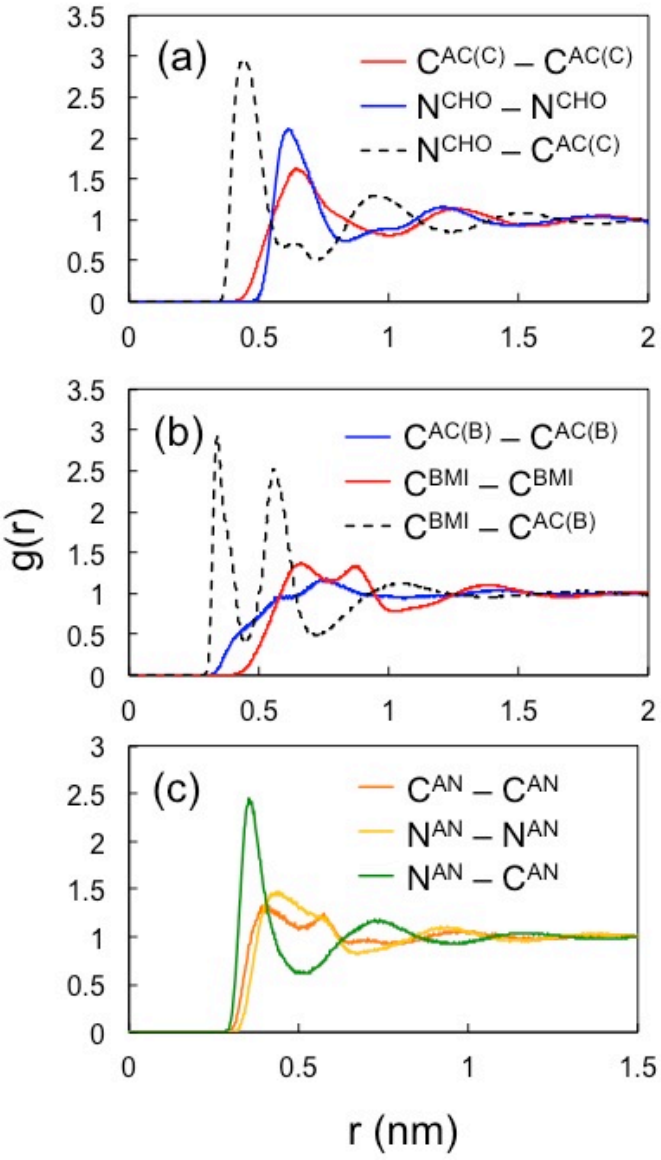

Figure 4.2: RDFs for (a) [Cho][Ac] at 400 K, (b) [BMI][Ac] at 400 K, and (c) acetonitrile at 300 K.

Table 4.2: Primary peak positions (r') and heights ($g(r')$)

RDF	T (K)	r'	$g(r')$
$N^{CHO} \cdots N^{CHO}$	350	0.60	2.2
$C^{AC(C)} \cdots C^{AC(C)}$	350	0.64	1.6
$C^{AC(C)} \cdots N^{CHO}$	350	0.43	3.0
$C^{BMI} \cdots C^{BMI}$	350	0.75	1.2
$C^{AC(B)} \cdots C^{AC(B)}$	350	0.66	1.4
$C^{AC(B)} \cdots C^{BMI}$	350	0.34	3.1
$N^{CHO} \cdots N^{CHO}$	400	0.61	2.1
$C^{AC(C)} \cdots C^{AC(C)}$	400	0.65	1.6
$C^{AC(C)} \cdots N^{CHO}$	400	0.44	3.0
$C^{BMI} \cdots C^{BMI}$	400	0.74	1.2
$C^{AC(B)} \cdots C^{AC(B)}$	400	0.65	1.4
$C^{AC(B)} \cdots C^{BMI}$	400	0.34	2.9
$N^{CHO} \cdots N^{CHO}$	600	0.63	1.9
$C^{AC(C)} \cdots C^{AC(C)}$	600	0.65	1.6
$C^{AC(C)} \cdots N^{CHO}$	600	0.46	2.9
$N^{AN} \cdots N^{AN}$	300	0.41	1.3
$C^{AN} \cdots C^{AN}$	300	0.44	1.5
$N^{AN} \cdots C^{AN}$	300	0.35	2.5

The SDF results indicate that cations – more precisely, their polar groups – are distributed preferentially around the C–O bonds of acetate. Though not shown here, the remaining solvation shell in the direction of the Ac methyl group is filled mainly by nonpolar groups of ions, *viz.*, butyl chain of BMI cations and methyl group of other Ac anions. It is worthwhile to note that the absence of long aliphatic chains in choline reduces its amphiphilic nature considerably, compared to, *e.g.*, BMI. As a result, the nonpolar hemisphere of the first solvation shell of acetate in [Cho][Ac] is filled predominantly by the methyl group of other Ac ions.[38] The double peaks in Figure 4.2(b) and the corresponding double shells in Figure 4.3(b) are due to interactions of C^{BMI} of BMI cations with Ac anions in different directions, as shown in Figure 4.4.

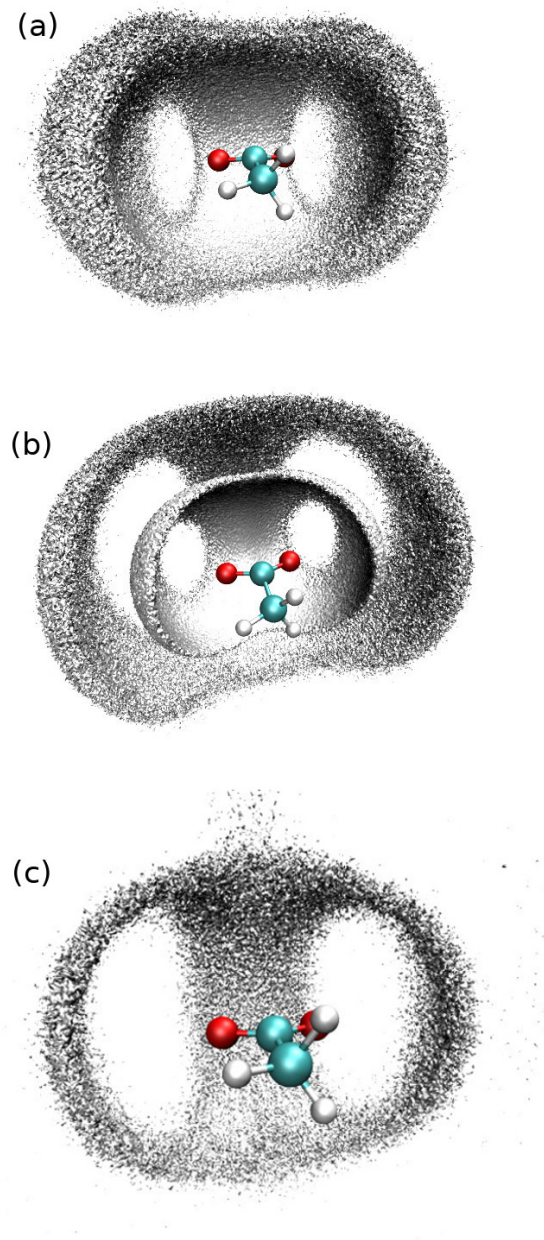

Figure 4.3: Isodensity plots of SDFs for (a) N^{BMI} and (b) C^{BMI} of [BMI], and (c) C^{CHO} of [Cho] around acetate at 400 K.

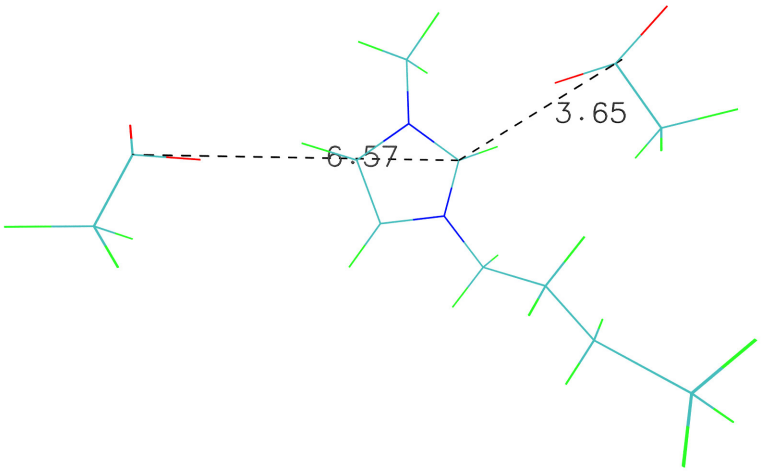

Figure 4.4: Ionic interactions of BMI and Ac ions.

4.3.3 Time Dependent Order Parameter

A time-dependent order parameter to characterize the system "glassiness" for species A can be defined as

$$Q_A^p(t) = \sum_{i,j \in A} \delta(|\vec{r}_i(0) - \vec{r}_j(t)|). \tag{4.2}$$

As discussed in Ref. 44, local vibrational dynamics, if present, can relax $Q^p(t)$ rapidly. Since our main focus is on correlations associated with systemic structural deformations as opposed to weakly-correlated localized vibrations, we remove the latter by employing a coarse-graining function[42–44]

$$w(r) = \begin{cases} 1 & \text{if } r < a \\ 0 & \text{if } r > a \end{cases} \tag{4.3}$$

in place of the delta function in Equation 4.2. This gives the species an effective volume of $V_0 = \frac{4}{3}\pi a^3$ and leads to

$$Q_A(t) = \sum_{i,j \in A} w(|\vec{r}_i(0) - \vec{r}_j(t)|). \tag{4.4}$$

Table 4.3: $\langle Q(t)/N\rangle$ fitting parameters for $\langle Q(t)/N\rangle = \sum_{i=1}^{4} A_i^Q \exp[-t/\tau_i^Q] + N_0$, where $N_0 = \langle Q(\infty)/N\rangle$. a is the parameter in $w(r)$ function.

Atom	T (K)	a (nm)	n_0	τ_1^Q (ns)	A_1^Q	τ_2^Q (ns)	A_2^Q	τ_3^Q (ns)	A_3^Q	τ_4^Q (ns)	A_4^Q
N^{CHO}	350	0.1320	0.03997	0.078	0.04	2.339	0.14	19.467	0.66	-	-
$C^{AC(C)}$	350	0.1424	0.05018	0.084	0.03	2.581	0.14	19.467	0.67	-	-
C^{BMI}	350	0.1567	0.04995	0.009	0.04	0.116	0.07	1.172	0.13	10.118	0.53
$C^{AC(B)}$	350	0.1424	0.03748	0.007	0.06	0.111	0.08	1.166	0.14	10.631	0.51
N^{CHO}	400	0.1320	0.03930	0.046	0.14	0.575	0.36	2.794	0.43	-	-
$C^{AC(C)}$	400	0.1424	0.04934	0.049	0.13	0.630	0.36	2.864	0.44	-	-
C^{BMI}	400	0.1567	0.04877	0.002	0.07	0.025	0.12	0.154	0.22	0.895	0.51
$C^{AC(B)}$	400	0.1424	0.03660	0.001	0.10	0.020	0.13	0.127	0.20	0.792	0.49
N^{CHO}	600	0.1320	0.03600	0.001	0.35	0.006	0.38	0.023	0.24	-	-
$C^{AC(C)}$	600	0.1424	0.04520	0.001	0.35	0.006	0.38	0.024	0.27	-	-
N^{AN}	300	0.1956	0.3569	0.0012	0.72	-	-	-	-	-	-
C^{AN}	300	0.1700	0.2343	0.0012	0.85	-	-	-	-	-	-

For IL systems, we employed $a = 0.4\,\sigma$. For acetonitrile, a values for its carbon and nitrogen atoms, C^{AN} and N^{AN}, were $0.5\,\sigma$ and $0.6\,\sigma$, respectively. Numerical values of a used for our analysis here can be found in Table 4.3. These a values were selected to optimize the susceptibility associated with $Q(t)$ (see below).[44] It is important to note that $Q(t)$ does not distinguish between particles of like species. This means that there is no contribution to the decay of $Q(t)$ when, for example, two particles of species A exchange positions. Because of this lack of distinction between particles of like species and the finite values of a, we find that $\langle Q(\infty)/N\rangle = N_0$, where $N_0 \equiv V_0 n$ and n is the number density of the species; n values are listed in Table 4.1 and N_0 values are listed in Table 4.3.

The MD results for $\langle Q(t)/N\rangle$ are displayed in Figure 4.5. The relaxation of $\langle Q(t)/N\rangle$ was found to be well fitted by the sum of multiple exponential decays, *i.e.*

$$\left\langle \frac{Q(t)}{N} \right\rangle = \sum_{i=1}^{4} A_i^Q \exp[-t/\tau_i^Q] + N_0. \tag{4.5}$$

Values for a, N_0, τ_i^Q, and A_i^Q can be found in Table 4.3. [Cho][Ac] and [BMI][Ac]

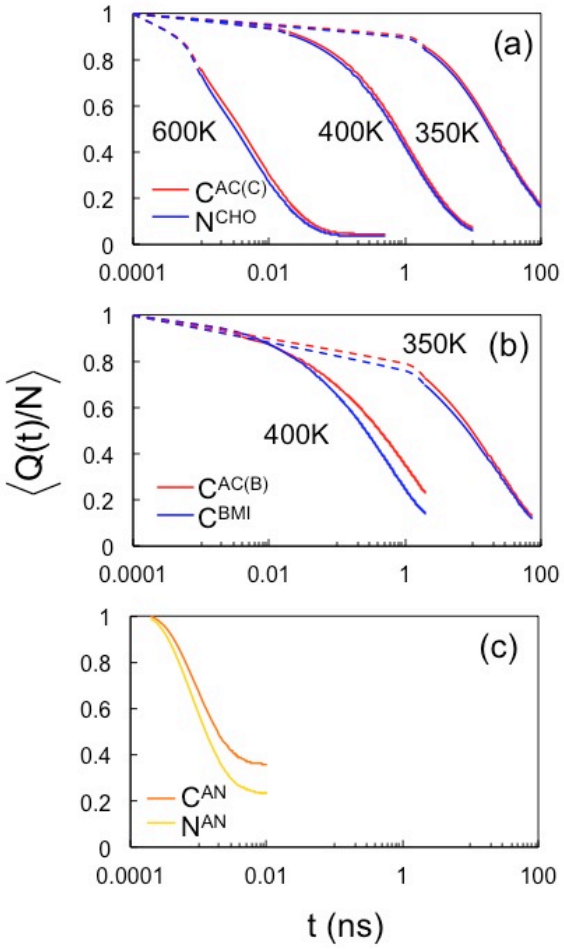

Figure 4.5: Plots of $\langle Q(t)/N \rangle$ for (a) [Cho][Ac], (b) [BMI][Ac], and (c) acetonitrile. For each IL system, cation $\cdots$ cation are blue and anion $\cdots$ anion are red; for acetonitrile $N^{AN} \cdots N^{AN}$ is yellow and $C^{AN} \cdots C^{AN}$ is orange. The dashed line is just a guide for eyes.

were fitted with three and four exponential functions, respectively. By contrast, a single exponential function well describes $\langle Q(t)/N \rangle$ of acetonitrile, indicating that underlying dynamics are Gaussian. As is expected, $\langle Q(t)/N \rangle$ decays faster at higher temperatures; all values of τ_i^Q's are smaller and the contribution of the fastest decay component, *viz.*, A_1^Q, to the overall relaxation increases. At 350 K and 400 K, $\langle Q(t)/N \rangle$ for [Cho][Ac] – the more viscous of the two ILs – decays more slowly than $\langle Q(t)/N \rangle$ for [BMI][Ac]; at all simulated temperatures, both ILs decay much more slowly than acetonitrile.

4.3.4 Four Point Correlation Functions

To understand the time evolution of the dynamic correlation between species A and B, we analyzed the four-point overlap correlation function $g_4^{ol}(r,t)$ between the two species

$$g_4^{ol}(\vec{r},t) = \frac{V}{N_A N_B}\left\langle \sum_{ij\,\in A}\sum_{kl\,\in B} \delta\left(\vec{r}-\vec{r}_k(0)+\vec{r}_i(0)\right) \times w\left(|\vec{r}_i(0)-\vec{r}_j(t)|\right) w\left(|\vec{r}_k(0)-\vec{r}_l(t)|\right)\right\rangle . \quad (4.6)$$

For simplicity, we consider a radially averaged correlation function, $g_4^{ol}(r,t)$, where $r = |\vec{r}|$. We note that $g_4^{ol}(r,t)$ is a direct extension of the full van Hove function; it describes time evolution of correlation of density fluctuations occurring simultaneously at two different positions, located a distance of r apart. As such, it gauges the four-particle conditional probability; *viz.*, given a particle of species A at position 1 and particle of species B at position 2 at the initial time $t = 0$, it measures (up to a constant) the probability that the same or another particle of A and the same or another particle of B will be found at positions very close to the original locations 1 and 2, respectively, at a later time. Like the order parameter described above, $g_4^{ol}(r,t)$ does not distinguish between particles of the same species. This means that at time $t = 0$, $g_4^{ol}(r,0)$ becomes the RDF, *i.e.*, $g_4^{ol}(r,0) = g(r)$. We also note that $g_4^{ol}(\infty,t) = \langle Q_A(t)/N_A\rangle \langle Q_B(t)/N_B\rangle$ because particles are of finite size and become spatially uncorrelated at large r. In other words, $g_4^{ol}(r',t)$ does not decay to zero due to the finite value of a.

Analogous to the fitting for $\langle Q(t)/N\rangle$ in Equation 4.5, we were able to fit $g_4^{ol}(r,t)$ for ILs accurately with three exponential functions as

$$g_4^{ol}(r,t) = \sum_{i=1}^{3} A_i^{ol}(r)\exp[-t/\tau_i^{ol}(r)] + b(r)\ . \quad (4.7)$$

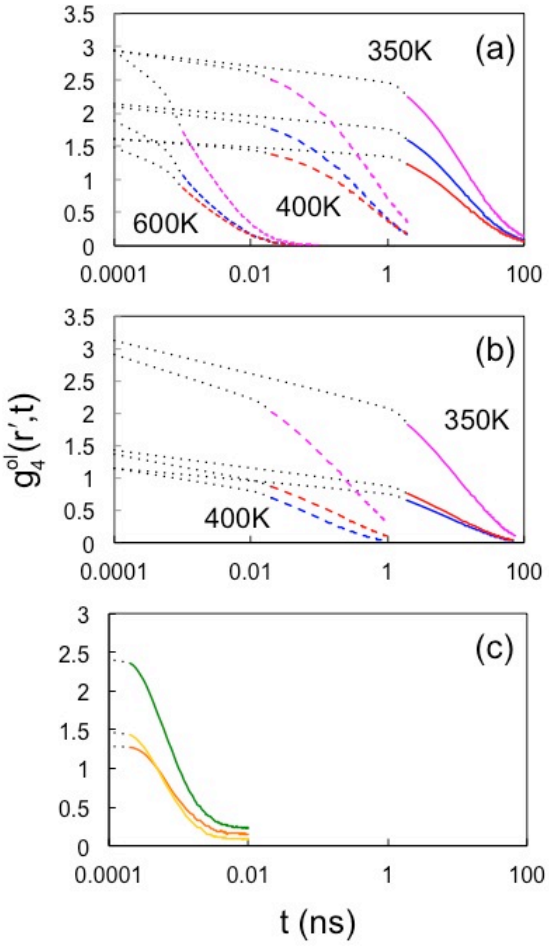

Figure 4.6: Plots of $g_4^{ol}(r', t)$ for (a) [Cho][Ac], (b) [BMI][Ac], and (c) acetonitrile . For each IL system, cation $\cdots$ cation are blue, anion $\cdots$ anion are red, and cation $\cdots$ anion are purple; for acetonitrile $N^{AN} \cdots N^{AN}$ is orange, $C^{AN} \cdots C^{AN}$ is yellow, and $N^{AN} \cdots C^{AN}$ is green. The dotted line is just a guide for eyes.

Table 4.4: $g_4^{ol}(r,t)$ fitting at $r = r'$

Pair types	T (K)	$b(r)$	$\tau_1^{ol}(r)$ (ns)	$A_1^{ol}(r)$	$\tau_2^{ol}(r)$ (ns)	$A_2^{ol}(r)$	$\tau_3^{ol}(r)$ (ns)	$A_3^{ol}(r)$
$N^{CHO} \cdots N^{CHO}$	350	0.090	0.13	0.17	2.44	0.49	14.00	1.34
$C^{AC(C)} \cdots C^{AC(C)}$	350	0.063	0.10	0.11	2.44	0.42	14.59	1.03
$N^{CHO} \cdots C^{AC(C)}$	350	0.227	0.11	0.19	2.21	0.63	13.70	1.92
$C^{BMI} \cdots C^{BMI}$	350	0.092	0.10	0.26	1.12	0.26	7.95	0.58
$C^{AC(B)} \cdots C^{AC(B)}$	350	0.094	0.08	0.37	1.07	0.32	8.84	0.66
$C^{BMI} \cdots C^{AC(B)}$	350	0.380	0.09	0.69	0.98	0.57	8.20	1.58
$N^{CHO} \cdots N^{CHO}$	400	0.013	0.06	0.56	0.44	0.91	1.73	0.61
$C^{AC(C)} \cdots C^{AC(C)}$	400	0.010	0.06	0.43	0.54	0.78	1.97	0.39
$N^{CHO} \cdots C^{AC(C)}$	400	0.021	0.07	0.81	0.52	1.27	1.90	0.84
$C^{BMI} \cdots C^{BMI}$	400	0.020	0.01	0.40	0.11	0.37	0.57	0.42
$C^{AC(B)} \cdots C^{AC(B)}$	400	0.063	0.01	0.46	0.06	0.35	0.40	0.57
$C^{BMI} \cdots C^{AC(B)}$	400	0.181	0.01	0.81	0.07	0.72	0.45	1.33
$N^{CHO} \cdots N^{CHO}$	600	0.0033	0.95×10^{-3}	0.99	4.30×10^{-3}	0.71	15.93×10^{-3}	0.19
$C^{AC(C)} \cdots C^{AC(C)}$	600	0.0041	0.08×10^{-3}	0.64	4.15×10^{-3}	0.65	16.18×10^{-3}	0.18
$N^{CHO} \cdots C^{AC(C)}$	600	0.0088	0.80×10^{-3}	1.35	4.34×10^{-3}	1.20	16.24×10^{-3}	0.36
$N^{AN} \cdots N^{AN}$	300	0.15	1.05×10^{-3}	1.13	-	-	-	-
$C^{AN} \cdots C^{AN}$	300	0.07	0.90×10^{-3}	1.34	-	-	-	-
$N^{AN} \cdots C^{AN}$	300	0.22	0.99×10^{-3}	2.22	-	-	-	-

We found that $g_4^{ol}(r,t)$ for acetonitrile is well described by a single exponential function. As mentioned above, $b(r)$ in Equation 4.7 becomes $\langle Q_A(\infty)/N_A \rangle \langle Q_B(\infty)/N_B \rangle$ ($= N_{A,0}N_{B,0}$) at large r. Values for τ_i^{ol}, A_i^{ol}, and b for $r = r'$, *i.e.*, positions of primary RDF peaks, are presented in Table 4.4 (see Table 4.2 for values of r' and $g(r')$). The corresponding relaxation behaviors of $g_4^{ol}(r',t)$ for the systems considered here are compared in Figure 4.6. At given temperature, [BMI][Ac] shows a faster decay of $g_4^{ol}(r,t)$ than [Cho][Ac] just like the $\langle Q(t)/N \rangle$ case. The $g_4^{ol}(r,t)$ relaxation in acetonitrile at 300 K is faster than that in [BMI][Ac] and [Cho][Ac] at 350 K by $\sim$4 orders of magnitude.

For further insight, we have examined the r-dependence of $\tau_i^{ol}(r)$ and their normalized contributions $A_i^{ol}(r)/\sum_{i=1}^{3} A_i^{ol}(r)$. The results for [Cho][Ac] at 400 K are shown in Figure 4.7. The different $\tau_i^{ol}(r)$ values correspond to different relaxation time-domains of $g_4^{ol}(r,t)$. The fastest decay time, $\tau_1^{ol}(r)$, likely due to initial mo-

tions of ions within their cages, exhibits essentially no dependence on r (Figure 4.7a). We think that such motions are fairly localized and thus rapid density fluctuations arising from them are not affected by the motions of other ions. The slower decay times, especially $\tau_3^{ol}(r)$, on the other hand, show considerable r-dependence for $r \lesssim 1.3$ nm. This means that slow density fluctuations of ions are likely influenced by and therefore correlated with the density fluctuations of other ions located within a distance of ~ 1.3 nm. The results in Figure 4.7b show that all three decay components make a significant contribution to the overall relaxation of $g_4^{ol}(r,t)$. There are several noteworthy features. First, the normalized amplitudes of the two slow components, $A_{2,3}^{ol}(r)/\sum_{i=1}^{3} A_i^{ol}(r)$, are strongly correlated while they show near perfect anticorrleation with the normalized amplitude of the fastest component. Second, the r-behavior of the amplitudes of the slow components is very similar to the corresponding RDF (*cf.* Figure 4.2). We note that [BMI][Ac] shows behaviors similar to [Cho][Ac] and thus is not shown here.

The susceptibility $\chi_4(t)$, which describes the fluctuations of the order parameter of the system, is defined as

$$\chi_4(t) = \frac{\beta V}{N} \left[\langle Q(t)^2 \rangle - \langle Q(t) \rangle^2 \right], \tag{4.8}$$

with $\beta = 1/k_B T$. $\chi_4(t)$ measures cooperative motions of ions at two different locations, averaged over the system. Figure 4.8 displays $\chi_4(t)$ for $\mathrm{C}^{\mathrm{AC(C)}} \cdots \mathrm{C}^{\mathrm{AC(C)}}$ at 400 K determined with different values of a. As mentioned above where a was first introduced, the a value with the greatest susceptibility is used for calculations throughout this work.[44]

Figure 4.9 shows the MD results for the susceptibility for each system at the selected a value (Table 4.3). As is expected from the temporal behaviors of both the order parameters and the four-point density time correlation functions, we find

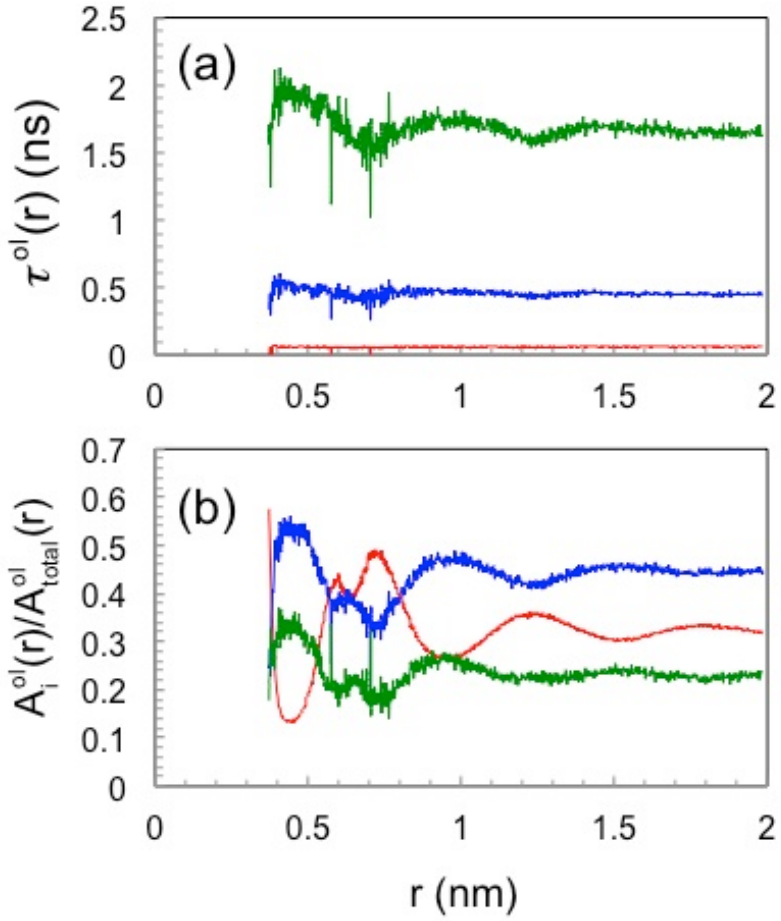

Figure 4.7: Plots of τ_i^{ol} for $\mathrm{C}^{AC(C)} \cdots \mathrm{N}^{CHO}$ at 400 K are shown in (a), and plots of cofactors, $A_i^{ol}(r)$, normalized to the sum of cofactors ($A_{total}^{ol}(r) = \sum_{i=1}^{3} A_i^{ol}(r)$) are shown in (b), where $i = 1$ is shown in red, $i = 2$ is shown in blue, and $i = 3$ is shown in green.

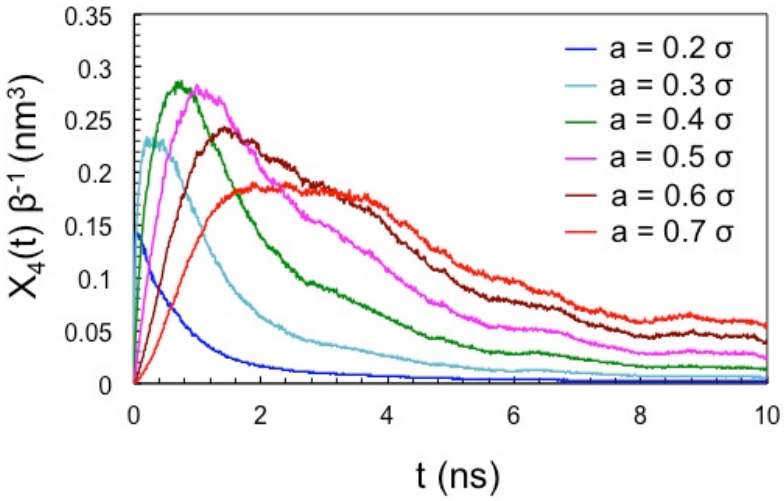

Figure 4.8: Plots of $\chi_4(t)$ for $C^{AC(C)} \cdots C^{AC(C)}$ in [Cho][Ac] at 400 K with different values of a.

$\chi_4(t)$ peaks at longer times for lower temperatures. Furthermore, $\chi_4(t)$ for more viscous [Cho][Ac] is slower than that for [BMI][Cl]. We ascribe the molecular origin of this difference to the formation of hydrogen bond in the former.[38] Interestingly, the susceptibility calculated between like species is greater than the susceptibility calculated between unlike species.

In many prior studies,[25,29,30,38,50,51,64,65] the deviation of the IL transport behavior from Gaussian dynamics is measured by

$$\alpha_2(t) = \frac{3}{5}\frac{\langle \Delta r^4(t) \rangle}{\langle \Delta r^2(t) \rangle^2} - 1 \ , \tag{4.9}$$

where $\Delta r(t)$ is the displacement of ions at time t from their initial positions. Comparison of the results in Figure 4.10 with those in Figure 4.9 reveals that temporal behaviors of $\alpha_2(t)$ and $\chi_4(t)$, including their peak positions, are very similar for all temperatures and systems we considered. This indicates that the non-Gaussian behavior of single particle dynamics is directly related to time-dependent correlated

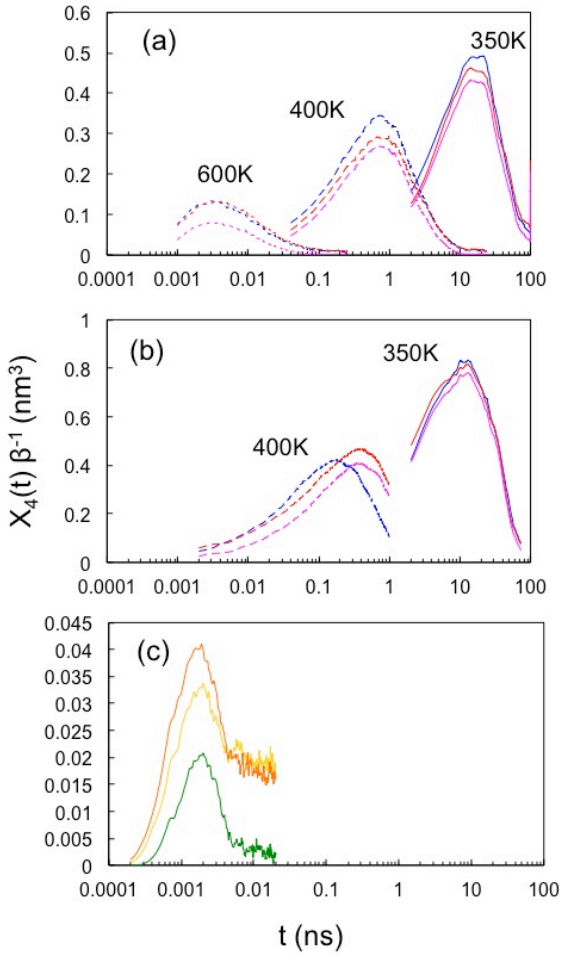

Figure 4.9: Plots of $\chi_4(t)$ for (a) [Cho][Ac], (b) [BMI][Ac], and (c) acetonitrile. For each IL system, cation $\cdots$ cation are blue, anion $\cdots$ anion are red, and cation $\cdots$ anion are purple; for acetonitrile $N^{AN} \cdots N^{AN}$ is orange, $C^{AN} \cdots C^{AN}$ is yellow, and $N^{AN} \cdots C^{AN}$ is green.

motions of two particles, *viz.*, cooperative dynamics.

4.3.5 Dynamic Correlation Length

Finally, we proceed to the dynamic length scale associated with cooperative motions in ILs. We employ the apporach widely used in the analysis of glass systems,[44–48,50]

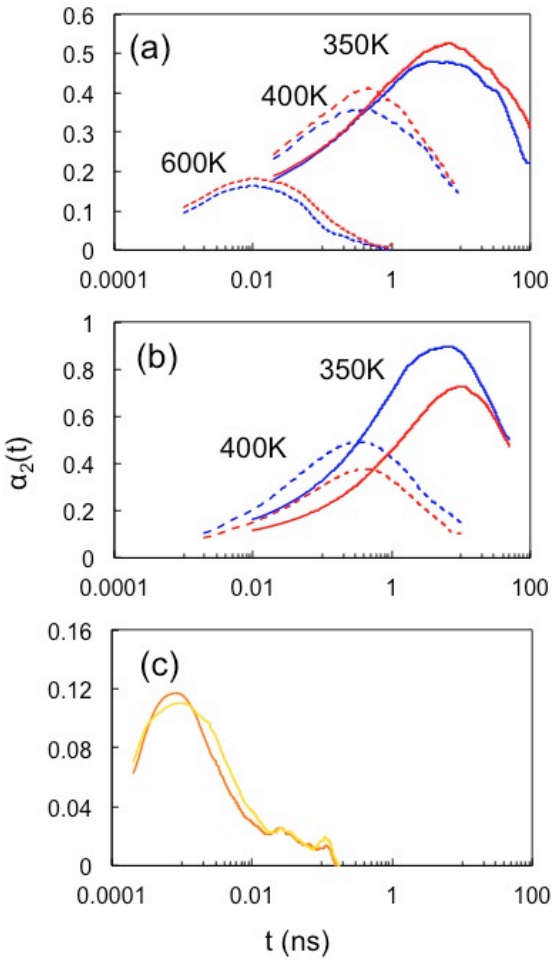

Figure 4.10: Plots of the non-Gaussian factor, $\alpha_2(t)$ for (a) [Cho][Ac], (b) [BMI][Ac], and (c) acetonitrile; cations are shown in blue, anions are shown in red, N^{AN} is in orange, and C^{AN} is in yellow.

viz., small wave vector expansion of the four-point structure factor

$$S_4^{ol}(\vec{q},t) = \frac{1}{N_A}\left\langle \sum_{i,j\in A} \exp\,[i\vec{q}\cdot\vec{r}_i(0)]w(|\vec{r}_i(0)-\vec{r}_j(t)|) \times \sum_{k,l\in A} \exp\,[-i\vec{q}\cdot\vec{r}_k(0)]w(|\vec{r}_k(0)-\vec{r}_l(t)|)\right\rangle. \tag{4.10}$$

The inclusion up to the q^2 terms in the expansion à la Ornstein-Zernike (OZ) theory yields[44,45]

$$S_4^{ol}(q,t) = \frac{S_4^{ol}(0,t)}{1+(q\xi_4(t))^{\alpha}} \tag{4.11}$$

with $\alpha = 2$. The corresponding r-space behavior is given by

$$g_4^{ol}(r,t) \propto \frac{S_4^{ol}(0,t)}{r\xi_4(t)^2} \exp[-r/\xi_4(t)] \ . \tag{4.12}$$

While a more general expression with $\alpha \neq 2$ is often used in the analysis of glass systems,[46–48,50] we employ here the original OZ form,[44,45] *i.e.*, $\alpha = 2$ in Equation 4.11, mainly due to the limited number of data points available for the numerical analysis. This limitation arises from the small system size we used to speed up the simulations because long trajectories are needed for proper sampling of highly viscous and thus slowly-relaxing ILs. We computed the radially averaged structure factor, $S_4^{ol}(q,t)$ ($q = |\vec{q}|$), by including in the calculations only $\vec{q}$ vectors that satisfy the periodic boundary conditions of the simulation system and fitted the resulting $S_4^{ol}(q,t)$ with Equation 4.11 ($\alpha = 2$) at the lowest five q values using the Newton method with $S_4^{ol}(0,t)$ and $\xi_4(t)$ treated as fitting parameters.

The results for $\xi_4(t)$ for like ions (cation$\cdots$cation and anion$\cdots$anion) are shown in Figure 4.11. As is expected, increasing temperature leads to shorter correlation lengths, *i.e.*, lower peak heights of $\xi_4(t)$. This means that the spatial range of cooperative dynamics becomes shorter as the temperature rises. Another important feature is that the spatial range of cooperative dynamics varies with time. This can be understood as follows: A dynamic event, occurring at, say, position 1 cannot be influenced by another dynamic event at a different location, position 2, if the two events occur at the same time because the effect of a dynamic event cannot propagate instantaneously. However, a dynamic event occurring at a later time at position 1 can be influenced by a dynamic event at an earlier time at position 2. We expect that with time, the propagation and strength of the effect of a dynamic event grows and diminishes, respectively. As a result, the corresponding spatial range of the influence of a dynamic event will exhibit a non-monotonic behavior in t, reaching a maximum

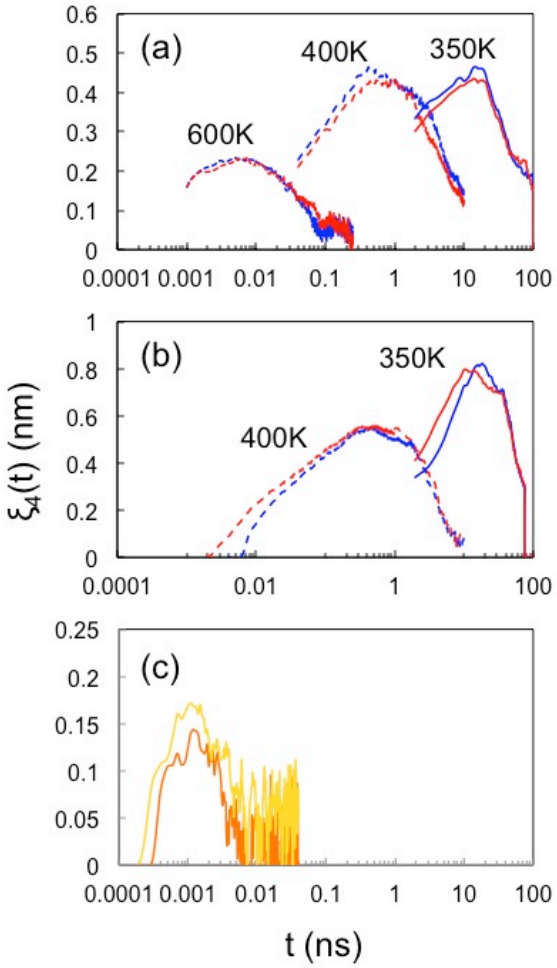

Figure 4.11: Like-species plots of $\xi(t)$ *vs.* time for (a) [Cho][Ac] and (b) [BMI][Ac] and (c) acetonitrile. Cation $\cdots$ cation curves are in blue and anion $\cdots$ anion curves are in red; $N^{AN} \cdots N^{AN}$ is in orange and $C^{AN} \cdots C^{AN}$ is in yellow.

at some point, followed by a decrease. $\chi_4(t)$ measures this time-dependence via Equation 4.12. Comparison with Figure 4.9 shows that the peak positions of $\xi_4(t)$ are close to those of $\chi_4(t)$.

The correlation length scale can be compared with the sizes of ions shown in RDFs, Figure 4.2. For [Cho][Ac], the maximum $\xi_4(t)$ at 600 K is smaller than the ionic radii. As the temperature decreases, the correlation length approaches and goes slightly above the ionic radii for both [Cho][Ac] and [BMI][Ac]. The length scale of acetonitrile is much less than its molecular size, indicating no correlated motions. It also shows that the correlation length depends on the dynamics across the system rather than the size of the species.

It is worthwhile to note that the temperatures of our simulations are well above the reported glass transtion temperatures of both systems. We expect that if simulations were performed at lower temperatures, the length scale would further increase, which implies that both systems would show stronger glassy behavior at room temperature.

4.4 Conclusions

Spatially correlated dynamics in ILs is brought about, in part, by distinct spatial clustering of "mobile" and "immobile" ions. Studies of glass systems with similar behavior implement a four-point time-correlation function to simultaneously gauge the length-scale of correlated regions and the time associated with the correlation.

In this paper we studied the time-dependent four-point density correlation function ($g_4^{ol}(r,t)$), its related susceptibility ($\chi_4(t)$), and the dynamic length scale of correlation ($\xi_4(t)$) for the ILs [Cho][Ac] and [BMI][Ac]. We found that $g_4^{ol}(r,t)$ exhibits r-dependent relaxation, revealing the influence of spatial correlation on collective motions of ions. $\xi_4(t)$ determined by fitting the four-point structure factor $S_4^{ol}(q,t)$ in the low q region shows that the spatial range of collective motions initially increases

with time but decreases after reaching a maximum. Compared with the traditional solvent, acetonitrile, correlation extends to greater distances in the studied ILs and is retained for significantly longer times.

Our results indicate that four-point time correlation functions can shed new light on IL dynamics, not accessible via two-point correlation functions and thus provide a useful theoretical tool to study IL dynamics, especially their cooperative aspect. Therefore it would be worthwhile in the future to study structure-dynamics relationships in ILs, such as the influence of structural heterogeneity on collective dynamics, using the four-point time correlation functions and their variants.

[1] Plechkova, N. V.; Seddon, K. R. Applications of ionic liquids in the chemical industry. *Chem. Soc. Rev.* **2008**, *37*, 123–150.

[2] Watanabe, M.; Thomas, M. L.; Zhang, S.; Ueno, K.; Yasuda, T.; Dokko, K. Application of Ionic Liquids to Energy Storage and Conversion Materials and Devices. *Chem. Rev.* **2017**, *117*, 7190–7239.

[3] Egorova, K. S.; Gordeev, E. G.; Ananikov, V. P. Biological Activity of Ionic Liquids and Their Application in Pharmaceutics and Medicine. *Chem. Rev.* **2017**, *117*, 7132–7189.

[4] Amiril, S.; Rahim, E.; Syahrullail, S. A review on ionic liquids as sustainable lubricants in manufacturing and engineering: Recent research, performance, and applications. *J. Cleaner Prod.* **2017 in press**,

[5] Agbor, V. B.; Cicek, N.; Sparling, R.; Berlin, A.; Levin, D. B. Biomass pretreatment: Fundamentals toward application. *Biotechnol. Adv.* **2011**, *29*, 675–685.

[6] Triolo, A.; Russina, O.; Arrighi, V.; Juranyi, F.; Janssen, S.; Gordon, C. M. Quasielastic neutron scattering characterization of the relaxation processes in a room temperature ionic liquid. *The Journal of Chemical Physics* **2003**, *119*, 8549–8557.

[7] Ingram, J. A.; Moog, R. S.; Ito, N.; Biswas, R.; Maroncelli, M. Solute Rotation and Solvation Dynamics in a Room-Temperature Ionic Liquid. *The Journal of Physical Chemistry B* **2003**, *107*, 5926–5932.

[8] Chakrabarty, D.; Hazra, P.; Chakraborty, A.; Seth, D.; Sarkar, N. Dynamics of solvent relaxation in room temperature ionic liquids. *Chemical Physics Letters* **2003**, *381*, 697 – 704.

[9] Chowdhury, P. K.; Halder, M.; Sanders, L.; Calhoun, T.; Anderson, J. L.; Armstrong, D. W.; Song, X.; Petrich, J. W. Dynamic Solvation in Room-Temperature Ionic Liquids. *The Journal of Physical Chemistry B* **2004**, *108*, 10245–10255.

[10] Mandal, P. K.; Sarkar, M.; Samanta, A. Excitation-Wavelength-Dependent Fluorescence Behavior of Some Dipolar Molecules in Room-Temperature Ionic Liquids. *The Journal of Physical Chemistry A* **2004**, *108*, 9048–9053.

[11] Shirota, H.; Funston, A. M.; Wishart, J. F.; Castner Jr., E. W. Ultrafast dynamics of pyrrolidinium cation ionic liquids. *The Journal of Chemical Physics* **2005**, *122*, 184512.

[12] Samanta, A. Dynamic Stokes Shift and Excitation Wavelength Dependent Fluorescence of Dipolar Molecules in Room Temperature Ionic Liquids. *The Journal of Physical Chemistry B* **2006**, *110*, 13704–13716.

[13] Arzhantsev, S.; Jin, H.; Ito, N.; Maroncelli, M. Observing the complete solvation response of DCS in imidazolium ionic liquids, from the femtosecond to nanosecond regimes. *Chemical Physics Letters* **2006**, *417*, 524 – 529.

[14] Lang, B.; Angulo, G.; Vauthey, E. Ultrafast Solvation Dynamics of Coumarin 153 in Imidazolium-Based Ionic Liquids. *The Journal of Physical Chemistry A* **2006**, *110*, 7028–7034, PMID: 16737250.

[15] Funston, A. M.; Fadeeva, T. A.; Wishart, J. F.; Castner, E. W. Fluorescence Probing of Temperature-Dependent Dynamics and Friction in Ionic Liquid Local Environments. *The Journal of Physical Chemistry B* **2007**, *111*, 4963–4977, PMID: 17439268.

[16] Arzhantsev, S.; Jin, H.; Baker, G. A.; Maroncelli, M. Measurements of the Complete Solvation Response in Ionic Liquids. *The Journal of Physical Chemistry B* **2007**, *111*, 4978–4989.

[17] Jin, H.; Li, X.; Maroncelli, M. Heterogeneous Solute Dynamics in Room Temperature Ionic Liquids. *The Journal of Physical Chemistry B* **2007**, *111*, 13473–13478.

[18] Jin, H.; Li, X.; Maroncelli, M. Heterogeneous Solute Dynamics in Room-Temperature Ionic Liquids. *The Journal of Physical Chemistry B* **2010**, *114*, 11370–11370.

[19] Yamamuro, O.; Yamada, T.; Kofu, M.; Nakakoshi, M.; Nagao, M. Hierarchical structure and dynamics of an ionic liquid 1-octyl-3-methylimidazolium chloride. *The Journal of Chemical Physics* **2011**, *135*, 054508.

[20] Kofu, M.; Nagao, M.; Ueki, T.; Kitazawa, Y.; Nakamura, Y.; Sawamura, S.; Watanabe, M.; Yamamuro, O. Heterogeneous Slow Dynamics of Imidazolium-Based Ionic Liquids Studied by Neutron Spin Echo. *The Journal of Physical Chemistry B* **2013**, *117*, 2773–2781.

[21] Guo, J.; Baker, G. A.; Hillesheim, P. C.; Dai, S.; Shaw, R. W.; Mahurin, S. M. Fluorescence correlation spectroscopy evidence for structural heterogeneity in ionic liquids. *Phys. Chem. Chem. Phys.* **2011**, *13*, 12395–12398.

[22] Patra, S.; Samanta, A. Microheterogeneity of Some Imidazolium Ionic Liquids As Revealed by Fluorescence Correlation Spectroscopy and Lifetime Studies. *The Journal of Physical Chemistry B* **2012**, *116*, 12275–12283.

[23] Wu, E. C.; Kim, H. J.; Peteanu, L. A. Spectroscopic and MD Study of Dynamic and Structural Heterogeneities in Ionic Liquids. *The Journal of Physical Chemistry B* **2017**, *121*, 1100–1107.

[24] Shim, Y.; Duan, J.; Choi, M. Y.; Kim, H. J. Solvation in molecular ionic liquids. *The Journal of Chemical Physics* **2003**, *119*, 6411–6414.

[25] Del Pópolo, M. G.; Voth, G. A. On the Structure and Dynamics of Ionic Liquids. *J. Phys. Chem.B* **2004**, *108*, 1744–1752.

[26] Shim, Y.; Choi, M. Y.; Kim, H. J. A molecular dynamics computer simulation study of room-temperature ionic liquids. II. Equilibrium and nonequilibrium solvation dynamics. *The Journal of Chemical Physics* **2005**, *122*, 044511.

[27] Shim, Y.; Jeong, D.; Choi, M. Y.; Kim, H. J. Rotational dynamics of a diatomic solute in the room-temperature ionic liquid 1-ethyl-3-methylimidazolium hexafluorophosphate. *The Journal of Chemical Physics* **2006**, *125*, 061102.

[28] Kobrak, M. N. Characterization of the solvation dynamics of an ionic liquid via molecular dynamics simulation. *The Journal of Chemical Physics* **2006**, *125*, 064502.

[29] Hu, Z.; Margulis, C. J. Heterogeneity in a room-temperature ionic liquid: persistent local environments and the red-edge effect. *Proc. Natl. Acad. Sci. U.S.A.* **2006**, *103*, 831–836.

[30] Cadena, C.; Zhao, Q.; Snurr, R. Q.; Maginn, E. J. Molecular modeling and experimental studies of the thermodynamic and transport properties of pyridinium-based ionic liquids. *J. Phys. Chem. B* **2006**, *110*, 2821–2832.

[31] Hu, Z.; Margulis, C. J. Room-Temperature Ionic Liquids: Slow Dynamics, Viscosity, and the Red Edge Effect. *Accounts of Chemical Research* **2007**, *40*, 1097–1105.

[32] Shim, Y.; Kim, H. J. Dielectric Relaxation, Ion Conductivity, Solvent Rotation, and Solvation Dynamics in a Room-Temperature Ionic Liquid. *The Journal of Physical Chemistry B* **2008**, *112*, 11028–11038.

[33] Jeong, D.; Choi, M. Y.; Kim, H. J.; Jung, Y. Fragility, Stokes-Einstein violation, and correlated local excitations in a coarse-grained model of an ionic liquid. *Phys. Chem. Chem. Phys.* **2010**, *12*, 2001–2010.

[34] Terranova, Z. L.; Corcelli, S. A. On the Mechanism of Solvation Dynamics in Imidazolium-Based Ionic Liquids. *The Journal of Physical Chemistry B* **2013**, *117*, 15659–15666.

[35] Araque, J. C.; Yadav, S. K.; Shadeck, M.; Maroncelli, M.; Margulis, C. J. How Is Diffusion of Neutral and Charged Tracers Related to the Structure and Dynamics of a Room-Temperature Ionic Liquid? Large Deviations from Stokes–Einstein Behavior Explained. *The Journal of Physical Chemistry B* **2015**, *119*, 7015–7029.

[36] Lesch, V.; Heuer, A.; Holm, C.; Smiatek, J. Solvent effects of 1-ethyl-3-methylimidazolium acetate: solvation and dynamic behavior of polar and apolar solutes. *Phys. Chem. Chem. Phys.* **2015**, *17*, 8480–8490.

[37] Kim, D.; Park, S.-W.; Shim, Y.; Kim, H. J.; Jung, Y. Excitation-energy dependence of solvation dynamics in room-temperature ionic liquids. *The Journal of Chemical Physics* **2016**, *145*, 044502.

[38] Willcox, J. A. L.; Kim, H.; Kim, H. J. A molecular dynamics study of the ionic liquid, choline acetate. *Phys. Chem. Chem. Phys.* **2016**, *18*, 14850–14858.

[39] Verma, S. D.; Corcelli, S. A.; Berg, M. A. Rate and Amplitude Heterogeneity in the Solvation Response of an Ionic Liquid. *The Journal of Physical Chemistry Letters* **2016**, *7*, 504–508.

[40] Daly, R. P.; Araque, J. C.; Margulis, C. J. Communication: Stiff and soft nanoenvironments and the "Octopus Effect" are the crux of ionic liquid structural and dynamical heterogeneity. *The Journal of Chemical Physics* **2017**, *147*, 061102.

[41] Dasgupta, C.; Indrani, A. V.; Ramaswamy, S.; Phani, M. K. Is There a Growing Correlation Length near the Glass Transition? *EPL (Europhysics Letters)* **1991**, *15*, 307.

[42] Glotzer, S. C.; Novikov, V. N.; Schrøder, T. B. Time-dependent, four-point density correlation function description of dynamical heterogeneity and decoupling in supercooled liquids. *The Journal of Chemical Physics* **2000**, *112*, 509–512.

[43] Lačević, N.; Starr, F. W.; Schrøder, T. B.; Novikov, V. N.; Glotzer, S. C. Growing correlation length on cooling below the onset of caging in a simulated glass-forming liquid. *Phys. Rev. E* **2002**, *66*, 030101.

[44] Lačević, N.; Starr, F. W.; Schrøder, T. B.; Glotzer, S. C. Spatially heterogeneous dynamics investigated via a time-dependent four-point density correlation function. *J. Chem. Phys.* **2003**, *119*, 7372–7387.

[45] Berthier, L. Time and length scales in supercooled liquids. *Phys. Rev. E* **2004**, *69*, 020201.

[46] Toninelli, C.; Wyart, M.; Berthier, L.; Biroli, G.; Bouchaud, J.-P. Dynamical susceptibility of glass formers: Contrasting the predictions of theoretical scenarios. *Phys. Rev. E* **2005**, *71*, 041505.

[47] Berthier, L.; Biroli, G.; Bouchaud, J.-P.; Kob, W.; Miyazaki, K.; Reichman, D. R. Spontaneous and induced dynamic fluctuations in glass formers. I. General results and dependence on ensemble and dynamics. *The Journal of Chemical Physics* **2007**, *126*, 184503.

[48] Berthier, L.; Biroli, G.; Bouchaud, J.-P.; Kob, W.; Miyazaki, K.; Reichman, D. R. Spontaneous and induced dynamic correlations in glass formers. II. Model calculations and comparison to numerical simulations. *The Journal of Chemical Physics* **2007**, *126*, 184504.

[49] Karmakar, S.; Dasgupta, C.; Sastry, S. Growing length and time scales in glass-forming liquids. *Proceedings of the National Academy of Sciences* **2009**, *106*, 3675–3679.

[50] Kim, K.; Saito, S. Multiple length and time scales of dynamic heterogeneities in model glass-forming liquids: A systematic analysis of multi-point and multi-time correlations. *The Journal of Chemical Physics* **2013**, *138*, 12A506.

[51] Pal, T.; Biswas, R. Slow solvation in ionic liquids: Connections to non-Gaussian moves and multi-point correlations. *The Journal of Chemical Physics* **2014**, *141*, 104501.

[52] Lindahl, E.; Hess, B.; van der Spoel, D. GROMACS 3.0: a package for molecular simulation and trajectory analysis. *Mol. Model. Annu.* **2001**, *7*, 306–317.

[53] Berendsen, H.; van der Spoel, D.; van Drunen, R. GROMACS: A message-passing parallel molecular dynamics implementation. *Comput. Phys. Commun.* **1995**, *91*, 43–56.

[54] Van Der Spoel, D.; Lindahl, E.; Hess, B.; Groenhof, G.; Mark, A. E.; Berendsen, H. J. C. GROMACS: fast, flexible, and free. *J. Comput. Chem.* **2005**, *26*, 1701–1718.

[55] Hess, B.; Kutzner, C.; van der Spoel, D.; Lindahl, E. GROMACS 4: Algorithms for Highly Efficient, Load-Balanced, and Scalable Molecular Simulation. *J. Chem. Theory Comput.* **2008**, *4*, 435–447.

[56] Bogolitsyn, K. G.; Skrebets, T. E.; Makhova, T. A. Physicochemical properties of 1-butyl-3-methylimidazolium acetate. *Russian Journal of General Chemistry* **2009**, *79*, 125–128.

[57] Haynes, W. M., Ed. *CRC Handbook of Chemistry and Physics*, 95th ed.; CRC Press, 2014.

[58] https://www.paramchem.org.

[59] Vanommeslaeghe, K.; Hatcher, E.; Acharya, C.; Kundu, S.; Zhong, S.; Shim, J.; Darian, E.; Guvench, O.; Lopes, P.; Vorobyov, I.; MacKerell Jr., A. D. CHARMM General Force Field: A Force field for Drug-Like Molecules Compatible with the CHARMM All-Atom Additive Biological Force Field. *J. Comput. Chem.* **2010**, *31*, 671–690.

[60] Vanommeslaeghe, K.; MacKerell Jr., A. D. Automation of the CHARMM General Force Field (CGenFF) I: bond perception and atom typing. *J. Chem. Inf. Model.* **2012**, *52*, 3144–3154.

[61] Vanommeslaeghe, K.; Raman, E. P.; MacKerell Jr., A. D. Automation of the CHARMM General Force Field (CGenFF) II: Assignment of bonded parameters and partial atomic charges. *J. Chem. Inf. Model.* **2012**, *52*, 3155–3168.

[62] Nikitin, A. M.; Lyubartsev, A. P. New six-site acetonitrile model for simulations of liquid acetonitrile and its aqueous mixtures. *J. Comput. Chem.* **2007**, *28*, 2020–2026.

[63] Shim, Y.; Choi, M. Y.; Kim, H. J. A molecular dynamics computer simulation study of room-temperature ionic liquids. I. Equilibrium solvation structure and free energetics. *The Journal of Chemical Physics* **2005**, *122*, 044510.

[64] Rahman, A.; Singwi, K. S.; Sjölander, A. Theory of Slow Neutron Scattering by Liquids. I. *Phys. Rev.* **1962**, *126*, 986–996.

[65] Colmenero, J.; Alvarez, F.; Arbe, A. Self-motion and the α relaxation in a simulated glass-forming polymer: Crossover from Gaussian to non-Gaussian dynamic behavior. *Phys. Rev. E* **2002**, *65*, 041804.

Heterogeneous Dynamics of Ionic Liquids: The Effects of Chain Length on Imidazolium-based Ionic Liquids

5.1 Introduction

In the previous chapter, the correlated dynamics of choline acetate and 1-butyl-3-methyl-imidazolium acetate was studied using a four point correlation function. Their dynamical behaviors were also compared with a traditional solvent, acetonitrile.

In this chapter, we extend our previous study to imidazolium ILs of different sizes, namely 1-ethyl-3-methyl-imidazolium acetate ([EMI][AC]), 1-butyl-3-methyl-imidazolium acetate ([BMI][AC]) and 1-octyl-3-methyl-imidazolium acetate ([OMI][AC]) (Figure 5.1). Their relaxation time and correlation length are examined using the four point correlation function. Additionally, in order to better investigate the correlated motions, a new correlation function is proposed based on the traditional four point correlation function.

5.2 Simulation Models and Methods

There different systems containing 512 [EMI][AC], [BMI][AC] and [OMI][AC] respectively were simulated with GROMCAS 2016 package[1]. ParamChem interface[2] was used to generate force field parameters with CHARMM General Force Field (CGenFF).[3–5] Leap frog algorithm was used to integrate the trajectories with a time step of 1 fs. Cubic periodic boundary condition was applied with particle mesh Ewald method[6] to calculate the long ranged electrostatic interactions. The van der Waals interactions were switched to zero gradually between 12 Å and 14 Å. Each system was first equalibrated at 800 K and 1 bar for 20 ns, and then annealed to 400 K in 10 ns, followed by 10 ns to determine the density (Table 5.1) in the isobaric-isothermal (NPT) ensemble using the Nosé-Hoover thermostat[7,8] and Parrinello-Rahman barostat. A 20 ns production was then performed with the determined density in isothermal (NVT) ensemble at 400 K. Trajectories were saved every 0.5 ps.

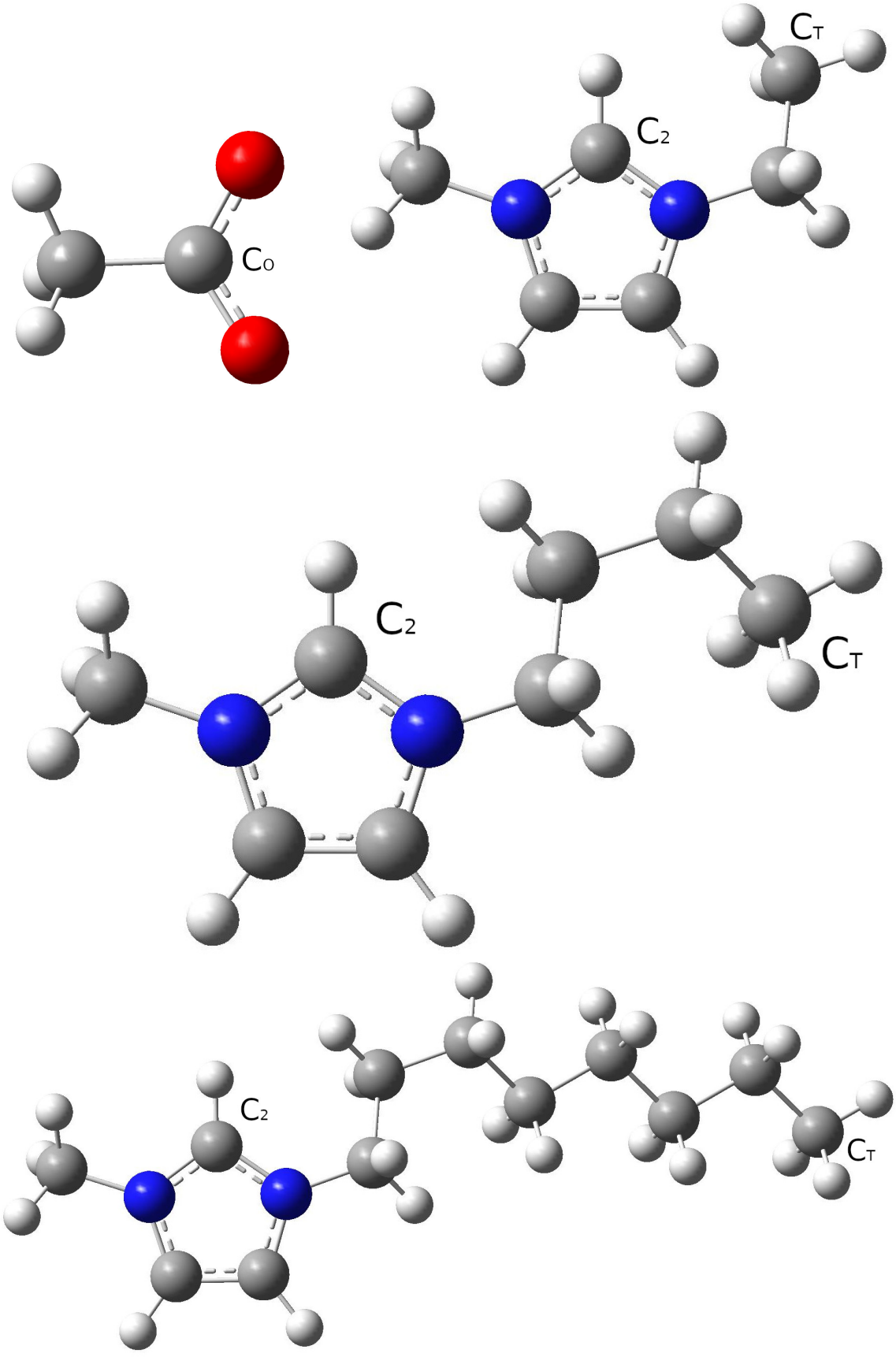

Figure 5.1: Notation of ionic liquids: acetate (top left), EMI (top right), BMI (middle) and OMI (bottom).

5.3 Results and Discussion

5.3.1 Radial Distribution Function

Most of the structures of the three imidazolium ILs represented in radial distribution functions (RDFs) are very similar (Figure 5.2). There are two closest counterion shells around 4 Å and 6 Å. The nearest like ion shell is located at around 8 Å. The structures of these shells have been discussed previously in section 4.3.1. As the chain length increases, the aggregation of the alkyl side chain becomes more prominent as shown in C_T-C_T. The reduction of the peak around 4.5 Å of C_O-C_T is likely due to the flexibility of longer alkyl chains.

5.3.2 Traditional Four Point Correlation Function

Time Dependent Order Parameter

Following the notation of Ref. 11, a time-dependent order parameter for species A can be defined as

$$Q_A^p(t) = \sum_{i,j \in A} \delta(|\vec{r}_i(0) - \vec{r}_j(t)|). \tag{5.1}$$

The delta function in Equation 5.1 is replaced with $w(r)$ (Equation 5.2) to avoid local vibration leading to Equation 5.3.

Table 5.1: Density at 400 K.

IL	Density (g/cm^3)	Experimental density (g/cm^3)
[EMI][AC]	1.045	1.061*
[BMI][AC]	0.993	1.013**
[OMI][AC]	0.934	-

* 363 K, Ref 9.
** 363 K, Ref 10.

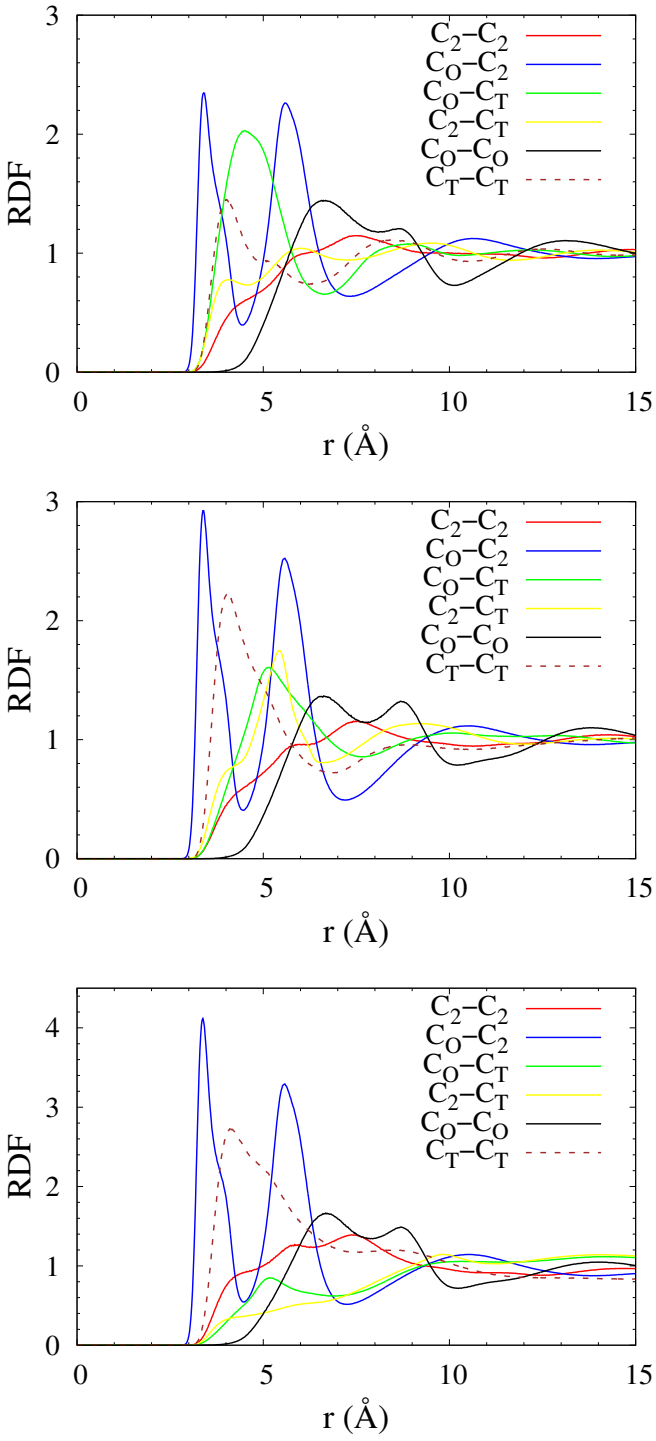

Figure 5.2: RDF of [EMI][AC] (top), [BMI][AC] (middle) and [OMI][AC] (bottom). C_2 stands for the C-2 on imidazolium rings; C_T stands for the terminal carbon of the longer side chain of cations; C_O stands for the carboxylic carbon of acetate anions.

$$w(r) = \begin{cases} 1 & \text{if } r < a \\ 0 & \text{if } r > a \end{cases} \tag{5.2}$$

$$Q_A(t) = \sum_{i,j \in A} w(|\vec{r}_i(0) - \vec{r}_j(t)|). \tag{5.3}$$

For IL systems, we employed $a = 1.424$ Å, which is 0.4σ of C_O atom. σ is the length parameter in the Lennard-Jones potential.

The relaxation of $\langle Q(t)/N \rangle$ in Figure 5.3 was found to be well fitted by the sum of multiple exponential decays, *i.e.*

$$\left\langle \frac{Q(t)}{N} \right\rangle = \sum_{i=1}^{4} A_i^Q \exp[-t/\tau_i^Q] + N_0. \tag{5.4}$$

Due to the finite a parameter in $w(r)$ function, we find that $N_0 = \langle Q(t)/N \rangle = V_0 n$, where n is the number density of the species and $V_0 = \frac{4}{3}\pi a^3$ is the effective volume of the delta function.

The shortest relaxation time, τ_1 in Table 5.2, of the three ILs are comparable, although C_T dynamics are faster than C_O and C_2. τ_2 and τ_3 show a similar trend. The four τ_i differ by roughly one order of magnitude except for τ_4 of [EMI][AC]. The larger relaxation time τ_3 and τ_4 increase significantly with the chain length. We think that the smaller relaxation time τ_1 and τ_2 represents local librational motions which are closely related to the atoms themselves, while the larger relaxation time τ_4 corresponds to the motions related to the whole ion or ion pair. We also calculate the averaged relaxation time using both direct numerical integration (τ_{int}) and from the fitted function ($\tau_{ave} = \sum_{i=1}^{4} A_i^Q \tau_i^Q$). The weights A_i^Q in Table 5.3 of the longer relaxation for C_2 and C_O are larger, while those of C_T are smaller. This leads to smaller τ_{int} and τ_{ave} for the latter. We also note that the large τ_4^Q of [OMI] C_T is likely due to a large fitting error.

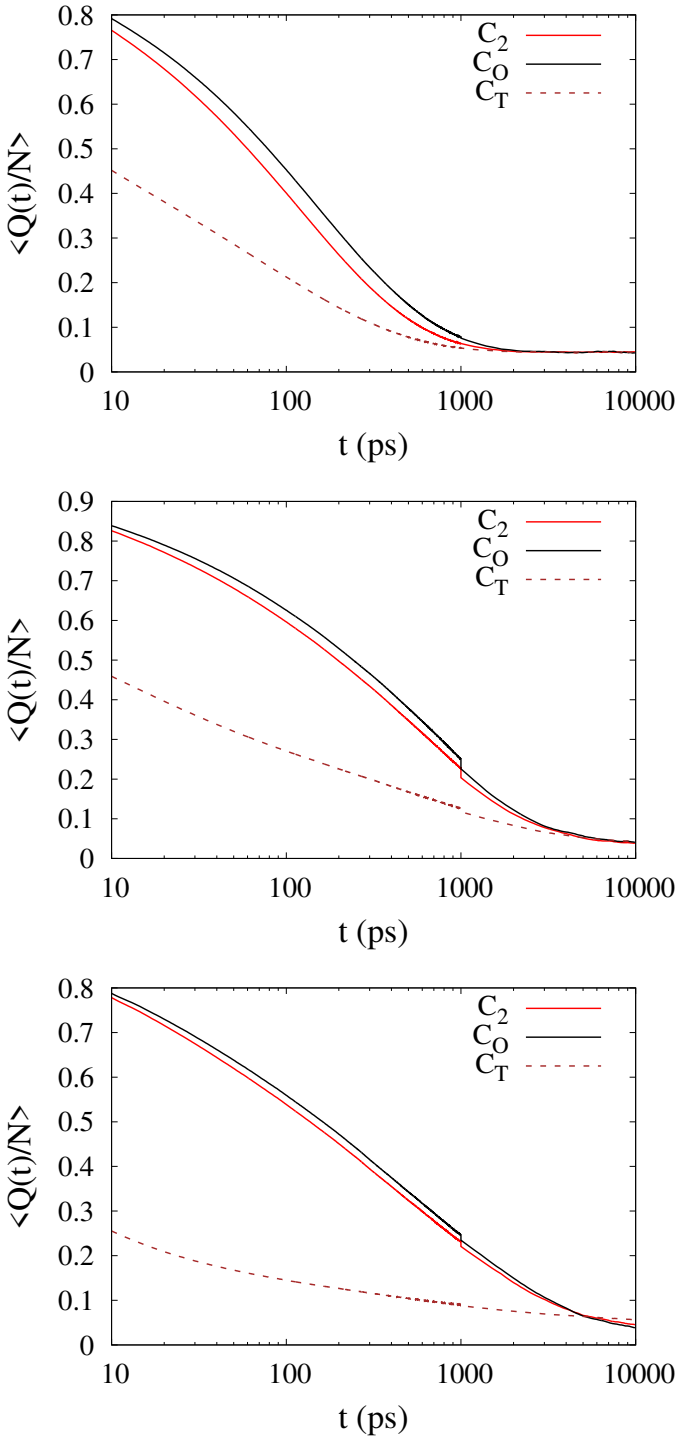

Figure 5.3: Time-dependent order parameter, $\langle Q(t)/N \rangle$, for [EMI][AC] (top), [BMI][AC] (middle), [OMI][AC] (bottom). C_2 stands for the C-2 on imidazolium rings; C_T stands for the terminal carbon of the longer side chain of cations; C_O stands for the carboxylic carbon of acetate anions.

Table 5.2: Fitted parameters for $\langle Q(t)/N\rangle = \sum_{i=1}^{4} A_i^Q \exp[-t/\tau_i^Q] + N_0$. τ_{int}^Q is calculated by numerical integration of $\langle Q(t)/N\rangle$, while $\tau_{ave}^Q = \sum_{i=1}^{4} A_i^Q \tau_i^Q$. C_2 stands for the C-2 on imidazolium rings; C_T stands for the terminal carbon of the longer side chain of cations; C_O stands for the carboxylic carbon of acetate anions.

IL	Atom	τ_{int}^Q	τ_{ave}^Q	τ_1^Q	τ_2^Q	τ_3^Q	τ_4^Q
EMI	C_O	178	185	2.53	24.1	122	432
	C_2	139	145	2.59	22.0	111	367
	C_T	66	69	0.83	10.0	77	335
BMI	C_O	675	624	2.16	31.1	174	1141
	C_2	599	572	3.27	37.7	215	1166
	C_T	338	286	0.77	16.5	153	1488
OMI	C_O	837	831	2.83	38.4	297	2248
	C_2	819	825	4.12	46.3	343	2558
	C_T	427	627*	0.70	12.2	226	8410*

* Not reliable due to large fitting error.

Table 5.3: Fitted parameters for $\langle Q(t)/N\rangle = \sum_{i=1}^{4} A_i^Q \exp[-t/\tau_i^Q] + N_0$. N_0 is calculated directly instead of fitting. C_2 stands for the C-2 on imidazolium rings; C_T stands for the terminal carbon of the longer side chain of cations; C_O stands for the carboxylic carbon of acetate anions.

IL	Atom	N_0	A_1^Q	A_2^Q	A_3^Q	A_4^Q
EMI	C_O	0.0447	0.12	0.17	0.34	0.32
	C_2	0.0447	0.13	0.19	0.36	0.27
	C_T	0.0447	0.37	0.22	0.21	0.15
BMI	C_O	0.0367	0.11	0.14	0.20	0.51
	C_2	0.0367	0.12	0.17	0.22	0.44
	C_T	0.0367	0.41	0.23	0.14	0.18
OMI	C_O	0.0266	0.16	0.20	0.28	0.33
	C_2	0.0266	0.18	0.21	0.29	0.28
	C_T	0.0266	0.60	0.21	0.08	0.07

Four Point Correlation Functions

The time evolution of the dynamic correlation between species A and B can be analyzed with the four-point overlap correlation function $g_4^{ol}(r,t)$

$$g_4^{ol}(\vec{r},t) = \frac{V}{N_A N_B} \left\langle \sum_{\substack{i,j \in A \\ k,l \in B}} \delta\left(\vec{r} - \vec{r}_k(0) + \vec{r}_i(0)\right) \times w\left(|\vec{r}_i(0) - \vec{r}_j(t)|\right) w\left(|\vec{r}_k(0) - \vec{r}_l(t)|\right) \right\rangle . \quad (5.5)$$

For simplicity, we consider a radially averaged correlation function, $g_4^{ol}(r,t)$, where $r = |\vec{r}|$.

Similar to the fitting for $\langle Q(t)/N \rangle$ in Equation 5.4, we fit $g_4^{ol}(r,t)$ for ILs with five exponential functions as

$$g_4^{ol}(r,t) = \sum_{i=1}^{5} A_i^{ol}(r) \exp[-t/\tau_i^{ol}(r)] + b(r) \ . \quad (5.6)$$

$b(r)$ in Equation 5.6 becomes $\langle Q_A(\infty)/N_A \rangle \langle Q_B(\infty)/N_B \rangle (= N_{A,0} N_{B,0})$ at large r.

The r-dependence of $\tau_i^{ol}(r)$ and their normalized weights $A_i^{ol}(r)/\sum_{i=1}^{5} A_i^{ol}(r)$ are displayed in Appendix B.1. As discussed in section 4.3.4, the different $\tau_i^{ol}(r)$ values correspond to different relaxation time-domains of $g_4^{ol}(r,t)$, and these relaxation time scales are largely r-independent. An example of C_O-C_O is shown in Figure 5.4. Figure 5.5 shows all the calculated relaxation time of [EMI][AC]. The relaxation behaviors of the polar atoms, C_O and C_2, are very similar, while the non-polar atom C_T shows faster relaxation. The r-dependence of relaxation of $g_4^{ol}(r,t)$ is mainly due to the weights $A_i^{ol}(r)$, which indicates that correlated pairs with different separation r share similar motions, however, their amplitudes are different.

The susceptibility $\chi_4(t)$, which describes the fluctuations of the order parameter

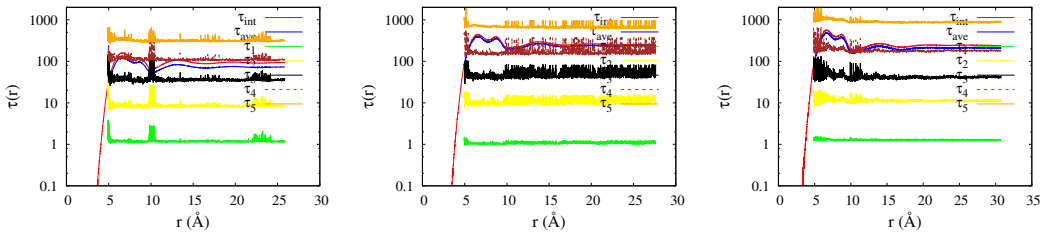

Figure 5.4: r-dependence of fitted parameters of $g^{ol}(r,t)$ of C_O-C_O: [EMI] (left), [BMI] (middle) and [OMI] (right).

of the system, is defined as

$$\chi_4(t) = \frac{\beta V}{N} \left[\langle Q(t)^2 \rangle - \langle Q(t) \rangle^2 \right], \tag{5.7}$$

with $\beta = 1/k_B T$. $\chi_4(t)$ measures cooperative motions of ions at two different locations, averaged over the system. The values of $\chi_4(t)$ generally describe the degree of the dynamical correlation in the system. The peak in $\chi_4(t)$ usually is related to the time scale of the correlated motions.

Figure 5.6 shows the MD results for the susceptibility for each system. The peaks of polar-polar groups move to large time scale when the chain length increases. However, the peaks related to C_T gradually move to smaller time scales. The peak height increases from [EMI][AC] to [BMI][AC], however, decreases slight in [HMI][AC]

The non-Gaussian factor $\alpha_2(t)$ defined in Equation 4.9 is also compuated and displayed in Figure 5.7. For polar groups, C_O and C_2, the peaks clearly shift to large time scales, especially from [EMI][AC] to [BMI][AC]. The trend of the peak posistion of C_T is less clear, shifting to larger time scale and then lower. This is similar to what we found in $\chi_4(t)$.

Dynamic Correlation Length

At the end of the traditional four point correlation function, we move to the dynamic length scale associated with cooperative motions in ILs. We follow the apporach used

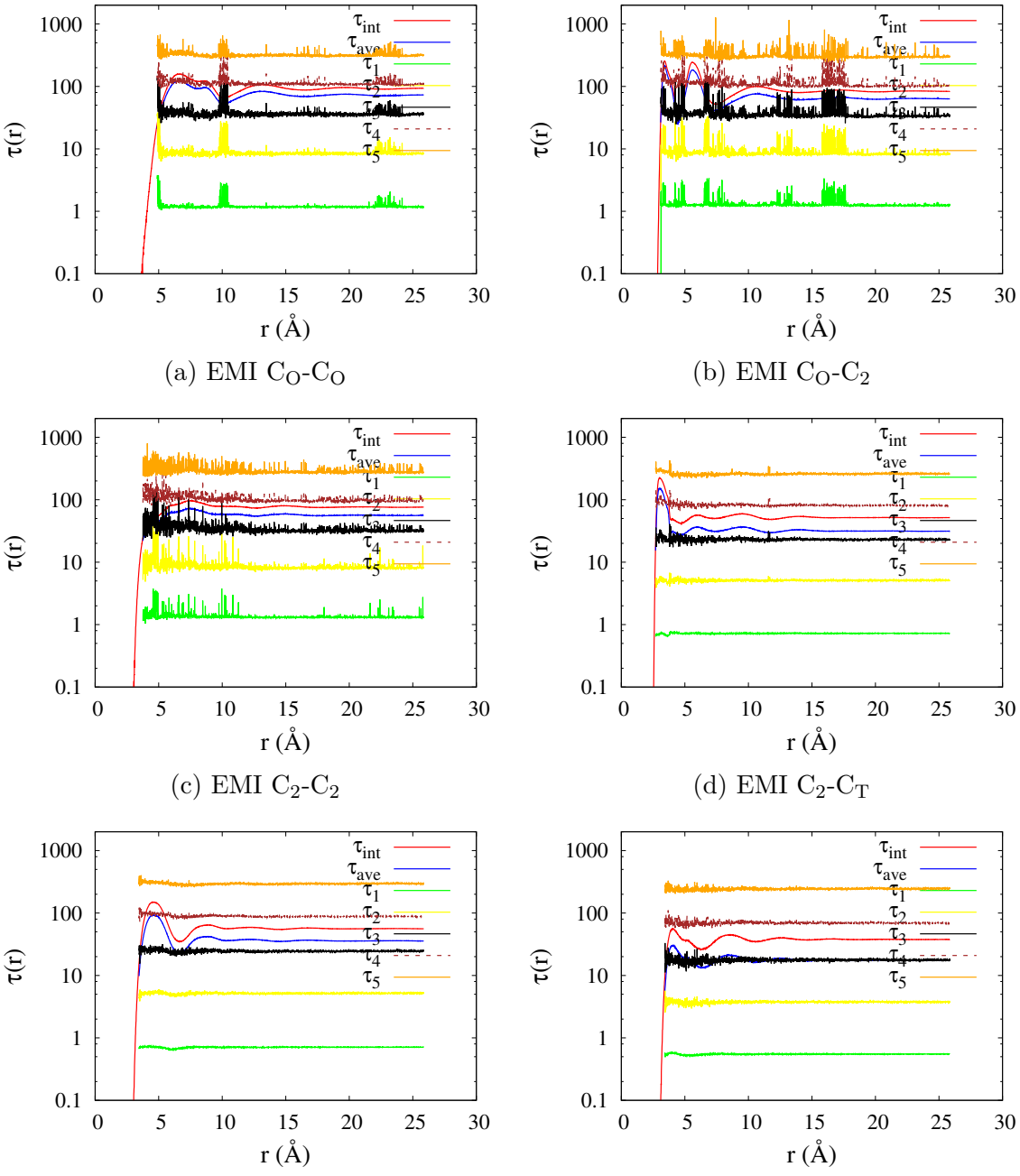

(a) EMI C_O-C_O (b) EMI C_O-C_2

(c) EMI C_2-C_2 (d) EMI C_2-C_T

(e) EMI C_O-C_T (f) EMI C_T-C_T

Figure 5.5: r-dependence of fitted parameters of $g^{ol}(r,t)$.

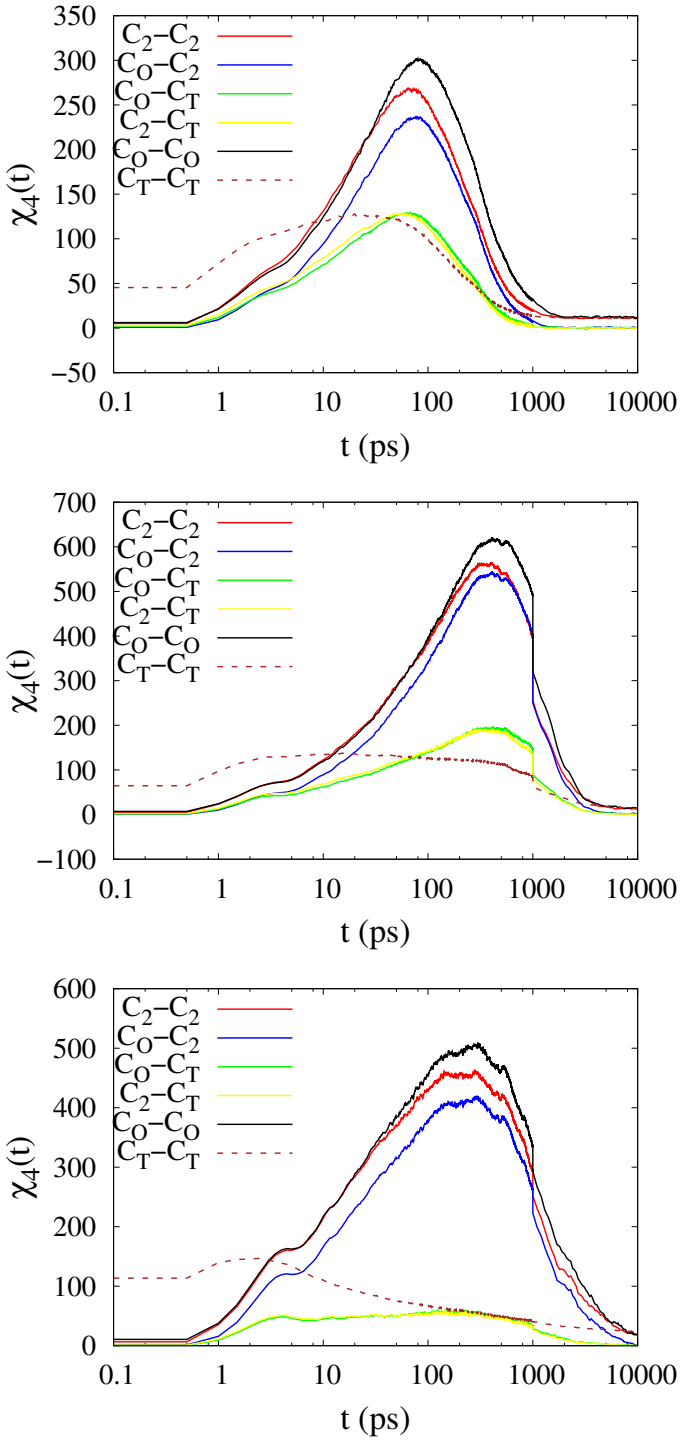

Figure 5.6: $\chi_4(t)$, for [EMI][AC] (top), [BMI][AC] (middle), [OMI][AC] (bottom).

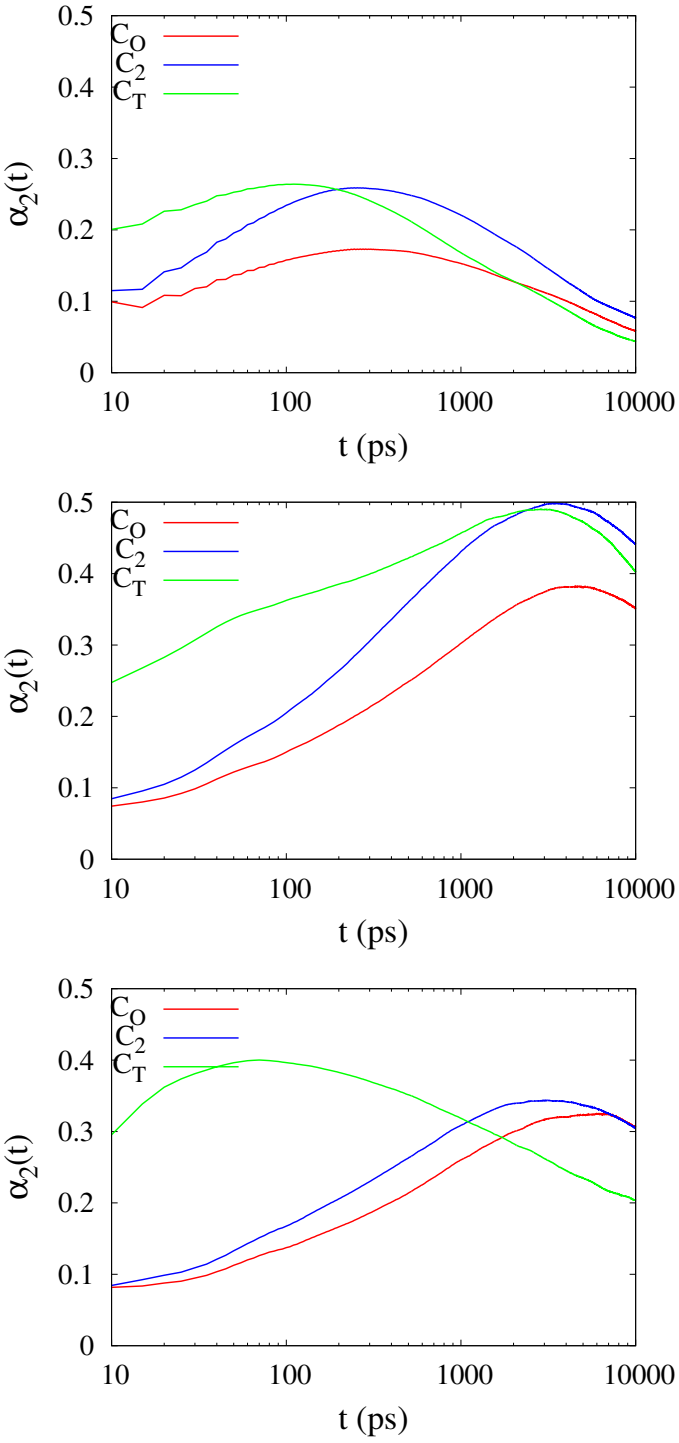

Figure 5.7: $\alpha_2(t)$, for [EMI][AC] (top), [BMI][AC] (middle), [OMI][AC] (bottom).

before in the previous section, small wave vector expansion of the four-point structure factor

$$S_4^{ol}(\vec{q},t) = \frac{1}{N_A}\left\langle \sum_{i,j\in A} \exp\,[i\vec{q}\cdot\vec{r}_i(0)]w(|\vec{r}_i(0)-\vec{r}_j(t)|) \times \sum_{k,l\in A} \exp\,[-i\vec{q}\cdot\vec{r}_k(0)]w(|\vec{r}_k(0)-\vec{r}_l(t)|)\right\rangle . \tag{5.8}$$

The inclusion up to the q^2 terms in the expansion à la Ornstein-Zernike (OZ) theory yields[11,12]

$$S_4^{ol}(q,t) = \frac{S_4^{ol}(0,t)}{1+(q\xi_4(t))^\alpha} \tag{5.9}$$

with $\alpha = 2$. The corresponding r-space behavior ($\alpha = 2$) is given by

$$g_4^{ol}(r,t) \propto \frac{S_4^{ol}(0,t)}{r\xi_4(t)^2}\exp[-r/\xi_4(t)]\ . \tag{5.10}$$

The results are presented in Figure 5.8. The typical maximum correlated lengths of the polar groups are around 5Å, 7Å and 4Å for [EMI][AC], [BMI][AC] and [OMI][AC] respectively. For the non-polar group, C_T, correlated length decreases from 3Å in [EMI][AC] to almost zero in [OMI][AC]. This agrees with our expectation that the electrostatic interactions dominate the correlated dynamics. The increase in the chain length initially increases the size of the ions and hence increases the correlated length. However, further increase in the chain length dilutes the electrostatic interactions, and hence weakens the correlated dynamics.

5.3.3 "Mobile" Self Four Point Correlation Function

In this section, we consider a new "mobile" self four point correlation function. In the traditional four point correlation function, the locations of the particles at time

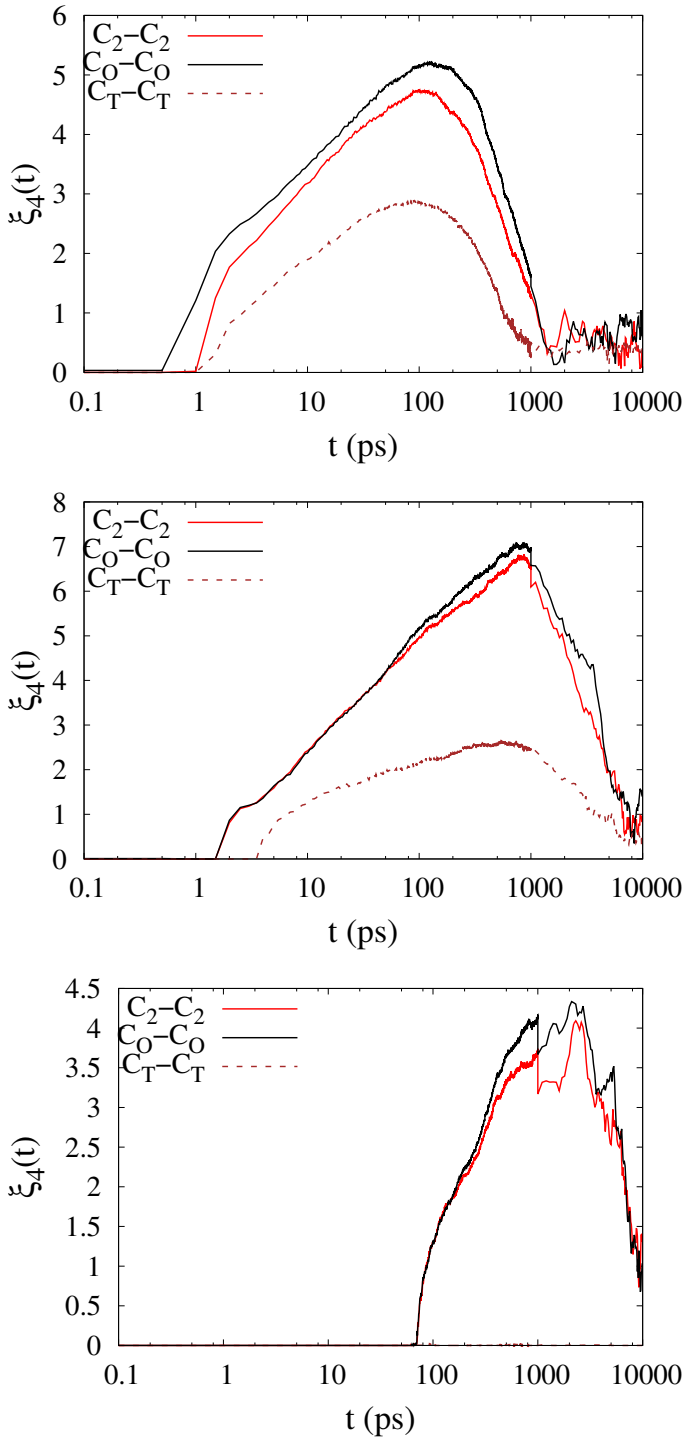

Figure 5.8: Dynamic correlation length, $\xi_4(t)$, for [EMI][AC] (top), [BMI][AC] (middle), [OMI][AC] (bottom).

t are the same as the original positions at time 0. However, this definition does not account for correlated particles maintaining relative positions as they move. In order to study such correlated dynamics, we introduce "mobile" self four point correlation function as

$$g_4^m(r_{AB}, r_{COM}, t) = \frac{V}{N_A N_B} \left\langle \sum_{\substack{i\in A \\ j\in B}} \delta(|\vec{r}_{ij}^{COM}(t) - \vec{r}_{ij}^{COM}(0)| - r_{COM}) \right. \\ \left. \times \delta(|\vec{r}_{ij}(0)| - r_{AB})\delta(|\vec{r}_{ij}(t)| - r_{AB}) \right\rangle \quad (5.11)$$

where $r_{ij}(t)$ is the distance of atom i and j at time t, and $\vec{r}_{ij}^{COM}(t)$ is the center of mass of atom i and j at time t. It is named as "self" four point correlation function because particles i and j have to the same particles at time 0 and t. It corresponds to self-self four point correlation function in the traditional case.[11]

Similar to the four point correlation function considered earlier, the last delta function is replaced by the coarse-grained $w(r)$ while sampling the trajectories.

$$g_4^m(r_{AB}, r_{COM}, t) = \frac{V}{N_A N_B} \left\langle \sum_{\substack{i\in A \\ j\in B}} \delta(|\vec{r}_{ij}^{COM}(t) - \vec{r}_{ij}^{COM}(0)| - r_{COM}) \right. \\ \left. \times \delta(|\vec{r}_{ij}(0)| - r_{AB})w(|\vec{r}_{ij}(t)| - r_{AB}) \right\rangle \quad (5.12)$$

Since it is difficult to analyze a three dimentional function, we integrate $g_4^m(r_{AB}, r_{COM}, t)$ over r_{COM}, it leads to a pair-wise correlation function at different distance r_{AB}

$$c^m(r_{AB}, t) = \int \mathrm{d}r_{COM}\ 4\pi r_{COM}^2 g_4^m(r_{AB}, r_{COM}, t) \quad (5.13)$$

$$= \frac{V}{N_A N_B} \left\langle \sum_{\substack{i\in A \\ j\in B}} \delta(|\vec{r}_{ij}(0)| - r_{AB})\delta(|\vec{r}_{ij}(t)| - r_{AB}) \right\rangle. \quad (5.14)$$

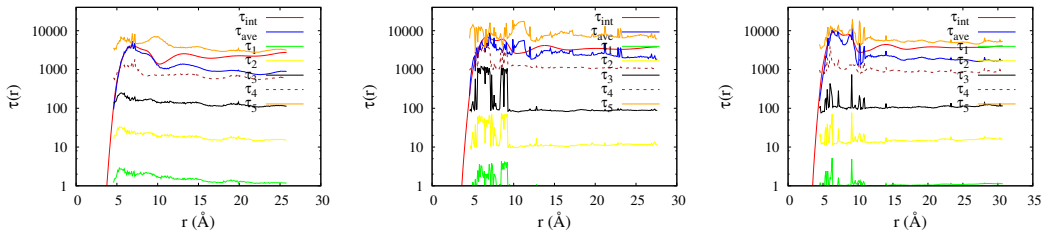

Figure 5.9: r-dependence of fitted parameters of $c^m(r,t)$ of C_O-C_O: [EMI] (left), [BMI] (middle) and [OMI] (right).

This is a "mobile" extension of the overlap four point correlation function $g_4^{ol}(r,t)$. Hence, we can fit the correlation function with a multi-exponential function.

$$c^m(r,t) = \sum_{i=1}^{5} A_i^m(r) \exp[-t/\tau_i^m(r)] + b(r) \ . \tag{5.15}$$

The complete results are shown in Appendix B.2. The average relaxation time scale $\tau_{ave}^m(r) = \sum_{i=1}^5 A_i^m(r)\tau_i^m(r)$ is calculated from the fitted exponential function, and τ_{int}^m is computed by a direct integration. The divergence of the two methods at large r may be due to the constant term, $b(r)$. There are many similarities between the two four point correlation functions. The same atom has similar relaxation time in different ions (Figure 5.9). The weights still show significant r-dependence. (For details, see Appendix B.2.) Non-polar groups relax faster than polar groups. We also notice several difference between the two four point correlation functions. First, the "mobile" definition yeilds larger time scales (about 10 times) especially for the two slowest relaxation time, $\tau_4^m(r)$ and $\tau_5^m(r)$. It means the collective motions not only include particles frozen at their original positions, but also involve collective translation or reorientation. This also provides an evidence that those time scales should be assigned to traditional or reorientational motions. Second, there are some r-dependence in $\tau^m(r)$, for example in Figure 5.10.

If we further integrate $c^m(r,t)$ over r, we obtain the average correlation function over the distance, $c(t) = \int \mathrm{d}r \ c^m(r,t)$. Here, we first determine the solvation

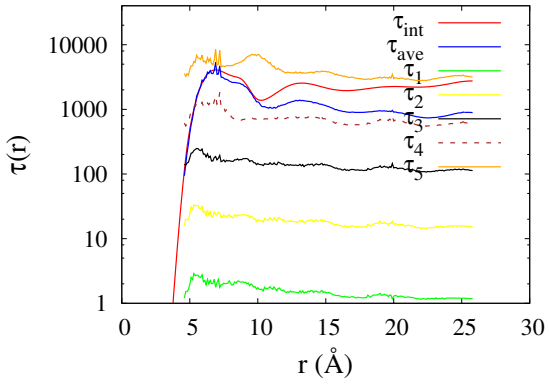

(a) EMI C_O-C_O

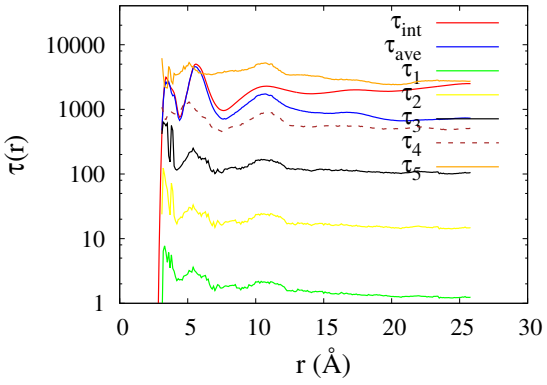

(b) EMI C_O-C_2

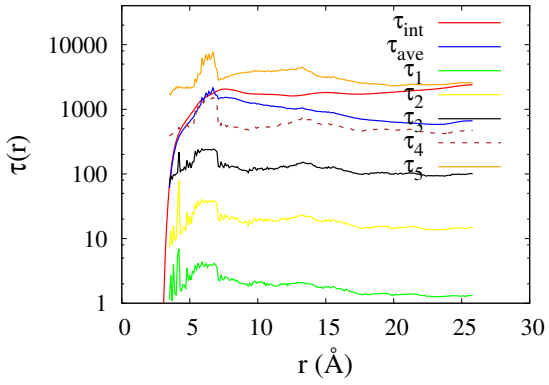

(c) EMI C_2-C_2

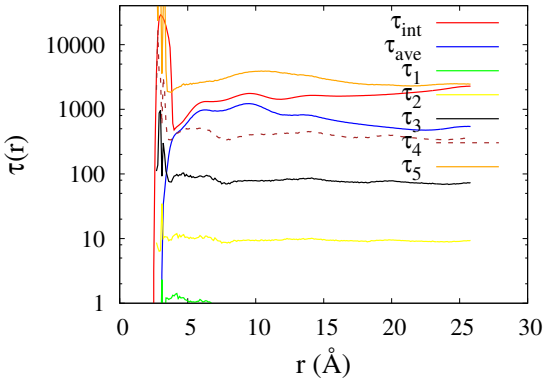

(d) EMI C_2-C_T

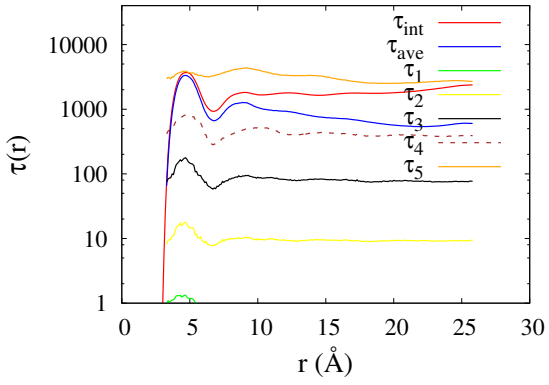

(e) EMI C_O-C_T

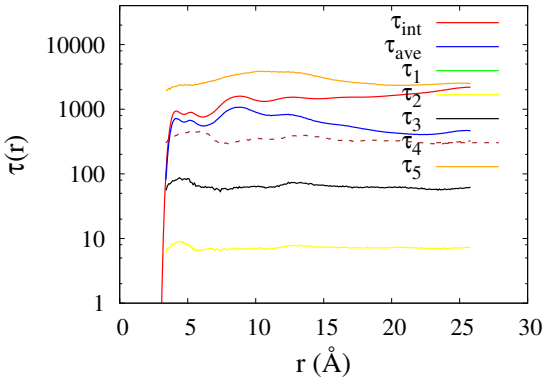

(f) EMI C_T-C_T

Figure 5.10: r-dependence of fitted parameters of $c^m(r,t)$.

shell from the RDF and then calculate the average correlation function $c(t)$ within the given solvation shell. We extract the relaxation times using a similar fitting $c(t) = \sum_{i=1}^{5} A_i^c \exp[-t/\tau_i^c] + N_0$ as before. The results are tabulated in Table 5.4 and Table 5.5. Generally, these results agree with what we found for $\langle Q(t)/N \rangle$, e.g. non-polar groups are faster than polar groups, weights of smaller relaxation time for non-polar groups are larger and relaxation time increases with chain length. We also note that the largest relaxation time τ_5^c may not be accurate due to large fitting errors.

Finally, we turn to the translational motions of these correlated particles. We calculate the mean square displacement of the combined correlated particles as

$$MSD^m(t) = \frac{\int_{r_1}^{r_2} 4\pi r_{AB}^2 \mathrm{d}r_{AB} \int 4\pi r_{COM}^2 \mathrm{d}r_{COM}\ r_{COM}^2 g_4^m(r_{AB}, r_{COM}, t)}{\int_{r_1}^{r_2} 4\pi r_{AB}^2 \mathrm{d}r_{AB} \int 4\pi r_{COM}^2 \mathrm{d}r_{COM}\ g_4^m(r_{AB}, r_{COM}, t)} \tag{5.16}$$

where r_1 and r_2 are the lower and upper bound of the solvation shell determined from RDF. In this definition, the correlation function $g_4^m(r_{AB}, r_{COM}, t)$ is treated as a probability distribution of finding a correlated particle pair. The diffusion coefficients are calculated using Einstein relation,

$$D^m = \frac{1}{6} \frac{\mathrm{d}}{\mathrm{d}t} MSD^m(t). \tag{5.17}$$

Along with the traditional single atom diffusion coefficients, the results are shown in Table 5.6. We observe that strongly correlated pairs, e.g. polar groups, tend to have smaller diffusion coefficients, usually about one half of that of the single atom. Less correlated pairs, especially for C_T-C_T and C_2-C_T, have relatively larger diffusion coefficients.

Table 5.4: Fitted parameters τ^c for $c(t) = \sum_{i=1}^{5} A_i^c \exp[-t/\tau_i^c] + N_0$. τ_{int}^c is calculated by numerical integration of $c(t)$, while $\tau_{ave}^c = \sum_{i=1}^{5} A_i^c \tau_i^c$. C_2 stands for the C-2 on imidazolium rings; C_T stands for the terminal carbon of the longer side chain of cations; C_O stands for the carboxylic carbon of acetate anions.

IL	Atom	Shell (Å)	τ_{int}^c	τ_{ave}^c	τ_1^c	τ_2^c	τ_3^c	τ_4^c	τ_5^c
EMI	C_O-C_O	0-10	2479	2068	2.14	24.0	176	891	4857
	C_O-C_O	10-17	2125	1170	1.61	19.6	142	724	3934
	C_O-C_2	0-4.5	1444	1433	2.98	21.1	158	859	4023
	C_O-C_2	4.5-7.3	2143	1873	2.83	27.3	191	905	3835
	C_O-C_2	7.3-14	1846	1187	1.97	21.1	142	658	3974
	C_O-C_T	0-10	1650	1270	1.02	11.2	101	550	3534
	C_2-C_2	0-12.5	1604	1148	2.51	23.0	141	581	3241
	C_2-C_T	0-10	3500	677	1.02	10.0	86	429	2924
	C_T-C_T	0-10	1092	750	0.69	7.4	69	376	2878
BMI	C_O-C_O	0-10	4424	3597	0.80	10.0	87	1294	8215
	C_O-C_O	10-17	3501	3397	0.83	11.1	89	1194	9844
	C_O-C_2	0-4.5	4252	3779	5.79	72.9	1279	1794	5500
	C_O-C_2	4.5-7.3	4660	5165*	4.83	69.6	1255	3214	13618*
	C_O-C_2	7.3-14	3410	2769	0.95	11.7	92	1163	7941
	C_O-C_T	0-10	3046	1941	0.69	10.1	75	1029	5802
	C_2-C_2	0-12.5	3440	3073	1.09	11.3	89	1171	7727
	C_2-C_T	0-10	3532	1534	0.72	10.1	75	1051	5773
	C_T-C_T	0-10	2168	1849	0.53	8.6	69	1172	6704
OMI	C_O-C_O	0-10	5324	4026	1.15	14.8	109	1183	8767
	C_O-C_O	10-17	3934	2155	1.02	13.9	102	924	5449
	C_O-C_2	0-4.5	5445	11283*	7.45	99.3	943	3023	16942*
	C_O-C_2	4.5-7.3	5842	2569	0.50	14.6	408	4391	6988
	C_O-C_2	7.3-14	4014	3174	1.14	14.1	106	1095	8050
	C_O-C_T	0-10	2202	909	0.70	7.9	59	492	3832
	C_2-C_2	0-12.5	4327	3574	1.29	13.5	101	1148	8470
	C_2-C_T	0-10	2349	797	0.73	7.9	59	477	3491
	C_T-C_T	0-10	1991	813	0.54	6.7	55	494	4920

* Not reliable due to large fitting error.

Table 5.5: Fitted parameters A_i^c for $c(t) = \sum_{i=1}^{5} A_i^c \exp[-t/\tau_i^c] + N_0$. C_2 stands for the C-2 on imidazolium rings; C_T stands for the terminal carbon of the longer side chain of cations; C_O stands for the carboxylic carbon of acetate anions.

IL	Atom	Shell (Å)	A_1^c	A_2^c	A_3^c	A_4^c	A_5^c
EMI	C_O-C_O	0-10	0.04	0.06	0.18	0.29	0.37
	C_O-C_O	10-17	0.06	0.08	0.21	0.32	0.23
	C_O-C_2	0-4.5	0.01	0.02	0.09	0.66	0.21
	C_O-C_2	4.5-7.3	0.03	0.05	0.15	0.32	0.40
	C_O-C_2	7.3-14	0.06	0.08	0.22	0.32	0.24
	C_O-C_T	0-10	0.10	0.09	0.16	0.30	0.31
	C_2-C_2	0-12.5	0.05	0.08	0.21	0.33	0.29
	C_2-C_T	0-10	0.08	0.08	0.14	0.22	0.19
	C_T-C_T	0-10	0.16	0.13	0.17	0.28	0.22
BMI	C_O-C_O	0-10	0.02	0.03	0.07	0.31	0.39
	C_O-C_O	10-17	0.05	0.05	0.10	0.39	0.30
	C_O-C_2	0-4.5	0.01	0.03	0.06	0.17	0.61
	C_O-C_2	4.5-7.3	0.03	0.05	0.18	0.29	0.29
	C_O-C_2	7.3-14	0.04	0.05	0.10	0.38	0.29
	C_O-C_T	0-10	0.11	0.10	0.11	0.25	0.29
	C_2-C_2	0-12.5	0.03	0.04	0.10	0.39	0.34
	C_2-C_T	0-10	0.10	0.09	0.11	0.27	0.22
	C_T-C_T	0-10	0.17	0.12	0.12	0.31	0.22
OMI	C_O-C_O	0-10	0.03	0.03	0.06	0.19	0.43
	C_O-C_O	10-17	0.06	0.06	0.10	0.22	0.36
	C_O-C_2	0-4.5	0.01	0.03	0.08	0.26	0.61
	C_O-C_2	4.5-7.3	0.01	0.04	0.10	0.31	0.17
	C_O-C_2	7.3-14	0.05	0.06	0.10	0.27	0.36
	C_O-C_T	0-10	0.18	0.16	0.15	0.16	0.21
	C_2-C_2	0-12.5	0.03	0.04	0.09	0.28	0.38
	C_2-C_T	0-10	0.17	0.16	0.15	0.16	0.20
	C_T-C_T	0-10	0.26	0.18	0.15	0.12	0.15

Table 5.6: Diffusion coefficients of correlated particles using $D^m = \frac{1}{6}\frac{\mathrm{d}}{\mathrm{d}t}MSD^m(t)$. C_2 stands for the C-2 on imidazolium rings; C_T stands for the terminal carbon of the longer side chain of cations; C_O stands for the carboxylic carbon of acetate anions. Units: $10^{-12}\ m^2/s$

Atom	Shell (Å)	EMI	BMI	OMI
C_O-C_O	0-10	13.1	3.8	3.0
C_O-C_O	10-17	12.9	3.5	2.6
C_O-C_2	0-4.5	16.5	4.7	3.4
C_O-C_2	4.5-7.3	16.1	4.6	3.2
C_O-C_2	7.3-14	15.7	4.0	2.7
C_O-C_T	0-10	15.9	5.1	4.2
C_2-C_2	0-12.5	19.2	4.6	2.9
C_2-C_T	0-10	29.2	6.8	4.9
C_T-C_T	0-10	19.4	6.6	5.1
C_O	atom	22.5	6.7	5.1
C_2	atom	36.5	8.5	5.1
C_T	atom	36.5	10.5	9.2

5.4 Conclusions

In this section, we studied the effects of the length of side chains on the correlated dynamics using the traditional four point correlation function and our newly proposed "mobile" self four point correlation function. We found the length of the side chain has rather complicated impacts. Correlation time scales typically increase with side chain length, and the non-polar side chain, C_T, becomes less correlated with other atoms. However, the correlated length scales of polar atoms first increase and then decrease while chain length increases, while the correlated length scales of non-polar atoms decrease monotonically. We attributed this pheonomenom to the strength of electrostatic interactions.

Our "mobile" self four point correlation function provides a better definition of correlated dynamics to allow translational and reorientational motions. It provides an evidence that the two slower relaxation relates to translational or reorientational motions. The diffusion of the correlated pairs is also compared with that of single

atom.

[1] van der Spoel, D.; Lindahl, E.; Hess, B.; Groenhof, G.; Mark, A. E.; Berendsen, H. J. C. GROMACS: Fast, flexible, and free. *Journal of Computational Chemistry* **2005**, *26*, 1701–1718.

[2] https://www.paramchem.org.

[3] Vanommeslaeghe, K.; MacKerell, A. D. Automation of the CHARMM general force field (CGenFF) I: Bond perception and atom typing. *Journal of Chemical Information and Modeling* **2012**, *52*, 3144–3154.

[4] Vanommeslaeghe, K.; Raman, E. P.; MacKerell, A. D. Automation of the CHARMM general force field (CGenFF) II: Assignment of bonded parameters and partial atomic charges. *Journal of Chemical Information and Modeling* **2012**, *52*, 3155–3168.

[5] Vanommeslaeghe, K.; Hatcher, E.; Acharya, C.; Kundu, S.; Zhong, S.; Shim, J.; Darian, E.; Guvench, O.; Lopes, P.; Vorobyov, I.; Mackerell, A. D. CHARMM general force field: A force field for drug-like molecules compatible with the CHARMM all-atom additive biological force fields. *Journal of Computational Chemistry* **2010**, *31*, 671–690.

[6] Darden, T.; York, D.; Pedersen, L. Particle mesh Ewald: An N log(N) method for Ewald sums in large systems. *The Journal of Chemical Physics* **1993**, *98*, 10089–10092.

[7] Nosé, S. A unified formulation of the constant temperature molecular dynamics methods. *The Journal of Chemical Physics* **1984**, *81*, 511–519.

[8] Nosé, S. A molecular dynamics method for simulations in the canonical ensemble. *Molecular Physics* **1984**, *52*, 255–268.

[9] Freire, M. G.; Teles, A. R. R.; Rocha, M. A. A.; Schröder, B.; Neves, C. M. S. S.; Carvalho, P. J.; Evtuguin, D. V.; Santos, L. M. N. B. F.; Coutinho, J. A. P. Thermophysical Characterization of Ionic Liquids Able To Dissolve Biomass. *Journal of Chemical & Engineering Data* **2011**, *56*, 4813–4822.

[10] Almeida, H. F. D.; Passos, H.; Lopes-da Silva, J. A.; Fernandes, A. M.; Freire, M. G.; Coutinho, J. A. P. Thermophysical Properties of Five Acetate-Based Ionic Liquids. *Journal of Chemical & Engineering Data* **2012**, *57*, 3005–3013.

[11] Lačević, N.; Starr, F. W.; Schrøder, T. B.; Glotzer, S. C. Spatially heterogeneous dynamics investigated via a time-dependent four-point density correlation function. *J. Chem. Phys.* **2003**, *119*, 7372–7387.

[12] Berthier, L. Time and length scales in supercooled liquids. *Phys. Rev. E* **2004**, *69*, 020201.

Vibrational Spectroscopy of Imidazolium-based Ionic Liquids: A Combined MD/DFT Study

6.1 Introduction

Ionic liquids (ILs) are purely ionic systems, consisting exclusively of organic cations and organic/inorganic anions. Because of their many appealing properties such as low melting points, non-volatility, non-flammability, good thermal stability and wide electrochemical window, they have received an extensive attention recently.[1–5] At the fundamental level, it is the intermolecular interactions that govern physical and chemical properties of liquids. Thus a proper understanding of interionic interactions is crucial to design, synthesis and optimization of ionic compounds to tailor ILs' properties for task-specific applications.

One of the important molecular-level interactions is hydrogen bonds. Their presence, or lack thereof, exerts a strong influence on structure and physicochemical properties of liquids. As such, roles of hydrogen-bonded interactions for ILs have been widely discussed.[6–26] A typical criterion for the existence of a hydrogen bond between two moieties X-H and Y invokes geometrical conditions, such as the distance between X and Y less than the sum of their van der Waals radii and near linear arrangement of X, H and Y. In view of its ad hoc nature, however, different criteria based on directly measurable spectroscopic quantities have also been considered.[27,28] For instance, X-H stretching vibrations can provide illuminating insight into the hydrogen-bonded interactions of X-H with Y because the direction and extent of their frequency shift caused by these interactions depend on the X-H bond polarity and electronegativity of atoms involved, modulated by their structure.[28] Therefore, vibrational spectroscopy, such as IR and Raman, offers an excellent tool to probe molecular structures, including hydrogen-bond structures since the vibrational frequencies and line shapes are strongly modulated by local molecular structures through intra- and inter-molecular interactions.

The characterization of the C-H stretching region of ILs consisting of 1-alkyl-3-

methylimidazolium cations (Figure 6.1) has generated a considerable interest as a way to probe the anion structure near cations.[18] According to experimental studies via infrared and Raman spectroscopy,[20,21] stretching vibrations of acidic hydrogen of the imidazolium ring—*viz.*, H11 bonded to C2 in the case of BMI^+ in Figure 6.1—show frequency shifts that vary with the basicity of the anion. As the the anion becomes more basic, the C2-H11 vibrations shift toward lower frequencies. This suggests that specific interactions between C2-H11 and anions are present and that their interaction strength depends on the hydrogen-bond accepting power of anions.[29]

Useful insights into hydrogen-bonded interactions in ILs can be gained via *ab initio* and DFT calculations[23–25] though the inclusion of the effect of the fluctuating solvation environment is challenging. Classical MD is a popular method that enables reliable sampling of solvent fluctuations at the molecular level. For example, MD coupled with X-Ray diffraction[30] and absorption spectroscopy[31–33] was employed to study the structure of imidazolium halide ILs. Dielectric relaxation and related spectroscopies[34] of imidazolium-based ILs, as well as the influence of the ion charges and charge distributions on their structure and dynamics,[35–37] were also examined via MD. However, intrinsically quantum mechanical properties, such as vibrational frequency shifts induced by hydrogen bonds, would require a more elaborate framework than typical classical descriptions used in simulations. In this context, *ab initio* MD offers an attractive alternative.[38–42] Nevertheless, applications of the computationally expensive *ab initio* method to IL systems can be limited because extended simulations are needed to ensure proper sampling of highly viscous ILs.

In this article, we employ a QM/MM strategy[43] to calculate C-H stretching vibrations of the cation imidazolium ring in BMI^+-based ILs (Figure 6.1). We extend the method employed in refs. 44 and 45 to bulk ILs by considering all possible cation-anion pairs in a given IL configuration determined via classical MD simulations, treating each of ion pairs as a quantum subsystem via the DFT method and averag-

ing over multiple configurations. The QM/MM results thus obtained are compared with the classical MD predictions for C-H vibrational spectra. The disagreement between the two exposes the importance of the proper treatment of electronic structure, modulated by the local solvation environment, in vibrational analysis. Additionally, comparison of QM/MM results based on different force field models provide insight into the key factors that govern vibrational properties of ILs.

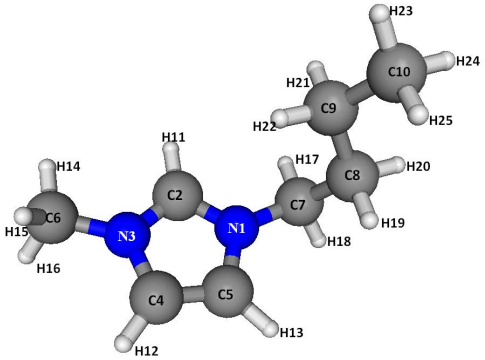

Figure 6.1: Molecular structure of 1-butyl-3-methylimidazolium

The outline of this paper is as follows: In sec 6.2, the models and methods employed in our calculations are described. Classical MD results for IL structure and QM/MM predictions for C-H vibrations of the imidazolium ring obtained with MD configurations are presented in sec 6.3. Comparison of the QM/MM and MD results for C-H vibrations is also made there. Sec 6.4 concludes.

6.2 Models and Methods

Classical MD simulations were performed to study structure and C-H stretching vibrations of three different ILs, BMI^+Cl^-, BMI^+Br^- and $BMI^+BF_4^-$, using the GROMACS software.[46] The simulation cell comprises 125 pairs of cations and anions. Two different force field models, OPLS-AA[47,48] and CHARMM,[49,50] were considered. For the former, the parameters developed by Lopes, Deschamps and Pádua (LDP) based on OPLS-AA force field were employed for BMI^+.[51,52] In the LDP description,

C2-H11, C4-H12 and C5-H13 bonds are constrained, *i.e.*, rigid.[51] Since their stretching vibrations are essential to MD analysis of IR spectra, we have assigned them a force constant that is the same as the force constant of alkyl C-H bonds in OPLS-AA. Hereafter, this modified LDP description employed in our study will be referred to as the OPLS-AA force field for simplicity. In the case of CHARMM, the parameters generated via ParamChem v.0.9.7 interface[53] that automatically assigns atom types, force field parameters and charges on molecules based on the 2b8 release of the CHARMM General Force Field[54–56] were employed for BMI^+. For anions, we employed parameters from ref 57 for both CHARMM and OPLS-AA. Their combination rules for non-bonded interactions follow the CHARMM and OPLS-AA convention, respectively. The force field parameters used in the present study are compiled in Appendix C.1.

All simulations were conducted in the isothermal-isobaric (NPT) ensemble at 350 K and 1 atm using the GROMACS program.[46] This thermodynamic condition allows for a direct comparison with the available IR results[21] for the ILs studied here. The simulation cell was a cubic box and periodic boundary conditions were applied. Non-bonded interactions were computed with a 14 Å cut-off. Electrostatic interactions were computed using the particle mesh Ewald method.[58] Simulations were carried out with 10 ns of annealing from 800 K to 350 K and 10 ns of equilibration at 350 K, followed by a 20 ns trajectory from which equilibrium structure was computed. The time step employed was 1 fs.

For C-H vibrational spectrum calculations, we first selected ten distinct configurations that are separated by 4 ns in time from two 20 ns equilibrium trajectories. With each of these ten configurations employed as an initial configuration, we simulated ten 1 ns trajectories with a time step of 0.3 fs, from which the velocity auto-correlation function (Equation (6.5) below) associated with C-H vibrations was computed. In the present study, we considered only C-H bonds of the BMI^+ ring. The IR absorption

$\alpha(\omega)$ due to vibrations of a specific C-H bond (for example, C2-H11 in Figure 6.1) is determined by[59]

$$n(\omega)\,\alpha(\omega) = \frac{4\pi^2\omega}{3\hbar cV}\left(1 - e^{-\beta\hbar\omega}\right) I(\omega)\ ; \tag{6.1}$$

$$I(\omega) = \frac{1}{2\pi}\int_{-\infty}^{\infty} dt\, e^{-i\omega t} \sum_i \langle \mu_i(t)\cdot\mu_i\rangle\ , \tag{6.2}$$

where i labels ions, $\vec{\mu}_i$ is the dipole moment of the bond, $n(\omega)$ is the index of refraction of the medium, c is the speed of light in vacuum, $I(\omega)$ is the absorption lineshape function, and β is the inverse temperature in units of k_B (*i*.e., $\beta = 1/k_BT$). Since nuclear motions are treated classically in the simulations, we corrected the MD result $I_{\rm MD}(\omega)$ for the lineshape function via

$$I(\omega) = \frac{\beta\hbar\omega}{1 - e^{-\beta\hbar\omega}}\, I_{\rm MD}(\omega)\ , \tag{6.3}$$

so that the resulting $I(\omega)$ satisfies the detailed balance condition[59]

$$I(-\omega) = e^{-\beta\hbar\omega} I(\omega)\ . \tag{6.4}$$

Substituting Equation (6.3) into Equation (6.2), we find

$$n(\omega)\,\alpha(\omega) = \frac{4\pi\beta}{3cV}\int_0^{\infty} dt\, \cos\omega t \left(\frac{\partial\mu}{\partial r}\right)^2 \sum_i \langle v_i(t)\cdot v_i\rangle\ , \tag{6.5}$$

where v_i is the relative velocity of the C and H atoms of the C-H bond. In the actual calculations, $(\partial\mu/\partial r)^2$ was assumed to be a constant. We note that different correction methods[60] for the classical results will yield different prefactors in Equation (6.5).

We also performed DFT calculations of C-H vibrations for the same ten configurations we employed above as initial configurations for the velocity auto-correlation calculations. Specifically, ion pairs were first identified as a cation plus its pairing

anion that is situated closest to the H atom of the cation's CH group under consideration for each configuration. For each of the ion pairs thus identified, *ab initio* calculations were performed with surrounding ions treated as a classical charge distribution in the QM/MM framework.[43] In the analysis of vibrational frequencies via PHVA (partial Hessian vibrational analysis),[44] the actual masses were used for C and H of the C-H bond under consideration, while all other atoms were assumed to be infinite in mass (9.0×10^6 amu to be exact). Therefore the QM/MM results we obtained describe frequencies of local C-H vibrational modes. All *ab initio* calculations were carried out using Gaussian 09 package[61] with the internally stored 6-31G(d, p) basis set. The hybrid B3LYP functional[62] was employed to optimize geometry of the H atom of the CH groups under consideration while all other atoms were frozen at the MD geometry. We note that the QM/MM method similar to ours was applied to study chemical shifts of BMI^+-based ILs.[63] Though only one MD configuration was employed in the analysis there, a good agreement with NMR measurements was obtained.

6.3 Results and Discussion

MD results for average IL densities are presented in Table 6.1. Good accord with the experimental results indicates that both OPLS-AA and CHARMM force fields provide a reasonable theoretical description for BMI^+-based IL systems. With this in mind, we consider their results for IL structure.

Table 6.1: MD results for IL densities (units: g/cm^3)

IL	CHARMM	OPLS-AA	Experiments
BMI^+Cl^-	1.034	1.063	1.053[a]
BMI^+Br^-	1.258	1.274	1.27[b]
$BMI^+BF_4^-$	1.145	1.143	1.161[c]

[a] Ref. 64. T =353 K.
[b] Refs. 65 and 66, estimated.
[c] Ref. 67. T = 352 K.

6.3.1 Structure

MD results for radial distribution functions (RDFs) of anions X^- around H atoms of the BMI^+ ring obtained with the OPLS-AA and CHARMM force fields are displayed in Figure 6.2. In the case of BF_4^-, RDFs of its F sites around H are exhibited. We consider the OPLS-AA results in Figure 6.2 first. Since the Lennard-Jones (LJ) interaction parameters and partial charges are identical for H11, H12 and H13 and nearly identical for C2, C4 and C5 in the OPLS-AA description (Tables S8 and S9),[51,52] the positions of the first RDF peaks of X^- around H11, H12 and H13 are virtually the same (Table 6.2). In addition, their peak heights are comparable. As such, the acidic character of H11 is not captured in the IL structure determined with the OPLS-based model description. We notice that the main peak height of the anion distributions around the ring hydrogen atoms decreases as the anion size increases. Furthermore, the number of X^- in the first solvation shell of H11 is bigger in BMI^+Br^- than in BMI^+Cl^- (Table 6.3). This indicates that ion pairing, *i.e.*, ability to form 1-1 cation-anion complex, becomes weaker in the order $Cl^- > Br^- > BF_4^-$.

Table 6.2: Height and position of the first RDF peak of anions[a] around H11 and H12[b]

IL	CHARMM	OPLS-AA
BMI^+Cl^-	12.5, 2.20 Å (5.7, 2.42 Å)	6.6, 2.58 Å (6.1, 2.60 Å)
BMI^+Br^-	10.2, 2.36 Å (5.0, 2.58 Å)	5.6, 2.74 Å (5.4, 2.72 Å)
$BMI^+BF_4^-$	3.3, 2.06 Å (2.3, 2.30 Å)	2.6, 2.54 Å (2.2, 2.48 Å)

[a] For $BMI^+BF_4^-$, the results for F are presented.

[b] Results for H12 are given in parentheses.

In contrast to the OPLS-AA description, CHARMM force field yields a significant difference in anion RDF between the acidic H11 and the non-acidic H12 and H13. The anion distributions are tighter and more pronounced around H11 than around H12 or H13 (Figure 6.2 and Table 6.2). As a result, the number of X^- in the first solvation shell of H11 is smaller than that of H12 in Table 6.3 since the volume of the solvation

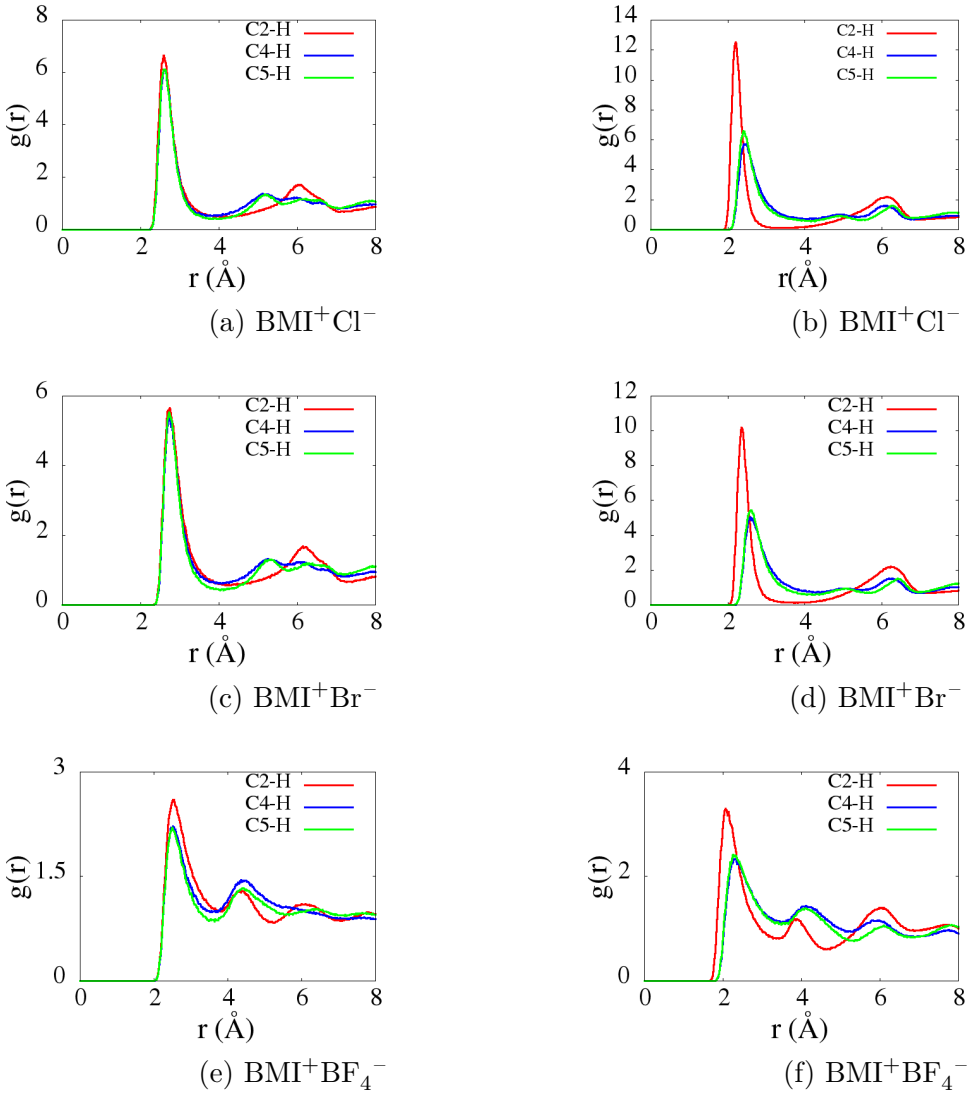

(a) BMI^+Cl^- (b) BMI^+Cl^-

(c) BMI^+Br^- (d) BMI^+Br^-

(e) $BMI^+BF_4^-$ (f) $BMI^+BF_4^-$

OPLS-AA CHARMM

Figure 6.2: Radial distribution functions of anions around hydrogen atoms of the BMI^+ ring obtained with OPLS-AA force field (left): (a) BMI^+Cl^-, (c) BMI^+Br^- and (e) $BMI^+BF_4^-$; and CHARMM force field (right): (b) BMI^+Cl^-, (d) BMI^+Br^- and (f) $BMI^+BF_4^-$. The results for H11, H12 and H13 are plotted in red, green and blue, respectively. For BF_4^-, F atoms are employed in the calculations of RDF.

Table 6.3: Number of anions[a] in the first solvation shell of H11 and of H12[b]

IL	CHARMM	OPLS-AA
BMI^+Cl^-	1.03 (1.51)	1.34 (1.13)
BMI^+Br^-	1.04 (1.63)	1.50 (1.25)
$BMI^+BF_4^-$	2.46 (2.93)	3.43 (2.43)

[a] Number of F atoms in the case of $BMI^+BF_4^-$.

[b] Results for H12 are given in parentheses.

shell of H12 is considerably larger than that of H11. This is exactly the opposite of the OPLS-AA results also presented there. Differing non-bonding interaction parameters of the BMI^+ ring atoms are responsible for the marked differences in RDF between H11 and H12/H13 in the CHARMM force field results. To be specific, the value of the LJ σ parameter for H11 (1.2 Å) is smaller than that for H12 (and H13) (1.6 Å) (Table C.2) and as a consequence, anions can approach the former better than the latter. In addition, the partial charges of H11 (0.153e) and C2 (0.333e) are greater than the corresponding charges of H12 and H13 (0.126e) and C4 and C5 (0.199e). This also helps the C2-H11 group to attract anions better than the C4-H12 or C5-H13 group. Analogous to the OPLS-AA case, the interactions of the anion and the ring H atoms, gauged by their RDF peak heights, and the ion pairing capability, measured by the number of anions in the first solvation shell, become weaker as the anion size increases.

According to prior DFT studies of ion pair interactions in the gas phase, H11 of imidazolium exhibits a hydrogen-bonded interaction[68,69] with anions to a varying degree.[23–25] Comparison of the results for different anions[23–25] indicates that the strength of this interionic hydrogen-bonded interaction increases with the hydrogen-bond accepting power, *i*.e., basicity, of the anions. In this context, the large amplitude of the main peak in the anion RDF around H11 and the significant inward shift of its position compared to the corresponding peaks around H12 and H13 in Figure 6.2

should be considered as the formation of a general hydrogen bond between C2-H11 and X^-. The decrease in the first peak height of the H11$\cdots X^-$ RDF is interpreted as the weakening of the H11$\cdots X^-$ interionic hydrogen bond in the order $Cl^- > Br^- > BF_4^-$.

6.3.2 Vibrational spectra (MD)

We proceed to vibrational spectra of the C-H groups of the cation ring determined from MD. The results obtained with the OPLS-AA and CHARMM force fields using Equation (6.5) are displayed in Figure 6.3. We start with the vibrational spectra of isolated BMI^+ in vacuum. The peak positions for the ring C-H stretching vibrations are around 2950 cm^{-1} in Figure 6.3a. Because all three C-H bonds are characterized by the same force constant 2.845×10^5 kJ/mol/nm^2 (Table C.10), their vibrational frequencies are essentially the same in the OPLS-AA description. By contrast, the force constant for C2-H11 vibrations (2.787×10^5 kJ/mol/nm^2) is smaller than that for C4-H12 and C5-H13 vibrations (3.138×10^5 kJ/mol/nm^2) in the CHARMM force field (Table C.4). As a result, the main peak for the former is located at a considerably lower frequency 3070 cm^{-1} than those for the latter two at $\sim$ 3190 cm^{-1} in Figure 6.3b. In both OPLS-AA and CHARMM force field descriptions, C4-H12 and C5-H13 vibrations exhibit a doublet structure, arising from their two normal modes, *viz.*, symmetric and antisymmetric stretching vibrations of C4-H12 and C5-H13.

One noteworthy feature of the OPLS-AA results is the presence of a very minor structure around 3010 cm^{-1} in the C2-H11 spectrum (Figure 6.3a). This is due to the mixing of C-H vibrations of alkyl chains of BMI^+ into the local C2-H11 vibrational mode. According to our simulations (results not shown), the vibrational frequencies of the C-H groups of the alkyl chains range from $\sim$2800 cm^{-1} to $\sim$3000 cm^{-1}.

For perspective, we mention that the DFT predictions for the vibrational frequencies of an isolated BMI^+ cation are about 3300 cm^{-1} for all ring C-H bonds. This is

at variance with the MD results for vibrational spectra in vacuum in Figure 6.3a and Figure 6.3b. However, the force field parameters are designed to describe liquid state properties, and therefore their gas-phase results should not be taken too seriously. The main purpose of the gas-phase MD analysis here is to gain insight that will help to understand liquid-phase results, which we turn to next.

In the computational spectra determined with OPLS-AA force field, the C2-H11 stretching vibrations develop a distinct double peak structure in all three ILs we studied (Figs. 6.3c, 6.3e, and 6.3g). The peak positions of the doublet are $\sim$2970 cm^{-1} and $\sim$3030 cm^{-1}. The enhancement of the doublet structure compared to isolated BMI$^+$ in Figure 6.3a is attributed to the increase in coupling between C2-H11 vibrations and C-H vibrations of the alkyl chain through, for example, sharing of a common anion between the two groups and the resulting increase in the mixing of the two vibrational modes. The C2-H11, C4-H12 and C5-H13 bands all become broadened and slightly blue-shifted in the IL phase, compared to the corresponding bands of isolated BMI$^+$ (see below).

In the case of CHARMM, the C2-H11 vibrational band exhibits three distinctive features, *viz.*, a main peak at $\sim$3100 cm^{-1} with a shoulder structure on its red edge near 3080 cm^{-1} and a weak secondary peak on its blue edge around 3150 cm^{-1} in the liquid phase (Figs. 6.3d, 6.3f, and 6.3h). The position of the shoulder structure is very close to the C2-H11 frequency of isolated BMI$^+$, *i.e.*, 3070 cm^{-1}, and it is assigned to vibrations of C2-H11 bonds that are not hydrogen-bonded. A simple analysis based on the H11$\cdots$X$^-$ separation[27,70] indicates that about 29% of C2-H11 bonds are not hydrogen-bonded in BMI$^+$Cl$^-$ at 350 K. The two peaks at $\sim$3100 and $\sim$3150 cm^{-1}, on the other hand, are assigned to vibrations of hydrogen-bonded C2-H11. The blue-shift of these two peaks with respect to isolated BMI$^+$ in vacuum is mainly ascribed to short-range LJ interactions between H11 and X$^-$ of the hydrogen-bonded pair. Specifically, the presence of an anion close to a C-H bond in solution

makes its C-H vibrational potential stiffer through short-range repulsion of H and thus raises its vibrational frequency over the gas-phase value. Though not presented here, we mention that the C2-H11 bond of a BMI^+–X^- ion pair in vacuum shows three vibrational peaks, the frequencies of which are very close to the three frequencies observed in the liquid-phase.

There are several features shared by the OPLS-AA and CHARMM results in Figure 6.3. First, compared to the gas phase, the vibrational spectra become broadened in the liquid phase as they should (inhomogeneous broadening). Second, the solution-phase spectra show a blue shift with respect to the gas phase. Third, as the anion size decreases and its basicity increases, the C2-H11 band becomes blue-shifted. The OPLS-AA results for the main peak position of the band are $\sim$2980, 2974 and 2970 cm^{-1} for BMI^+Cl^-, BMI^+Br^- and $BMI^+BF_4^-$, respectively, while the corresponding CHRMM results are $\sim$3140, 3100 and 3090 cm^{-1}. The extent of the blue-shift is larger in the CHARMM description than in the OPLS-AA description. This difference arises primarily from the formation of a hydrogen-bond between H11 and X^- in the former description. This hydrogen-bond formation shortens the distance between H11 and X^- and as a result, it strengthens the aforementioned short-range repulsion of the two and enhances the blue-shift of C2-H11 vibrations, compared to OPLS-AA. The second and third features noted here, which are at variance with experiments,[21] are spurious results arising from the harmonic approximation with fixed force constants, employed for stretching vibrations of chemical bonds in the force-field approach. We will return to this issue below. Due to errors in the force field parameters employed in ref. 71, the present MD analysis of C-H vibrational structures in the liquid phase supersedes the earlier work presented there.

6.3.3 Vibrational spectra (QM/MM)

Finally, we turn to QM/MM results for CH vibrational spectra in the liquid IL phase. The DFT results for distributions of CH stretching frequencies in the pres-

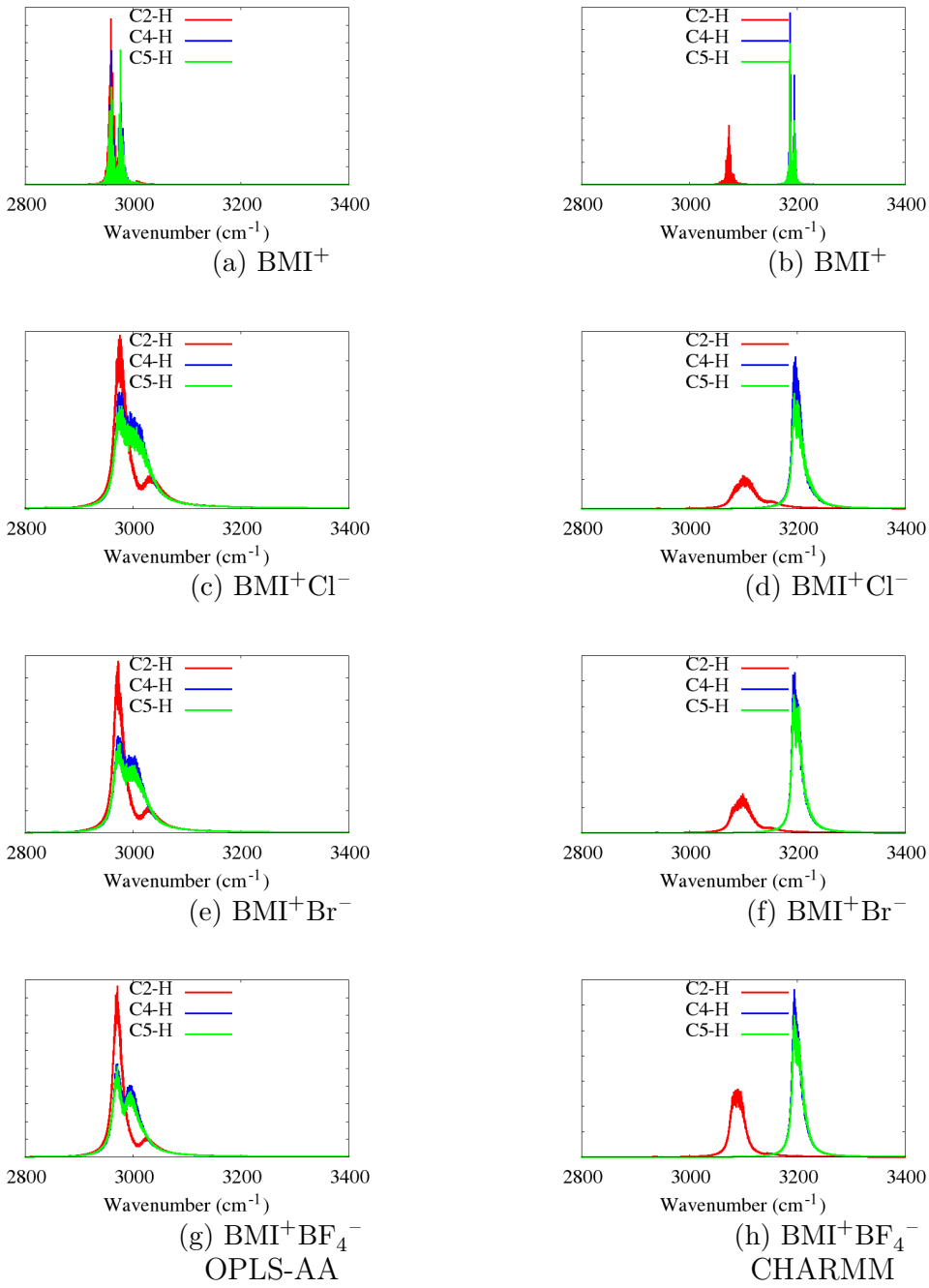

(a) BMI^+ (b) BMI^+

(c) BMI^+Cl^- (d) BMI^+Cl^-

(e) BMI^+Br^- (f) BMI^+Br^-

(g) $BMI^+BF_4^-$ OPLS-AA (h) $BMI^+BF_4^-$ CHARMM

Figure 6.3: Vibrations of ring CH bonds using OPLS-AA (left): (a) isolated BMI^+, (c) BMI^+Cl^-, (e) BMI^+Br^-, (g) $BMI^+BF_4^-$; and CHARMM (right) force fields: (b) isolated BMI^+, (d) BMI^+Cl^-, (f) BMI^+Br^-, (h) $BMI^+BF_4^-$.

ence of the IL configurations obtained from classical MD with the OPLS-AA and CHARMM force fields are shown in Figure 6.4. One of the most salient features is that MD/DFT predictions for the spectral shift of the C2-H11 vibrational band with IL anionic species are exactly the opposite of the corresponding classical results in Figure 6.3. The MD/DFT results show an increasing red-shift as the anion becomes more basic, whereas the force-field results exhibit a growing blue shift. The red-shift in the former arises from the weakening of the C2-H11 bond, caused mainly by the H11$\cdots$X$^-$ interionic hydrogen-bonded interaction.[23–26] As the basicity and thus hydrogen-bond accepting power of X$^-$ increases, the H11$\cdots$X$^-$ hydrogen bond strengthens by withdrawing electron density from the C2-H11 bond increasingly more. This in turn weakens the C2-H11 bond and decreases its vibrational frequency. The MD/DFT results for the position of the C2-H11 band, defined as the vibrational frequency averaged over its distribution, are 2840, 2863 and 3084 cm^{-1} for BMI$^+$Cl$^-$, BMI$^+$Br$^-$ and BMI$^+$BF$_4^-$, respectively, with the IL configurations determined with CHARMM (Figure 6.4). The corresponding results with the OPLS-AA configurations of ILs are 2940, 3000 and 3100 cm^{-1} (Figure 6.4). (For comparison, the DFT predictions for the C2-H11 vibrational frequency for the BMI$^+$–X$^-$ ion pair in the lowest energy conformation in the gas phase are 2589, 2628 and 3276 cm^{-1} for X$^-$ = Cl$^-$, Br$^-$ and BF$_4^-$, respectively, while that for isolated BMI$^+$ is 3302 cm^{-1}.) These results are in good agreement with the corresponding experimental values, 3018, 3020 and 3114 cm^{-1}, obtained in recent IR study by Kim, Ouchi and their co-workers.[21] Thus MD/DFT in the QM/MM framework predicts correctly that the red shift of the C2-H11 vibrational frequency correlates with the basicity of the hydrogen-bond accepting anions, *i*.e., hydrogen bond strength, in bulk ILs. Our analysis here also exposes the limitations of the vibrational analysis based on the classical force field, in which modulations of the molecular bond strength induced by electron density rearrangement are completely missing due to the harmonic approximation with fixed

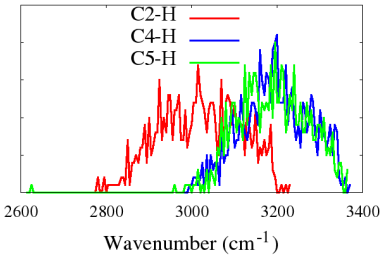

(a) BMI^+Cl^-

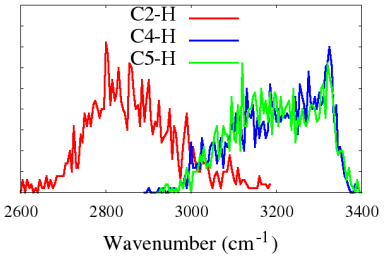

(b) BMI^+Cl^-

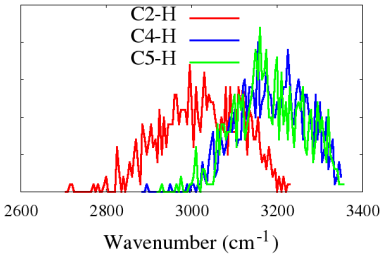

(c) BMI^+Br^-

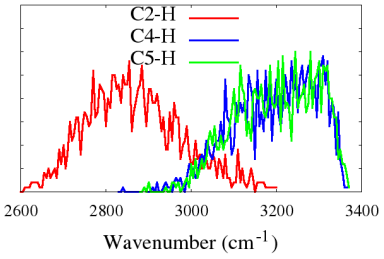

(d) BMI^+Br^-

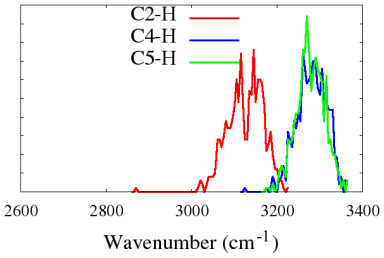

(e) $BMI^+BF_4^-$

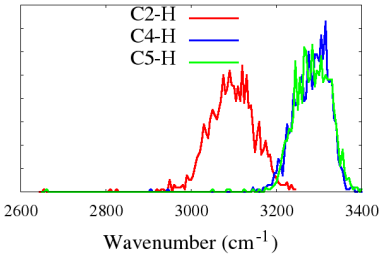

(f) $BMI^+BF_4^-$

OPLS-AA CHARMM

Figure 6.4: *Ab initio* results for CH vibrations using MD configurations obtained with OPLS-AA force fields (left): (a) BMI^+Cl^-, (c) BMI^+Br^-, (e) $BMI^+BF_4^-$; and CHARMM force fields (right): (b) BMI^+Cl^-, (d) BMI^+Br^-, (f) $BMI^+BF_4^-$.

force constants.

Another noteworthy aspect of Figure 6.4 is that the ring C-H vibrational bands of BMI^+Cl^- and BMI^+Br^- are considerably broader than those of $BMI^+BF_4^-$. This difference is ascribed to two factors, *viz.*, the strength and directionality of interactions between X^- and H. First, because the interactions of ring hydrogen atoms with Cl^- or Br^- are stronger than those with the F atoms of BF_4^-, structural fluctuations of the former anions will modulate significantly more the $H\cdots X^-$ interactions and thus C-H vibrational frequencies than those of the latter. Everything being equal, this

will yield an enhanced broadening of the C-H vibrational bands in the presence of Cl^- or Br^-, compared to BF_4^-. Second, the relative orientation of X^- with respect to the C-H bond is characterized by a wider distribution for atomic ions Cl^- or Br^- than for bulky BF_4^- with multiple F sites. As a result, the directionality of $H\cdots X^-$ interaction and therefore its strength vary much more with X = Cl and Br than with F of BF_4^-. This also results in an increase in the linewidth of C-H vibrational bands in the presence of Cl^- or Br^-, compared to BF_4^-. Our results are in good qualitative agreement with the deconvoluted IR spectra in ref. 21 though the spectral linewidths were not analyzed there.

It is worthy of note that while the intermolecular hydrogen-bonded structure of H11 is not captured appropriately in MD configurations determined with OPLS-AA force field as discussed above (Figure 6.2), DFT calculations of C2-H11 stretching vibrations based on these configurations, nonetheless, yield correct attributes of hydrogen-bonded interactions of H11 (Figure 6.4). This is because the electronic structure change of the C2-H11 bond induced by the presence of an anion in the vicinity is different from that of C4-H12 or C5-H13. In BMI^+Cl^-, the C2-H11 bond length of ion pairs averaged over 10 different MD configurations obtained with OPLS-AA force field (Sec. 6.2) is 1.804 Å prior to DFT optimization, whereas the corresponding QM/MM result is 1.806 Å. This means that compared to the MD result with OPLS-AA, the C2-H11 bond becomes slightly elongated when it is treated quantum mechanically via MD/DFT. By contrast, the average C4-H12 bond length in BMI^+Cl^- decreases from 1.807 to 1.803 Å with DFT optimization. In BMI^+Br^-, the C2-H11 bond length remains unchanged with the QM/MM procedure, while the C4-H12 bond length decreases by 0.005 Å. This shows that a proper account of the chemical nature, *i.e.*, electronic aspect, of the bonds is critical to an accurate understanding of their

vibrational structures.

6.4 Conclusions

In this article, we have studied vibrational spectra of ring hydrogen atoms of BMI^+-based ionic liquids using two different approaches: (i) classical MD with different force fields and (ii) DFT using the MD results for liquid structures in the QM/MM framework. It was found that while the hydrogen bond structure of acidic H11 was properly captured with CHARMM force field, its results for C2-H11 vibrational spectra showed a large departure from experiments. The OPLS-AA force field led to a similar deviation for C2-H11 vibrations but to a lesser degree. However, the hydrogen-bonded structure of H11 is largely missing in the OPLS-AA results because its acidic character is not reflected in its force field parameterization. QM/MM results obtained with MD configurations for IL structure, on the other hand, correctly predicts that C2-H11 vibrations shift to lower frequencies as the basicity of the hydrogen-bond accepting anions increases, in good accord with experiments.[21] They also yield narrowing of the C-H vibrational bands of the imidazolium ring in $BMI^+BF_4^-$ with respect to those in BMI^+Cl^- or BMI^+Br^-, consonant with experimental spectra. The failure of the force field approach to molecular vibrations in liquids is due to the classical harmonic approximation that completely neglects the weakening of the vibrational force constant, engendered by interionic hydrogen-bonded interactions. Therefore, electronic structure variations of C-H bonds, modulated by the local solvation environment, are crucial to an accurate account of their vibrational spectra.

[1] Welton, T. *Chem. Rev.* **1999**, *99*, 2071–2084.

[2] Wassercheid, P.; W., K. *Angew. Chem. Int. Ed.* **2000**, *39*, 3772–3789.

[3] Seddon, K. R. *J. Chem. Technol. Biotechno.* **1997**, *68*, 351–356.

[4] Hagiwara, R.; Ito, Y. *J. Fluorine Chem.* **2000**, *105*, 221–227.

[5] Huddleston, J. G.; Willauer, H. W.; Swatloski, R. P.; Visser, A. E.; Rogers, R. D. Room temperature ionic liquids as novel media for clean liquid liquid extraction. *Chem. Common.* **1998**, 1765–1766.

[6] Dieter, K. M.; Dymek, J., C. J.; Heimer, N. E.; Rovang, J. W.; Wilkes, J. S. *J. Am. Chem. Soc.* **1998**, *110*, 2722–2726.

[7] Talaty, E. R.; Raja, S.; Storhaug, V. J.; Dolle, A.; Carper, W. R. Raman and Infrared Spectra and ab Initio Calculations of C2-4MIM Imidazolium Hexafluorophosphate Ionic Liquids. *J. Phys. Chem. B* **2004**, *108*, 13177–13184.

[8] Heimer, N. E.; del Sesto, R. E.; Meng, Z.; Wilkes, J. S.; Carper, W. R. Vibrational spectra of imidazolium tetrafluoroborate ionic liquids. *J. Mol. Liq.* **2006**, *124*, 84–95.

[9] Rivera-Rubero, S.; Baldelli, S. *J. Phys. Chem. B* **2006**, *110*, 4756–4765.

[10] Palomar, J.; Ferro, V. R.; Gilarranz, M. A.; Rodriguez, J. J. Computational Approach to Nuclear Magnetic Resonance in 1-Alkyl-3-methylimidazolium Ionic Liquids. *J. Phys. Chem. B* **2007**, *111*, 168–180.

[11] Yokozeki, A.; Kasprzak, D. J.; Shiflett, M. B. *Phys. Chem. Chem. Phys.* **2007**, *36*, 5018–5026.

[12] Köddermann, T.; Wertz, C.; Heintz, A.; Ludwig, R. Ion-Pair Formation in the Ionic Liquid 1-Ethyl-3-methylimidazolium Bis(triflyl)imide as a Function of Temperature and Concentration. *Chem.Phys.Chem.* **2006**, *7*, 1944–1949.

[13] Fumino, K.; Wulf, A.; Ludwig, R. The Cation–Anion Interaction in Ionic Liquids Probed by Far-Infrared Spectroscopy. *Angew. Chem., Int. Ed.* **2008**, *47*, 3830–3834.

[14] Wulf, A.; Fumino, K.; Ludwig, R.; Taday, P. Combined THz, FIR and Raman Spectroscopy Studies of Imidazolium-Based Ionic Liquids Covering the Frequency Range 2—300 cm^{-1}. *Chem. Phys. Chem.* **2010**, *11*, 349–353.

[15] Katsyuba, S. A.; Zvereva, E. E.; Vidiš, A.; Dyson, P. J. *J. Phys. Chem. A* **2007**, *111*, 352–370.

[16] Tsuzuki, S.; Tokuda, H.; Mikami, M. *Phys. Chem. Chem. Phys.* **2007**, *9*, 4780–4784.

[17] Kiefer, J.; Fries, J.; Leipertz, A. *Appl. Spectrosc* **2007**, *61*, 1306–1311.

[18] Noack, K.; Schulz, P. S.; Paape, N.; Kiefer, J.; Wasserscheid, P.; Leipertz, A. *Phys. Chem. Chem. Phys.* **2010**, *12*, 14153–14161.

[19] Hunt, P. A. Why Does a Reduction in Hydrogen Bonding Lead to an Increase in Viscosity for the 1-Butyl-2,3-dimethyl-imidazolium-Based Ionic Liquids? *J. Phys. Chem. B* **2007**, *111*, 4844–4853.

[20] Jeon, Y.; Sung, J.; Seo, C.; Lim, H.; Cheong, H.; Kang, M.; Moon, B.; Ouchi, Y.; Kim, D. *J. Phys. Chem. B* **2008**, *112*, 4735–4740.

[21] Cha, S.; Ao, M.; Sung, W.; Moon, B.; Ahlstrom, B.; Johansson, P.; Ouchi, Y.; Kim, D. Structures of ionic liquid-water mixtures investigated by IR and NMR spectroscopy. *Phys. Chem. Chem. Phys.* **2014**, *16*, 9591–9601.

[22] Seki, T.; Grunwaldt, J.-D.; Baiker, A. *J. Phys. Chem. B* **2009**, *113*, 114–122.

[23] Dhumal, N. R. *Chem. Phys.* **2007**, *342*, 245–252.

[24] Dhumal, N. R.; Kim, H. J.; Kiefer, J. *J. Phys. Chem. A* **2009**, *113*, 10397–10404.

[25] Dhumal, N. R.; Kim, H. J.; Kiefer, J. *J. Phys. Chem. A* **2011**, *115*, 3551–3558.

[26] Dhumal, N. R.; Noack, K.; Kiefer, J.; Kim, H. J. *J. Phys. Chem. A* **2014**, *118*, 2547–2557.

[27] Bursulaya, B. D.; Kim, H. J. A Molecular Dynamics Simulation Study of Water near Critical Conditions. II. Dynamics and Spectroscopy. *J. Chem. Phys.* **1999**, *110*, 9656–9665.

[28] Joseph, J.; Jemmis, E. D. *J. Am. Chem. Soc.* **2007**, *129*, 4620–4632.

[29] Schrekker, H. S.; Silva, D. O.; Gelesky, M. A.; Stracke, M. P.; Schrekker, C. M. L.; Goncalves, R. S.; Dupont, J. *J. Braz. Chem. Soc.* **2008**, *19*, 426–433.

[30] Umebayashi, Y.; Hamano, H.; Tsuzuki, S.; Canongia Lopes, J. N.; Padua, A. A. H.; Kameda, Y.; Kohara, S.; Yamaguchi, T.; Fujii, K.; Ishiguro, S. Dependence of the Conformational Isomerism in 1-n-Butyl-3-methylimidazolium Ionic Liquids on the Nature of the Halide Anion. *J. Phys. Chem. B* **2010**, *114*, 11715–11724.

[31] Migliorati, V.; Zitolo, A.; Dangelo, P. Using a Combined Theoretical and Experimental Approach to Understand the Structure and Dynamics of Imidazolium-Based Ionic Liquids/Water Mixtures. 1. MD Simulations. *J. Phys. Chem. B* **2013**, *117*, 12505–12515.

[32] Migliorati, V.; Serva, A.; Aquilanti, G.; Olivi, L.; Pascarelli, S.; Mathonc, O.; D'Angelo, P. Combining EXAFS spectroscopy and molecular dynamics simulations to understand the structural and dynamic properties of an imidazolium iodide ionic liquid. *Phys. Chem. Chem. Phys.* **2015**, *17*, 2464–2474.

[33] Migliorati, V.; Serva, A.; Aquilanti, G.; Pascarellic, S.; D'Angelo, P. Local order and long range correlations in imidazolium halide ionic liquids: a combined molecular dynamics and XAS study. *Phys. Chem. Chem. Phys.* **2015**, *17*, 16443–16453.

[34] See, *e.g.*, N. R. Dhumal, J. Kiefer, D. Turton, K. Wynne and H. J. Kim, *J. Phys. Chem. B*, 2017, **121**, 4845–4851 and references therein.

[35] Youngs, T. G. A.; Hardacre, C. Application of Static Charge Transfer within an Ionic-Liquid Force Field and Its Effect on Structure and Dynamics. *Chem. Phys. Chem.* **2008**, *9*, 1548–1558.

[36] Kohagen, M.; Brehm, M.; Lingscheid, Y.; Giernoth, R.; Sangoro, J.; Kremer, F.; Naumov, S.; Iacob, C.; Karger, J.; Valiullin, R.; Kirchner, B. How Hydrogen Bonds Influence the Mobility of Imidazolium-Based Ionic Liquids. A Combined Theoretical and Experimental Study of 1-n-Butyl-3-methylimidazolium Bromide. *J. Phys. Chem. B* **2011**, *115*, 15280–15288.

[37] Kohagen, M.; Brehm, M.; Thar, J.; Zhao, W.; Maller-Plathe, F.; Kirchner, B. Performance of Quantum Chemically Derived Charges and Persistence of Ion Cages in Ionic Liquids. A Molecular Dynamics Simulations Study of 1-n-Butyl-3-methylimidazolium Bromide. *J. Phys. Chem. B* **2011**, *115*, 693–702.

[38] Del Pópolo, M. G.; Lynden-Bell, R. M.; Kohanoff, J. Ab Initio Molecular Dynamics Simulation of a Room Temperature Ionic Liquid. *J. Phys. Chem. B* **2005**, *109*, 5895–5902, PMID: 16851642.

[39] Bhargava, B. L.; Balasubramanian, S. *Chem. Phys. Lett.* **2006**, *417*, 486–491.

[40] Bodo, E.; Sferrazza, A.; Caminiti, R.; Mangialardo, S.; Postorino, P. A prototypical ionic liquid explored by ab initio molecular dynamics and Raman spectroscopy. *J. Chem. Phys.* **2013**, *139*, 144309.

[41] Thomas, M.; Brehm, M.; Hollóczki, O.; Kelemen, Z.; Nyulászi, L.; Pasinszki, T.; Kirchner, B. Simulating the vibrational spectra of ionic liquid systems: 1-Ethyl-3-methylimidazolium acetate and its mixtures. *J. Chem. Phys.* **2014**, *141*, 024510.

[42] Tanzi, L.; Benassi, P.; Nardone, M.; Ramondo, F. Vibrations of Bioionic Liquids by Ab Initio Molecular Dynamics and Vibrational Spectroscopy. *J. Phys. Chem. A* **2014**, *118*, 12229–12240.

[43] See, *e.g.*, *Combined Quantum Mechanical and Molecular Mechanical Methods*, edited by J. Gao and M. A. Thompson, ACS Symp. Ser. 712 (ACS, Washington, D.C., 1998).

[44] Li, H.; Jensen, J. H. *Theor. Chem. Acc.* **2002**, *107*, 211–219.

[45] Speranskiy, K.; Kurnikova, M. *J. Chem. Phys.* **2004**, *121*, 1516–1524.

[46] Pronk, S.; Páll, S.; Schulz, R.; Larsson, P.; Bjelkmar, P.; Apostolov, R.; Shirts, M. R.; Smith, J. C.; Kasson, P. M.; van der Spoel, D.; Hess, B.; Lindahl, E. GROMACS 4.5: a high-throughput and highly parallel open source molecular simulation toolkit. *Bioinformatics* **2013**, *29*, 845–854.

[47] Jorgensen, W. L.; Maxwell, D. S.; Tirado-Rives, J. *J. Am. Chem. Soc.* **1996**, *118*, 11225–11236.

[48] Kaminski, G. A.; Friesner, R. A.; Tirado-Rives, J.; Jorgensen, W. L. *J. Phys. Chem. B* **2001**, *105*, 6474–6487.

[49] MacKerell, A. D. et al. All-Atom Empirical Potential for Molecular Modeling and Dynamics Studies of Proteins. *J. Phys. Chem. B* **1998**, *102*, 3586–3616, PMID: 24889800.

[50] Mackerell, A. D.; Feig, M.; Brooks, C. L. Extending the treatment of backbone energetics in protein force fields: Limitations of gas-phase quantum mechanics in reproducing protein conformational distributions in molecular dynamics simulations. *J Comp. Chem. 25*, 1400–1415.

[51] Lopes, J. N. C.; Deschamps, J.; Pádua, A. A. H. *J. Phys. Chem. B* **2004**, *108*, 2038–2047.

[52] Lopes, J. N. C.; Deschamps, J.; Pádua, A. A. H. *J. Phys. Chem. B* **2004**, *108*, 11250–11250.

[53] https://www.paramchem.org.

[54] Vanommeslaeghe, K.; Hatcher, E.; Acharya, C.; Kundu, S.; Zhong, S.; Shim, J.; Darian, E.; Guvench, O.; Lopes, P.; Vorobyov, I.; MacKerell Jr., A. D. *J. Comput. Chem.* **2010**, *31*, 671–690.

[55] Vanommeslaeghe, K.; MacKerell Jr., A. D. *J. Chem. Inf. Model.* **2012**, *52*, 3144–3154.

[56] Vanommeslaeghe, K.; Raman, E. P.; MacKerell Jr., A. D. *J. Chem. Inf. Model.* **2012**, *52*, 3155–3168.

[57] Canongia Lopes, J. N.; Pádua, A. A. H. Molecular Force Field for Ionic Liquids III: Imidazolium, Pyridinium, and Phosphonium Cations; Chloride, Bromide, and Dicyanamide Anions. *J. Phys. Chem. B* **2006**, *110*, 19586–19592.

[58] Darden, T.; York, D.; Pedersen, L. Particle mesh Ewald: An N log(N) method for Ewald sums in large systems. *J. Chem. Phys.* **1993**, *98*, 10089–10092.

[59] McQuarrie, D. A. *Statistical Mechanics*; HarperCollins, 1976.

[60] See, *e.g.*, B. D. Bursulaya and H. J. Kim, *J. Chem. Phys.*, 1998, **109**, 4911–4919 and references therein.

[61] Frisch, M. J. et al. Gaussian 09 Revision A.02. Gaussian Inc. Wallingford CT 2009.

[62] Becke, A. D. *J. Chem. Phys.* **1993**, *98*, 5648–5652.

[63] Bagno, A.; D'Amico, F.; Saielli, G. Computing the NMR Spectrum of a Bulk Ionic Liquid Phase by QM/MM Methods. *J. Phys. Chem. B* **2006**, *110*, 23004–23006, PMID: 17107137.

[64] Machida, H.; Taguchi, R.; Sato, Y.; Smith, R. L., Jr. Measurement and Correlation of High Pressure Densities of Ionic Liquids, 1-Ethyl-3-methylimidazolium l-Lactate ([emim][Lactate]), 2-Hydroxyethyl-trimethylammonium l-Lactate ([(C2H4OH)(CH3)3N][Lactate]), and 1-Butyl-3-methylimidazolium Chloride ([bmim][Cl]). *Journal of Chemical & Engineering Data* **2011**, *56*, 923–928.

[65] Kim, K.-S.; Shin, B.-K.; Lee, H. Physical and electrochemical properties of 1-butyl-3-methylimidazolium bromide, 1-butyl-3-methylimidazolium iodide, and 1-butyl-3-methylimidazolium tetrafluoroborate. *Korean Journal of Chemical Engineering* **2004**, *21*, 1010–1014.

[66] Tshibangu, P. N.; Ndwandwe, S. N.; Dikio, E. D. Density, Viscosity and Conductivity Study of 1-Butyl-3-Methylimidazolium Bromide. *International Journal of Electrochemical Science* **2011**, *6*, 2201–2213.

[67] Jacquemin, J.; Husson, P.; Padua, A. A. H.; Majer, V. Density and viscosity of several pure and water-saturated ionic liquids. *Green Chem.* **2006**, *8*, 172–180.

[68] Koch, U.; Popelier, P. L. A. Characterization of C-H-O Hydrogen Bonds on the Basis of the Charge Density. *J. Phys. Chem.* **1995**, *99*, 9747–9754.

[69] Popelier, P. L. A. Characterization of a Dihydrogen Bond on the Basis of the Electron Density. *J. Phys. Chem. A* **1998**, *102*, 1873–1878.

[70] Willcox, J. A. L.; Kim, H.; Kim, H. J. A molecular dynamics study of the ionic liquid, choline acetate. *Phys. Chem. Chem. Phys.* **2016**, *18*, 14850–14858.

[71] Kim, H.; Dhumal, N. R.; Shim, Y.; Kim, H. J. Computational Study of Structure, Dynamics and Spectroscopy of Ionic Liquids. *ECS Trans.* **2014**, *64*, 119–127.

Appendices

Theoretical Study of Alkylsulfonic Acids: Force Field Development and Molecular Dynamics Simulations

A.1 RDF

Figure A.1 shows RDFs of O_H-C_M and C_M-C_M.

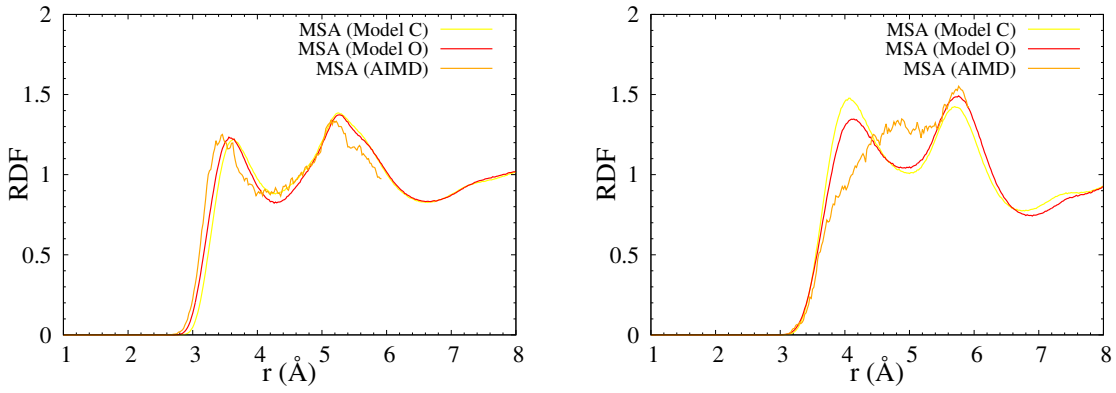

(a) O_H-C_M (b) C_M-C_M

Figure A.1: RDFs of O_H-C_{S1} and C_{S1}-C_{S1} in MSA.

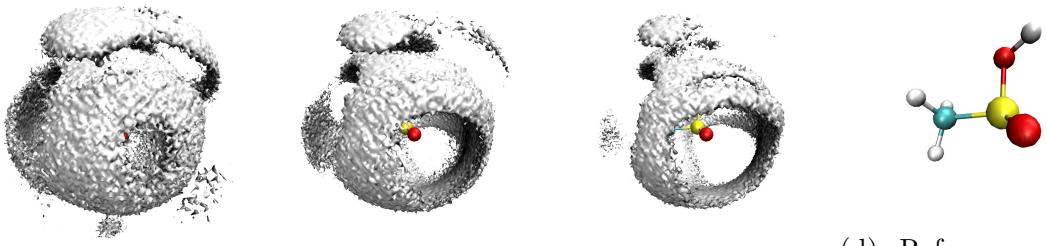

(a) isosurface 2 (b) isosurface 2.5 (c) isosurface 3 (d) Reference structure

Figure A.2: Model C results for SDF of C_{S1} around S_O in MSA at isosurface values of (a) 2, (b) 2.5 and (c) 3. For clarity, spatial orientation of the central MSA molecule is shown in (d).

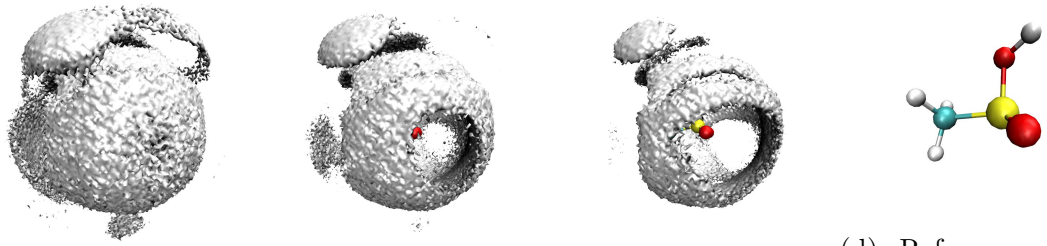

(a) isosurface 2 (b) isosurface 2.5 (c) isosurface 3 (d) Reference structure

Figure A.3: Model O results for SDF of C_{S1} around S_O in MSA at isosurface values of (a) 2, (b) 2.5 and (c) 3. Spatial orientation of the central MSA is displayed in (d).

A.2 SDF

Figures A.2, A.3 and A.4 show SDFs of C_{S1} around S_O with different isosurface values.

(a) isosurface 2 (b) isosurface 2.5 (c) isosurface 3 (d) Reference structure

Figure A.4: AIMD results for SDF of C_{S1} around S_O in MSA at isosurface values of (a) 6, (b) 8 and (c) 10. Spatial orientation of the central MSA is displayed in (d).

A.3 Force fields

Force field parameters of Model C and Model O are provided in separate files, model_-C.itp, model_C.rtp, model_C_psa.itp, model_C_psa.rtp, model_O.itp, and model_-O.rtp, in GROMACS format. Please refer to the supplemental information at https://pubs.acs.org/doi/10.1021/acs.jpcb.8b07736.

Heterogeneous Dynamics of Ionic Liquids: The Effects of Chain Length on Imidazolium-based Ionic Liquids

B.1 Fitted parameter for four point correlation function

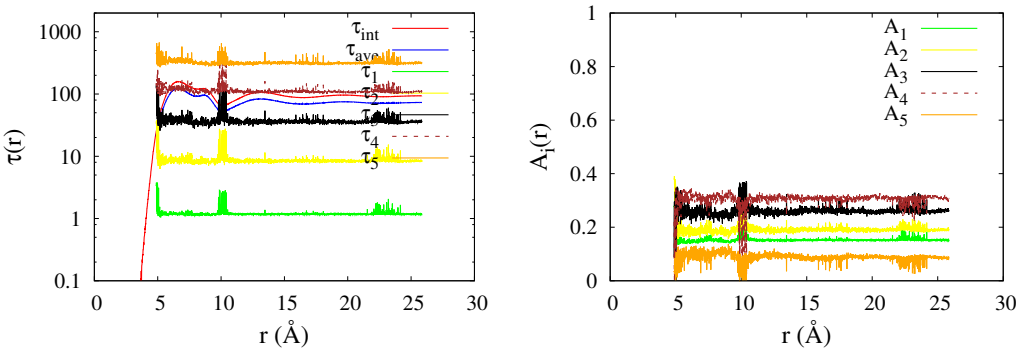

Figure B.1: Fitted parameters for EMI AC-AC

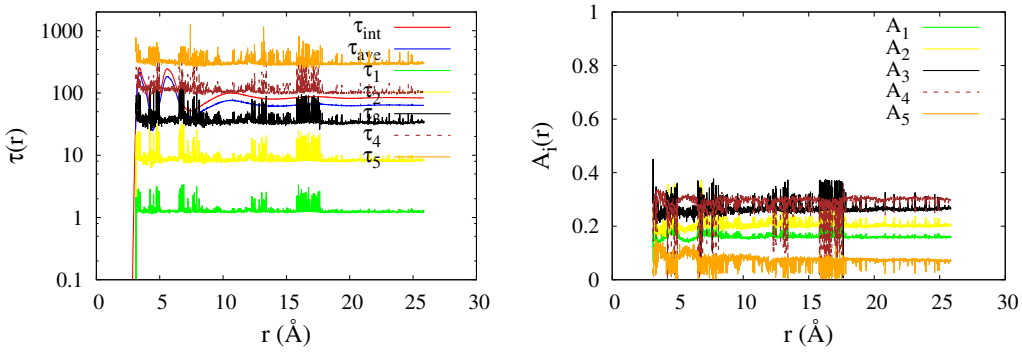

Figure B.2: Fitted parameters for EMI AC-C2

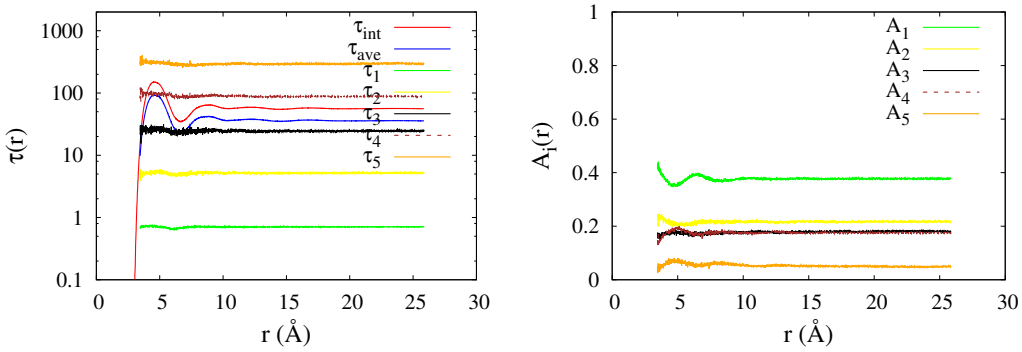

Figure B.3: Fitted parameters for EMI AC-CT

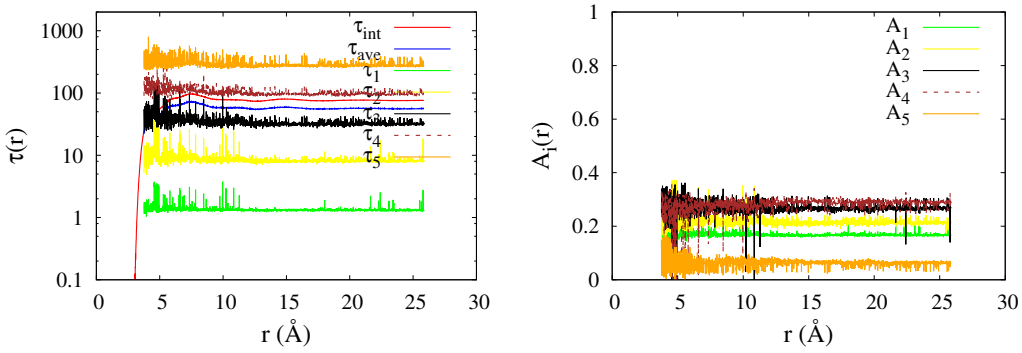

Figure B.4: Fitted parameters for EMI C2-C2

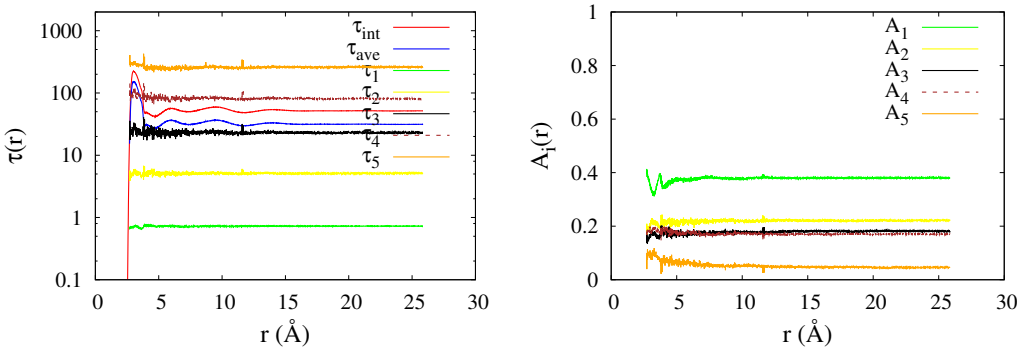

Figure B.5: Fitted parameters for EMI CT-C2

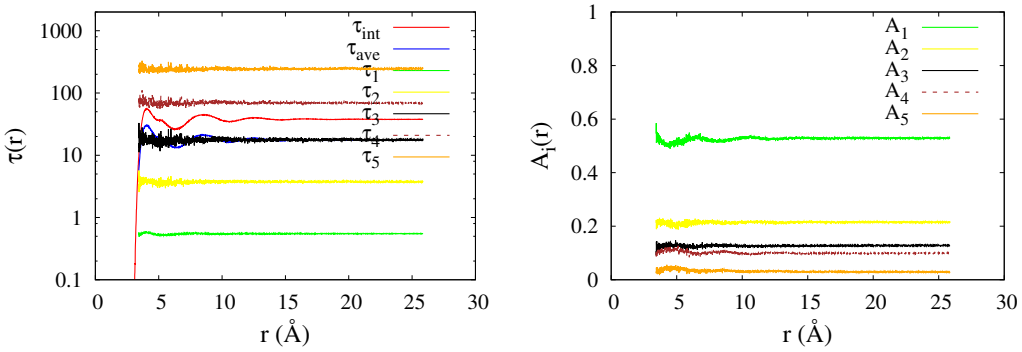

Figure B.6: Fitted parameters for EMI CT-CT

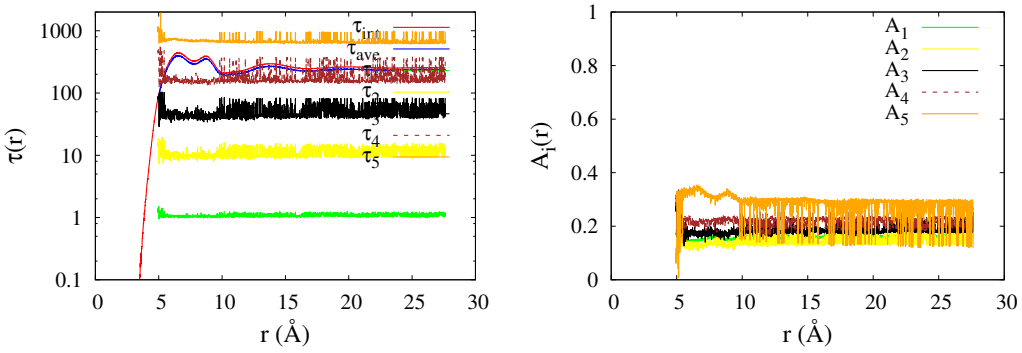

Figure B.7: Fitted parameters for BMI AC-AC

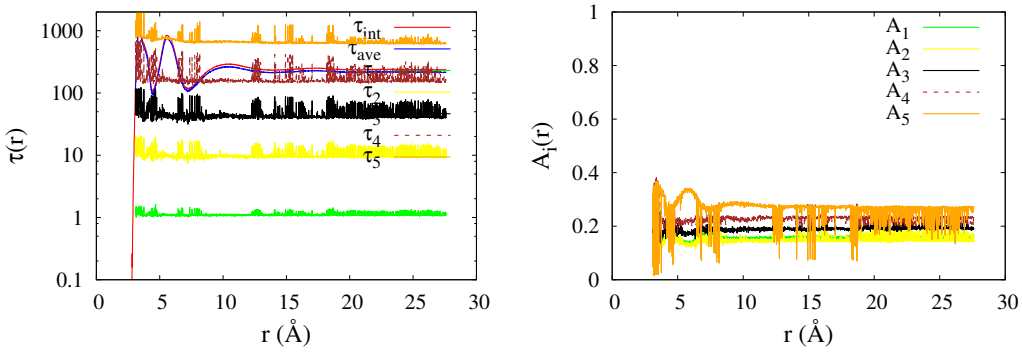

Figure B.8: Fitted parameters for BMI AC-C2

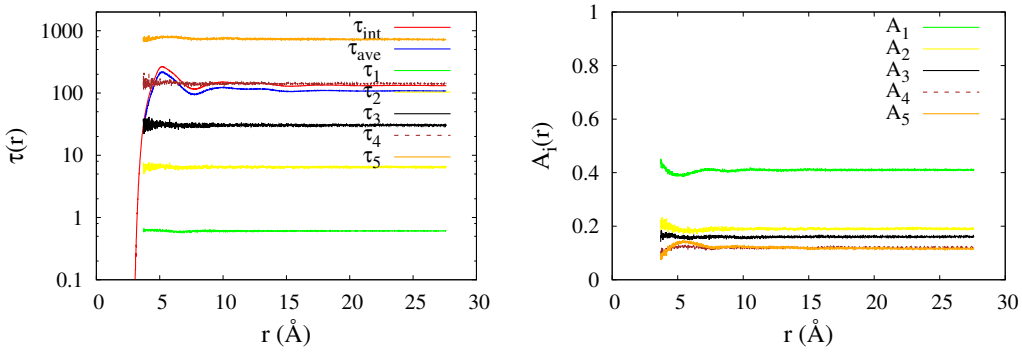

Figure B.9: Fitted parameters for BMI AC-CT

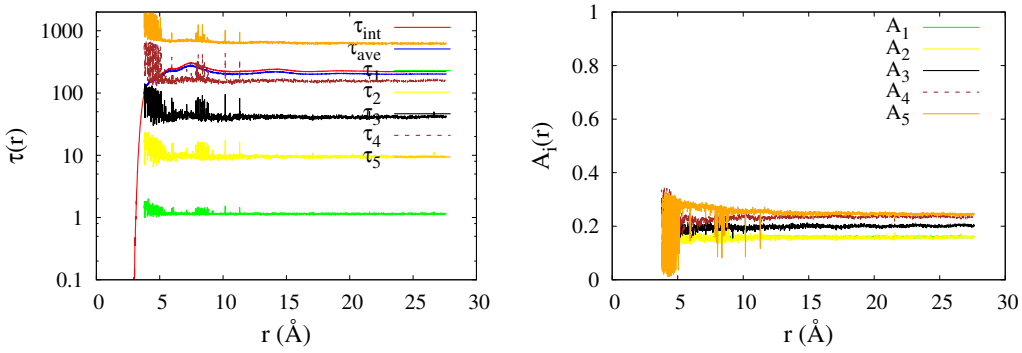

Figure B.10: Fitted parameters for BMI C2-C2

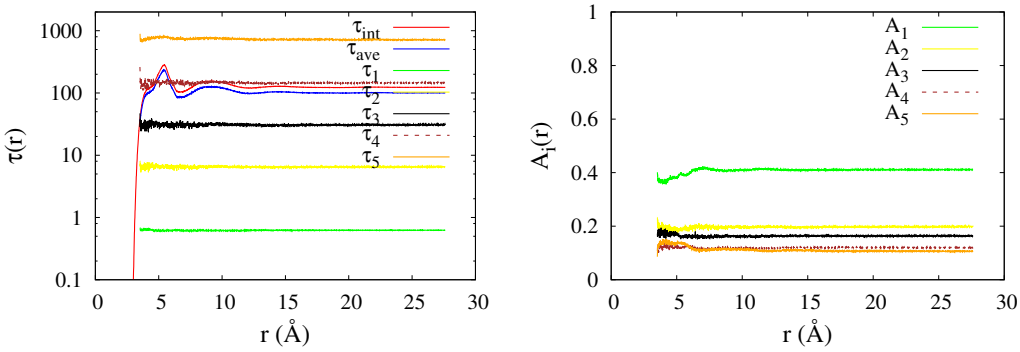

Figure B.11: Fitted parameters for BMI CT-C2

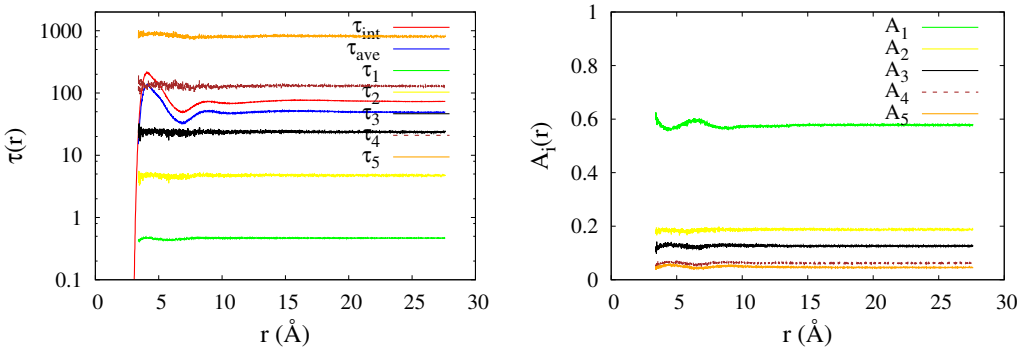

Figure B.12: Fitted parameters for BMI CT-CT

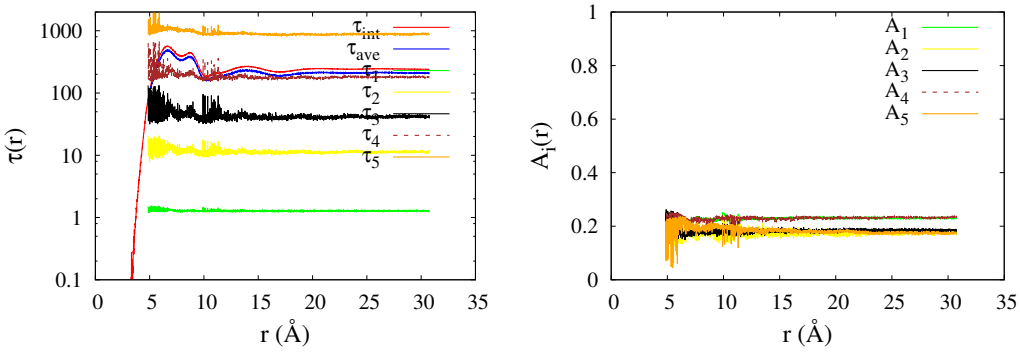

Figure B.13: Fitted parameters for OMI AC-AC

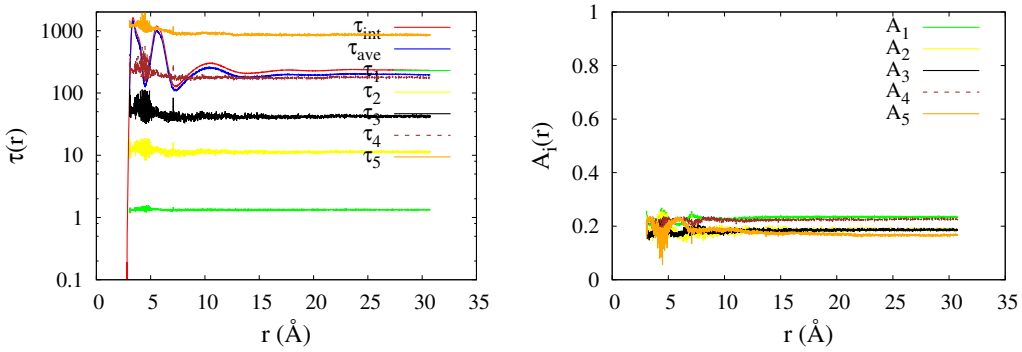

Figure B.14: Fitted parameters for OMI AC-C2

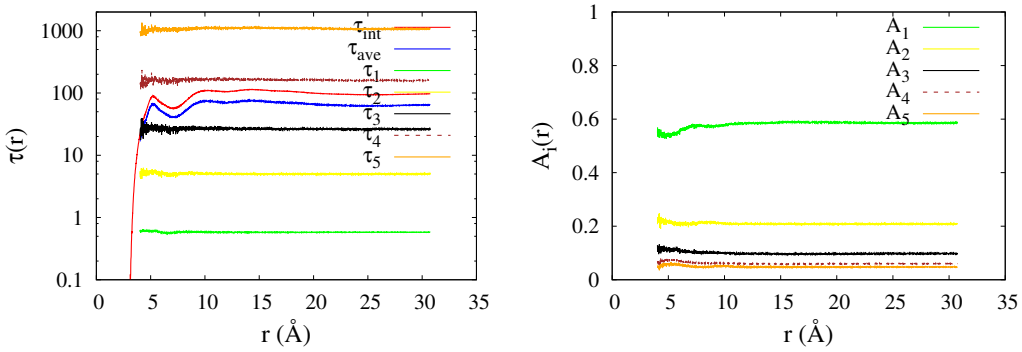

Figure B.15: Fitted parameters for OMI AC-CT

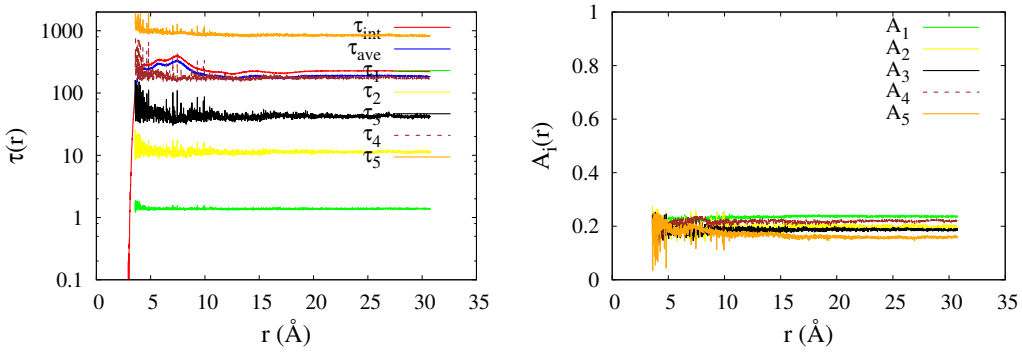

Figure B.16: Fitted parameters for OMI C2-C2

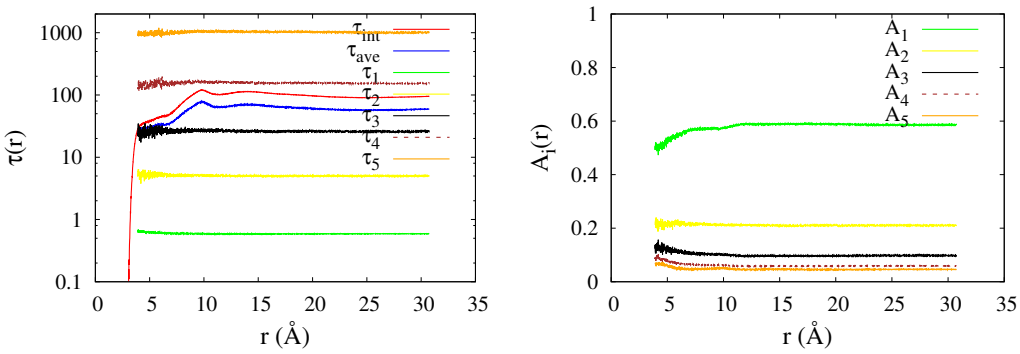

Figure B.17: Fitted parameters for OMI CT-C2

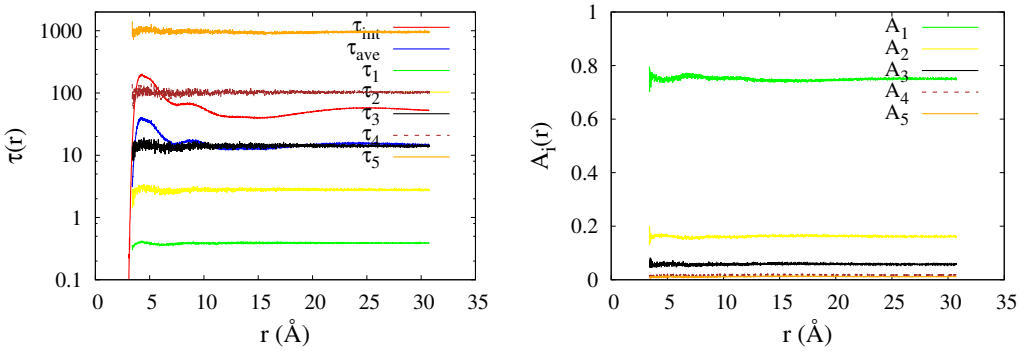

Figure B.18: Fitted parameters for OMI CT-CT

B.2 Fitted parameter for "mobile" self four point correlation function

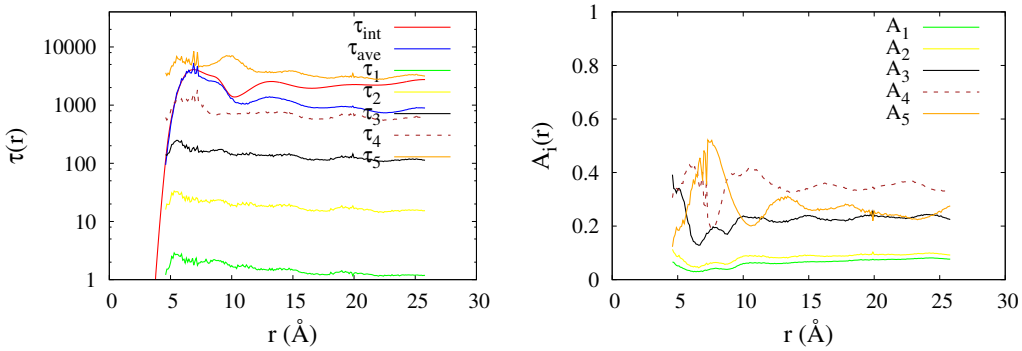

Figure B.19: Fitted parameters of "mobile" self four point correlation function for EMI AC-AC

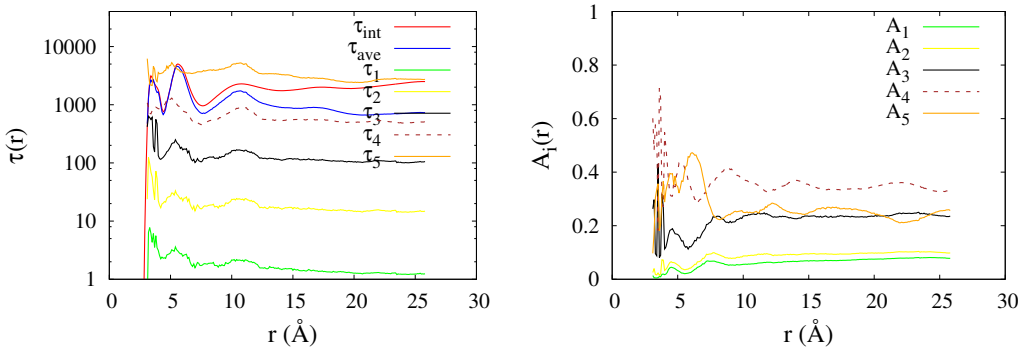

Figure B.20: Fitted parameters of "mobile" self four point correlation function for EMI AC-C2

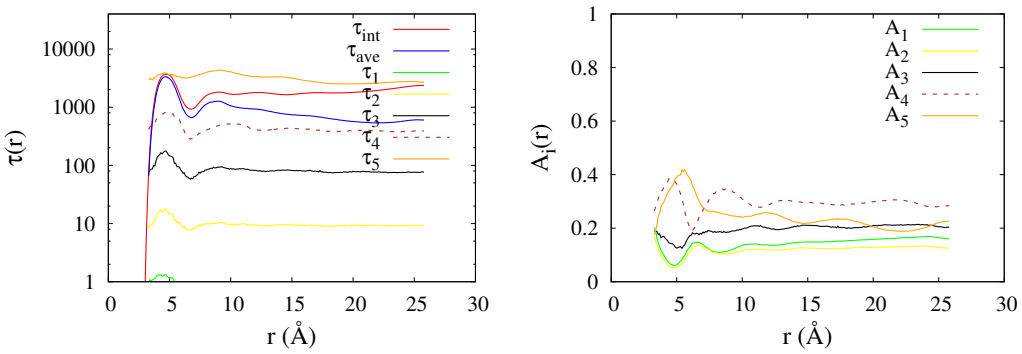

Figure B.21: Fitted parameters of "mobile" self four point correlation function for EMI AC-CT

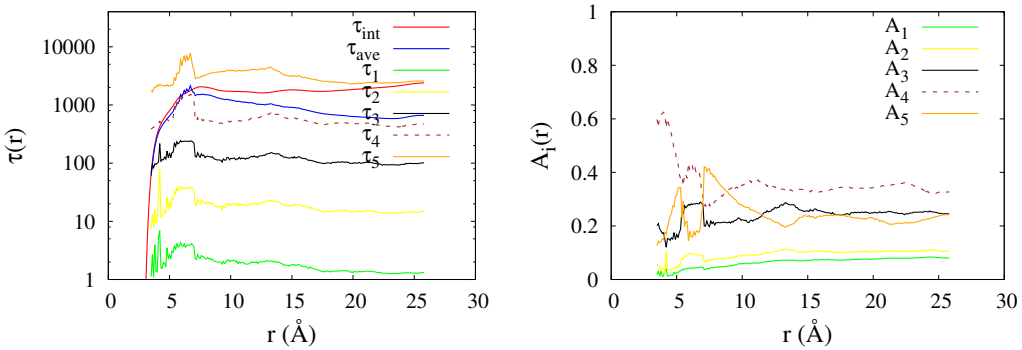

Figure B.22: Fitted parameters of "mobile" self four point correlation function for EMI C2-C2

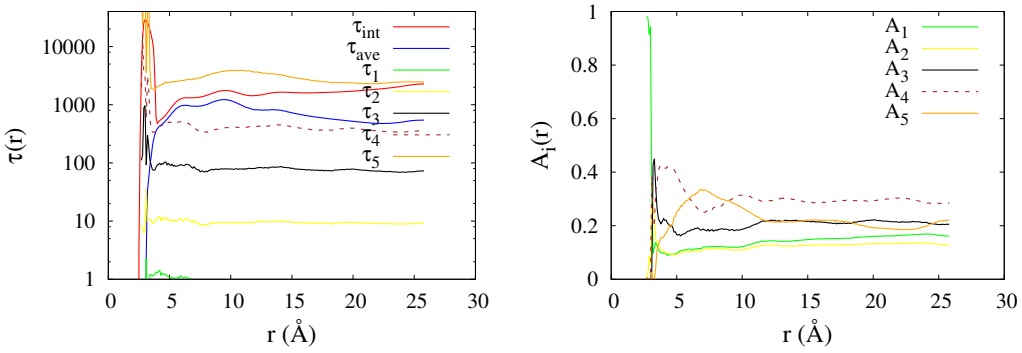

Figure B.23: Fitted parameters of "mobile" self four point correlation function for EMI C2-CT

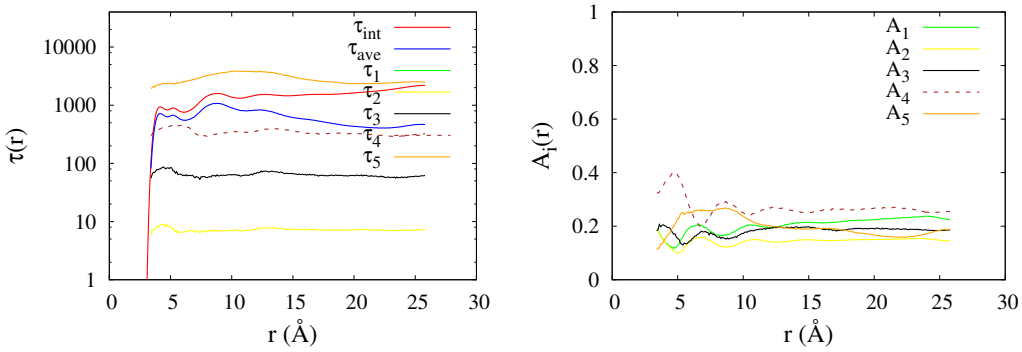

Figure B.24: Fitted parameters of "mobile" self four point correlation function for EMI CT-CT

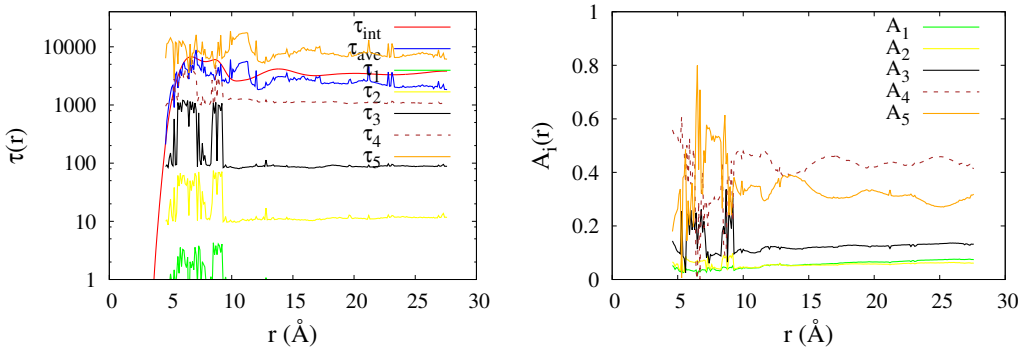

Figure B.25: Fitted parameters of "mobile" self four point correlation function for BMI AC-AC

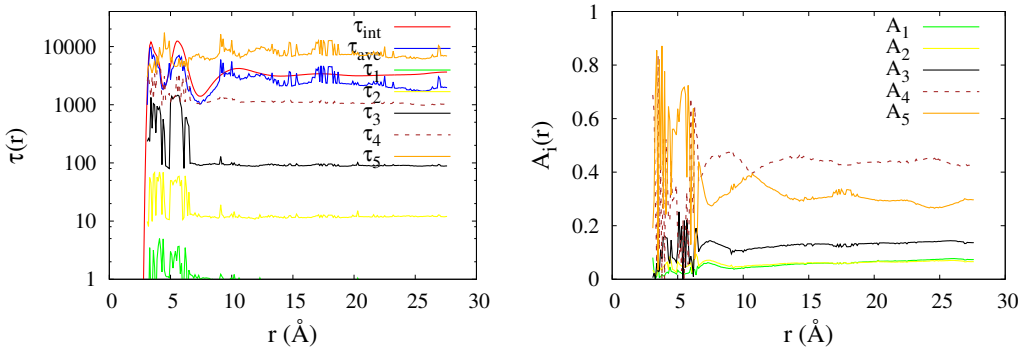

Figure B.26: Fitted parameters of "mobile" self four point correlation function for BMI AC-C2

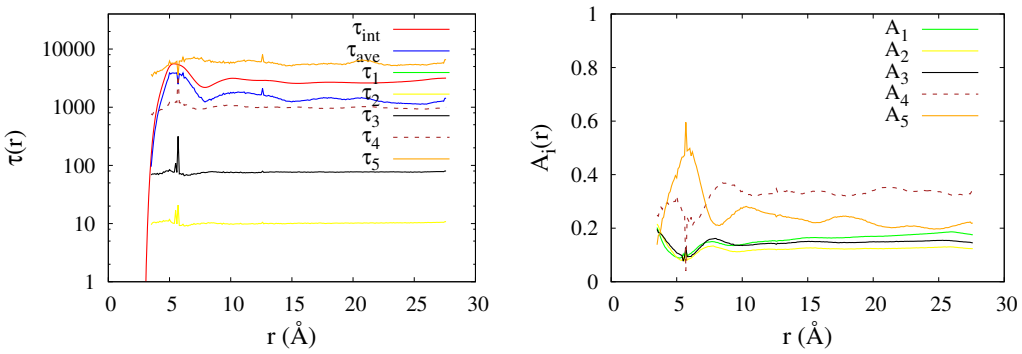

Figure B.27: Fitted parameters of "mobile" self four point correlation function for BMI AC-CT

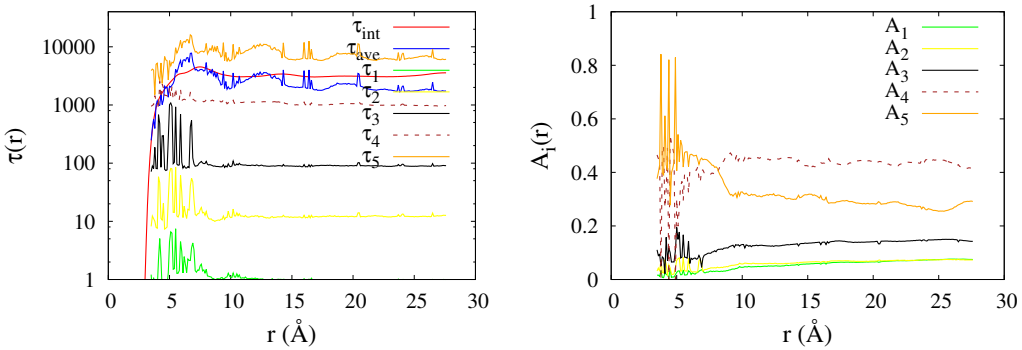

Figure B.28: Fitted parameters of "mobile" self four point correlation function for BMI C2-C2

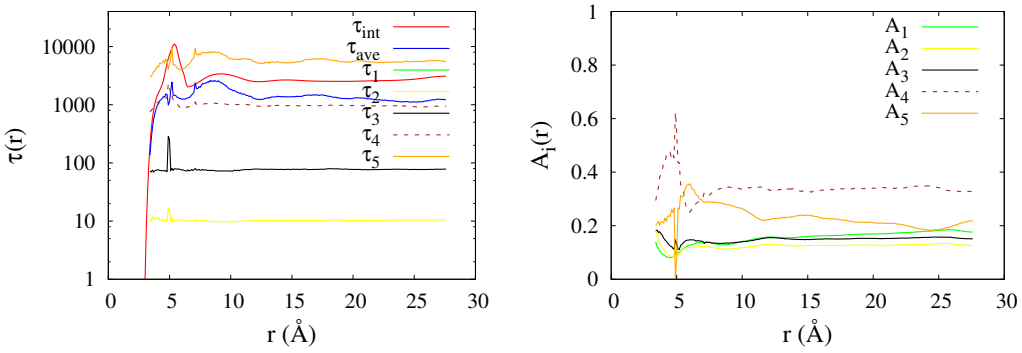

Figure B.29: Fitted parameters of "mobile" self four point correlation function for BMI C2-CT

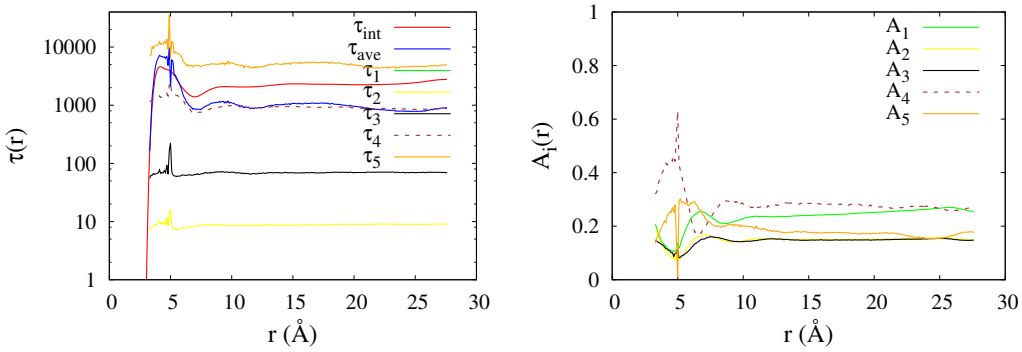

Figure B.30: Fitted parameters of "mobile" self four point correlation function for BMI CT-CT

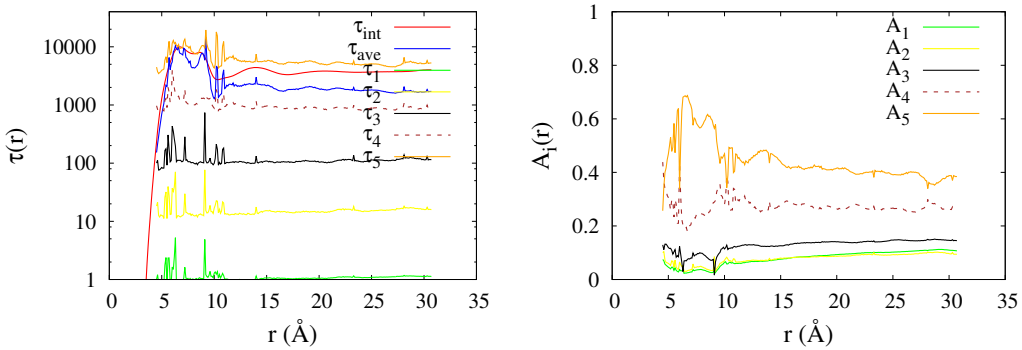

Figure B.31: Fitted parameters of "mobile" self four point correlation function for OMI AC-AC

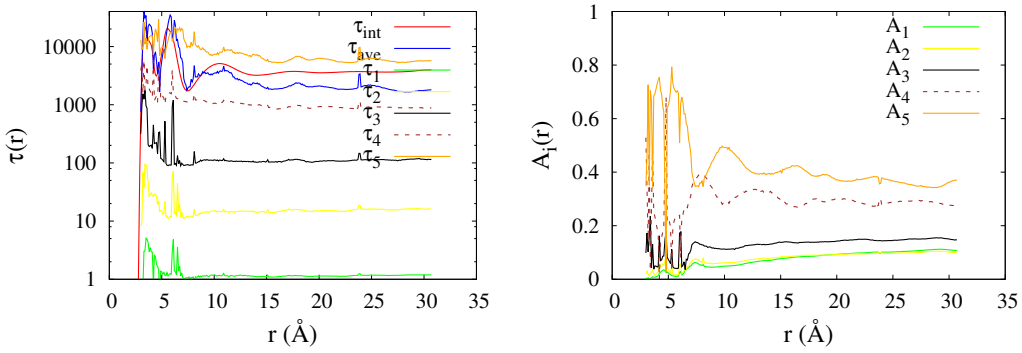

Figure B.32: Fitted parameters of "mobile" self four point correlation function for OMI AC-C2

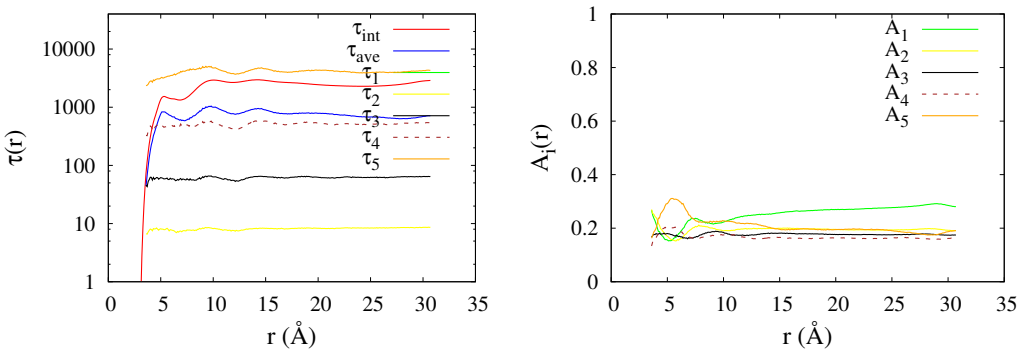

Figure B.33: Fitted parameters of "mobile" self four point correlation function for OMI AC-CT

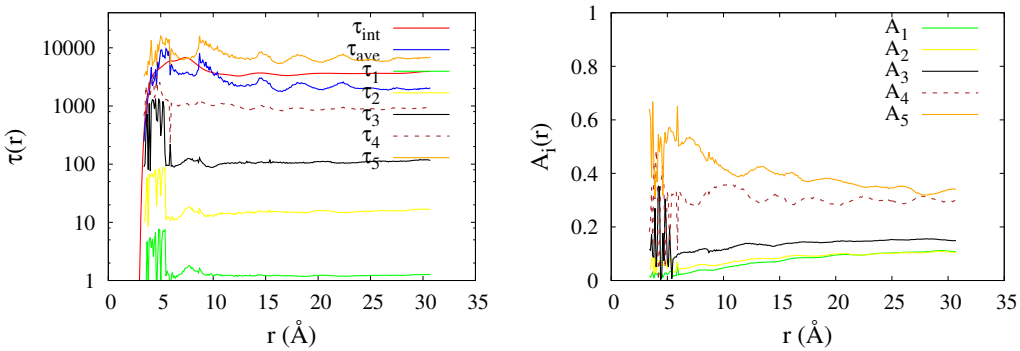

Figure B.34: Fitted parameters of "mobile" self four point correlation function for OMI C2-C2

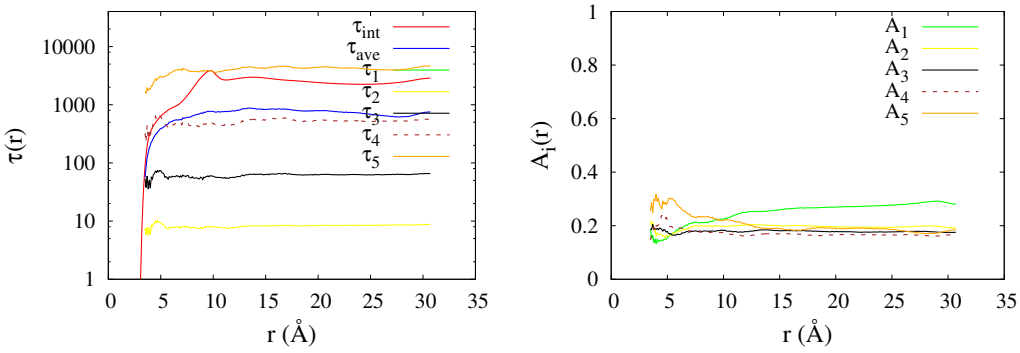

Figure B.35: Fitted parameters of "mobile" self four point correlation function for OMI C2-CT

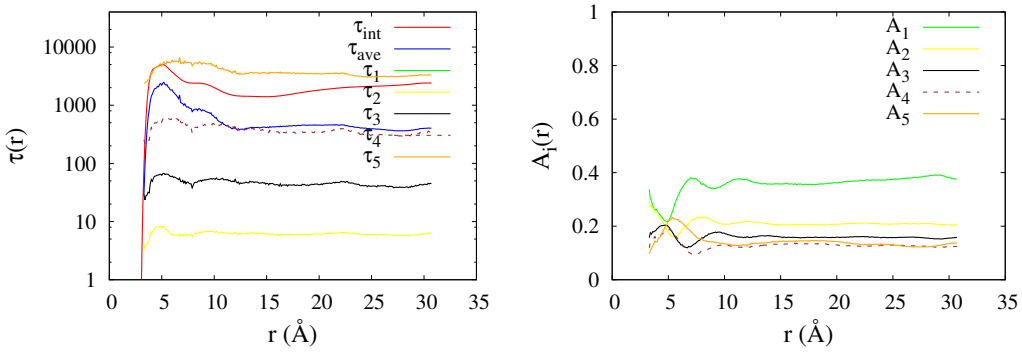

Figure B.36: Fitted parameters of “mobile” self four point correlation function for OMI CT-CT

Vibrational Spectroscopy of Imidazolium-based Ionic Liquids: A Combined MD/DFT Study

C.1 Force field parameters

C.1.1 CHARMM model description

Interactions in the CHARMM force field are described by

$$E = \sum_{i<j,bonds} \frac{1}{2} k_{ij}^{b} \left(r_{ij} - b_{ij}\right)^2 + \sum_{i<k,angles} \frac{1}{2} k_{ijk}^{\theta} \left(\theta_{ijk} - \theta_{ijk}^{0}\right)^2 + \frac{1}{2} k_{ijk}^{UB} \left(r_{ik} - r_{ik}^{0}\right)^2 + \sum_{i<l,dihedrals} \sum_{n} k_{n,ijkl}^{\phi} \left(1 + \cos\left(n\phi - \phi_{n,ijkl}\right)\right) + \sum_{improper} \frac{1}{2} k_{ijkl}^{\xi} \left(\xi_{ijkl} - \xi_{ijkl}^{0}\right) + \sum_{i<j} \left(\frac{q_i q_j}{4\pi\varepsilon_0 r_{ij}} + 4\epsilon_{ij} \left(\left(\frac{\sigma_{ij}}{r_{ij}}\right)^{12} - \left(\frac{\sigma_{ij}}{r_{ij}}\right)^{6} \right) \right) \quad \text{(C.1)}$$

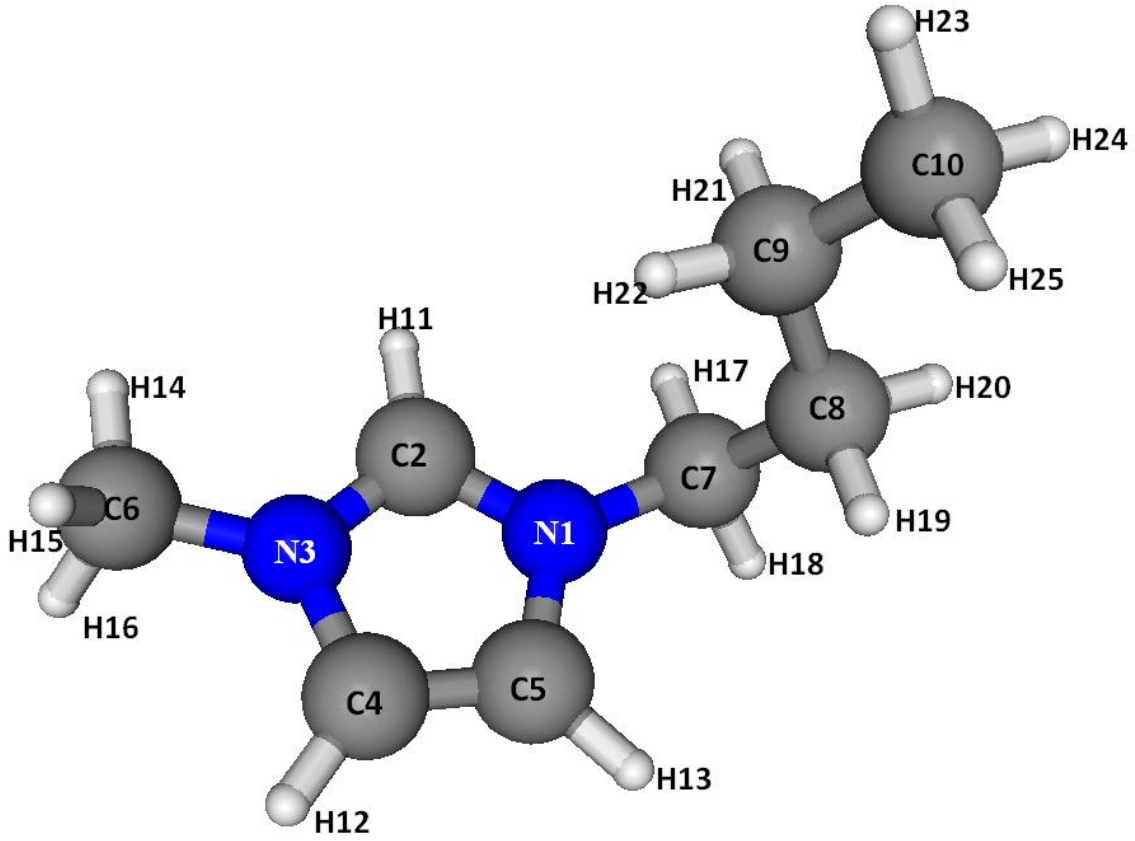

Figure C.1: Atom labels of buthylmetylimidazolium

Combination rules for LJ parameters listed in Table C.2 are

$$\sigma_{ij} = \frac{1}{2}(\sigma_i + \sigma_j) \tag{C.2}$$

$$\epsilon_{ij} = \sqrt{\epsilon_i \epsilon_j} \tag{C.3}$$

Note that for 1-4 interactions, special LJ parameters are needed for selected atoms in Table C.3

Table C.1: Charges in CHARMM

Label	Atom	$q(e)$
N1	NG2R52	-0.455
C2	CG2R53	0.333
N3	NG2R52	-0.503
C4	CG2R51	0.199
C5	CG2R51	0.199
C6	CG334	0.165
C7	CG324	0.200
C8	CG321	-0.160
H11	HGR53	0.153
H12	HGR52	0.126
H13	HGR52	0.126
H14	HGA3	0.090
H15	HGA3	0.090
H16	HGA3	0.090
C9	CG321	-0.178
C10	CG331	-0.285
H17	HGA2	0.090
H18	HGA2	0.090
H19	HGA2	0.090
H20	HGA2	0.090
H21	HGA2	0.090
H22	HGA2	0.090
H23	HGA3	0.090
H24	HGA3	0.090
H25	HGA3	0.090
Cl	CLA	-1.000
Br	BRA	-1.000
B	B	0.96
F	F	-0.49

Table C.2: LJ parameters in CHARMM

Atom	σ_{ij} (nm)	ϵ_{ij} (kJ/mol)
CG2R51	0.3741	0.2092
CG2R53	0.3919	0.0836
CG321	0.3581	0.2343
CG324	0.3875	0.2301
CG331	0.3652	0.3263
CG334	0.3946	0.3221
NG2R52	0.3296	0.8368
HGR52	0.1603	0.1924
HGR53	0.1247	0.1924
HGA2	0.2387	0.1464
HGA3	0.2387	0.1004
CLA	0.3650	0.8300
BRA	0.3970	0.8600
B	0.3581	0.3974
F	0.3118	0.2552

Table C.3: LJ parameters for special 1-4 interactions in CHARMM

Atom	σ_{ij} (nm)	ϵ_{ij} (kJ/mol)
CG321, CG324, CG331, CG334	0.33854151289	0.04184

Table C.4: Bond parameters in CHARMM

Atom_i	Atom_j	b_{ij} (nm)	k^b_{ij} (kJ/(mol $\cdot$nm^2))
CG2R51	CG2R51	0.1360	343088
CG2R51	NG2R52	0.1370	317984
CG2R51	HGR52	0.1083	313800
CG2R53	NG2R52	0.1320	317984
CG2R53	HGR53	0.1070	278654.4
CG321	CG321	0.1530	186188
CG321	CG324	0.1530	186188
CG321	CG331	0.1528	186188
CG324	CG331	0.1528	186188
CG321	HGA2	0.1111	258571.2
CG324	NG2R52	0.1453	251040
CG324	HGA2	0.1100	238069.6
CG331	HGA3	0.1111	269449.6
CG334	NG2R52	0.1453	251040
CG334	HGA3	0.1111	269449.6
B	F	0.1393	242672

Table C.5: Angle parameters in CHARMM

$Atom_i$	$Atom_j$	$Atom_k$	θ_{ijk} (degree)	k^{θ}_{ijk} (kJ/(mol·rad^2))	r^0_{ik} (nm)	k^{UB}_{ijk} (kJ/(mol·nm^2))
CG2R51	CG2R51	NG2R52	108.0	1213.3600	0.0000	0.00
CG2R51	CG2R51	HGR52	130.0	184.0960	0.2215	12552.00
NG2R52	CG2R51	HGR52	122.0	184.0960	0.2180	12552.00
NG2R52	CG2R53	NG2R52	108.0	1213.3600	0.0000	0.00
NG2R52	CG2R53	HGR53	126.0	267.7760	0.2140	20920.00
CG321	CG321	CG324	110.5	488.2728	0.2561	9338.69
CG321	CG321	CG331	115.0	485.3440	0.2561	6694.40
CG321	CG321	HGA2	110.1	221.7520	0.2179	18853.10
CG324	CG321	HGA2	110.1	221.7520	0.2179	18853.10
CG331	CG321	HGA2	110.1	289.5328	0.2179	18853.10
CG331	CG324	HGA2	110.1	289.5328	0.2179	18853.10
HGA2	CG321	HGA2	109.0	297.0640	0.1802	4518.72
CG321	CG324	NG2R52	110.0	566.5136	0.0000	0.00
CG331	CG324	NG2R52	110.0	566.5136	0.0000	0.00
CG321	CG324	HGA2	111.8	221.7520	0.2179	18853.10
NG2R52	CG324	HGA2	110.1	351.4560	0.0000	0.00
HGA2	CG324	HGA2	109.0	297.0640	0.1802	4518.72
CG321	CG331	HGA3	110.1	289.5328	0.2179	18853.10
CG324	CG331	HGA3	110.1	289.5328	0.2179	18853.10
HGA3	CG331	HGA3	108.4	297.0640	0.1802	4518.72
NG2R52	CG334	HGA3	110.1	351.4560	0.0000	0.00
HGA3	CG334	HGA3	108.4	297.0640	0.1802	4518.72
CG2R51	NG2R52	CG2R53	108.0	1213.3600	0.0000	0.00

CG2R51	NG2R52	CG324	124.9	209.2000	0.2130	12552.00
CG2R51	NG2R52	CG334	124.9	209.2000	0.2130	12552.00
CG2R53	NG2R52	CG324	127.1	209.2000	0.2090	12552.00
CG2R53	NG2R52	CG334	127.1	209.2000	0.2090	12552.00
F	B	F	109.5	418.2	0.0	0.0

Table C.6: Dihedral angle parameters in CHARMM

Atom_i	Atom_j	Atom_k	Atom_l	$\phi_{n,ijkl}$ (degree)	$k^{\phi}_{n,ijkl}$ (kJ/mol)	n
NG2R52	CG2R51	CG2R51	NG2R52	180	50.20800	2
NG2R52	CG2R51	CG2R51	HGR52	180	10.46000	2
HGR52	CG2R51	CG2R51	HGR52	180	4.18400	2
CG2R51	CG2R51	NG2R52	CG2R53	180	50.20800	2
CG2R51	CG2R51	NG2R52	CG324	180	25.10400	2
CG2R51	CG2R51	NG2R52	CG334	180	25.10400	2
HGR52	CG2R51	NG2R52	CG2R53	180	10.46000	2
HGR52	CG2R51	NG2R52	CG324	180	37.65600	2
HGR52	CG2R51	NG2R52	CG334	180	37.65600	2
NG2R52	CG2R53	NG2R52	CG2R51	180	50.20800	2
NG2R52	CG2R53	NG2R52	CG324	180	32.21680	2
NG2R52	CG2R53	NG2R52	CG334	180	32.21680	2
HGR53	CG2R53	NG2R52	CG2R51	180	12.55200	2
HGR53	CG2R53	NG2R52	CG324	180	26.35920	2
HGR53	CG2R53	NG2R52	CG334	180	26.35920	2
CG324	CG321	CG321	CG331	0	0.81588	3
CG324	CG321	CG321	HGA2	0	0.81588	3
CG331	CG321	CG321	HGA2	0	0.75312	3

HGA2	CG321	CG321	HGA2	0	0.92048	3
CG321	CG321	CG324	NG2R52	0	0.81588	3
CG321	CG321	CG324	HGA2	0	0.81588	3
HGA2	CG321	CG324	NG2R52	0	0.81588	3
HGA2	CG321	CG324	HGA2	0	0.81588	3
NG2R52	CG324	CG331	HGA3	0	0.81588	3
CG321	CG321	CG331	HGA3	0	0.66944	3
HGA2	CG321	CG331	HGA3	0	0.66944	3
HGA2	CG324	CG331	HGA3	0	0.66944	3
CG321	CG324	NG2R52	CG2R51	180	0.00000	6
CG321	CG324	NG2R52	CG2R53	180	0.00000	6
CG331	CG324	NG2R52	CG2R51	180	0.00000	6
CG331	CG324	NG2R52	CG2R53	180	0.00000	6
HGA2	CG324	NG2R52	CG2R51	180	0.62760	3
HGA2	CG324	NG2R52	CG2R53	180	0.62760	3
HGA3	CG334	NG2R52	CG2R51	180	0.62760	3
HGA3	CG334	NG2R52	CG2R53	180	0.62760	3

Table C.7: Improper dihedral angle parameters in CHARMM

Atom_i	Atom_j	Atom_k	Atom_l	ξ^0_{ijkl} (degree)	k^ξ_{ijkl} (kJ/(mol·rad^2))
NG2R52	X	X	X	0.0	10.0416

* X represents arbitrary atom.

** Atom_i is the center atom.

C.1.2 OPLS-AA model description

Interactions in the OPLS-AA force field are described by

$$E = \sum_{i<j,bonds} \frac{1}{2} k_{ij}^{b} \left(r_{ij} - b_{ij}\right)^2 + \sum_{i<k,angles} \frac{1}{2} k_{ijk}^{\theta} \left(\theta_{ijk} - \theta_{ijk}^{0}\right)^2 + \sum_{i<l,dihedrals} \sum_{n=1}^{4} \frac{1}{2} V_{n,ijkl} \left(1 - (-1)^n \cos\left(n\phi_{ijkl}\right)\right) + \sum_{i<l,improper} \sum_{n} k_{n,ijkl}^{\phi} \left(1 + \cos\left(n\phi - \phi_{n,ijkl}\right)\right) + \sum_{i<j} \left(\frac{q_i q_j}{4\pi\varepsilon_0 r_{ij}} + 4\epsilon_{ij} \left(\left(\frac{\sigma_{ij}}{r_{ij}}\right)^{12} - \left(\frac{\sigma_{ij}}{r_{ij}}\right)^{6} \right) \right) \quad \text{(C.4)}$$

Combination rules for LJ parameters listed in Table C.9 are

$$\sigma_{ij} = \sqrt{\sigma_i \sigma_j} \quad \text{(C.5)}$$

$$\epsilon_{ij} = \sqrt{\epsilon_i \epsilon_j} \quad \text{(C.6)}$$

Note that all 1-4 non-bonded interactions including electrostatic and LJ interactions in OPLS-AA force field are scale by 0.5.

Table C.8: Charges in OPLS-AA

Label	Atom	$q(e)$
N1	NA	0.15
C2	CR	-0.11
N3	NA	0.15
C4	CW	-0.13
C5	CW	-0.13
C6	CT	-0.17
C7	CT	-0.17
C8	CT	0.01
H11	HA	0.21
H12	HA	0.21
H13	HA	0.21
H14	HC	0.13
H15	HC	0.13
H16	HC	0.13
C9	CT	-0.12
C10	CT	-0.18
H17	HC	0.13
H18	HC	0.13
H19	HC	0.06
H20	HC	0.06
H21	HC	0.06
H22	HC	0.06
H23	HC	0.06
H24	HC	0.06
H25	HC	0.06
Cl	CLA	-1.00
Br	BRA	-1.00
B	B	0.96
F	F	-0.49

Table C.9: LJ parameters in OPLS-AA

Atom	σ_{ij} (nm)	ϵ_{ij} (kJ/mol)
CT	0.350	0.27614
CR	0.355	0.29288
CW	0.355	0.29288
HC	0.250	0.12552
HA	0.242	0.12552
NA	0.325	0.71128
CLA	0.365	0.83000
BRA	0.397	0.86000
B	0.358	0.39748
F	0.311	0.25522

Table C.10: Bond parameters in OPLS-AA

Atom_i	Atom_j	b_{ij} (nm)	k^b_{ij} (kJ/(mol $\cdot$nm^2))
HC	CT	0.1090	284500
CT	CT	0.1529	224200
CR	HA	0.1080	284500
CW	HA	0.1080	284500
CR	NA	0.1315	399200
CW	NA	0.1378	357400
CW	CW	0.1341	435200
NA	CT	0.1466	282000
B	F	0.1393	242672

Table C.11: Angle parameters in OPLS-AA

Atom_i	Atom_j	Atom_k	θ_{ijk} (degree)	k^{θ}_{ijk} (kJ/(mol·rad^2))
CT	CT	CT	112.7	488.3
CT	CT	HC	110.7	313.8
HC	CT	HC	107.8	276.1
CW	NA	CR	108.0	585.8
CW	NA	CT	125.6	585.8
CR	NA	CT	126.4	585.8
NA	CR	HA	125.1	292.9
NA	CR	NA	109.8	585.8
NA	CW	CW	107.1	585.8
NA	CW	HA	122.0	292.9
CW	CW	HA	130.9	292.9
NA	CT	HC	110.7	313.8
NA	CT	CT	112.7	488.3
F	B	F	109.5	418.2

Table C.12: Dihedral angle parameters in OPLS-AA

Atom_i	Atom_j	Atom_k	Atom_l	$V_{1,ijkl}$ (kJ/mol)	$V_{2,ijkl}$ (kJ/mol)	$V_{3,ijkl}$ (kJ/mol)	$V_{4,ijkl}$ (kJ/mol)
HC	CT	CT	HC	0.0000	0.0000	1.3305	0.0000
CT	CT	CT	HC	0.0000	0.0000	1.5313	0.0000
CT	CT	CT	CT	7.2800	-0.6569	1.1673	0.0000
CW	NA	CR	NA	0.0000	19.4600	0.0000	0.0000
CW	NA	CR	HA	0.0000	19.4600	0.0000	0.0000
CT	NA	CR	NA	0.0000	19.4600	0.0000	0.0000

CT	NA	CR	HA	0.0000	19.4600	0.0000	0.0000
CR	NA	CW	CW	0.0000	12.5520	0.0000	0.0000
CR	NA	CW	HA	0.0000	12.5520	0.0000	0.0000
CT	NA	CW	CW	0.0000	12.5520	0.0000	0.0000
CT	NA	CW	HA	0.0000	12.5520	0.0000	0.0000
NA	CW	CW	NA	0.0000	44.9800	0.0000	0.0000
NA	CW	CW	HA	0.0000	44.9800	0.0000	0.0000
HA	CW	CW	HA	0.0000	44.9800	0.0000	0.0000
CW	NA	CT	HC	0.0000	0.0000	0.5190	0.0000
CR	NA	CT	HC	0.0000	0.0000	0.0000	0.0000
CW	NA	CT	CT	-7.1535	6.1064	0.7939	0.0000
CR	NA	CT	CT	-5.2691	0.0000	0.0000	0.0000
NA	CT	CT	CT	-7.4797	3.1642	-1.2026	0.0000
NA	CT	CT	HC	0.0000	0.0000	0.3670	0.0000

Table C.13: Improper dihedral angle parameters in OPLS-AA

Atom_i	Atom_j	Atom_k	Atom_l	$\phi_{n,ijkl}$ (degree)	$k^{\phi}_{n,ijkl}$ (kJ/mol)	n
CR	CW	NA	CT	180.0	4.18400	2
NA	NA	CR	HA	180.0	4.60240	2
NA	CW	CW	HA	180.0	4.60240	2